

Modelling and Simulations of Corona Discharge Currents in a Large Scale Coaxial Geometry with a Dielectric Barrier due to Low Frequency Triangular Voltages

by

Martin Macken

Diploma work no. 135/2014

Department of Materials and Manufacturing Technology

Division of High Voltage Engineering

CHALMERS UNIVERSITY OF TECHNOLOGY

Gothenburg, Sweden

Diploma work in the Master's Program of Electric Power Engineering

Performed at Chalmers University of Technology

SE-412 46 Gothenburg, Sweden

Supervisor/Examiner:

Associate Professor Yuriy Serdyuk

Department of Materials and Manufacturing Technology

Division of High Voltage Engineering

Chalmers University of Technology

SE-412 46 Gothenburg, Sweden

Modelling and Simulations of Corona Discharge Currents in a Large Scale Coaxial Geometry with a Dielectric Barrier due to Low Frequency Triangular Voltages

MARTIN MACKEN

© MARTIN MACKEN, 2014

Diploma work no. 135/2014

Department of Materials and Manufacturing Technology

Division of High Voltage Engineering

Chalmers University of Technology

SE-412 96 Gothenburg, Sweden

Telephone: +46 (0)31 772 1000

Reproservice

Göteborg, Sweden 2014

ABSTRACT

When a high voltage is applied to electrodes immersed in air and provides a strongly non-uniform electric field, charged species such as free electrons and positive and negative ions can be created in gas due to corona discharge. Charged species will drift in the field from one electrode to another and eventually will be collected on dielectric surfaces if solid insulating elements are present in the discharge volume. The accumulated surface charges may strongly alter the electric field distribution in the entire system intensifying insulation ageing and increasing risk for flashovers. Such charge accumulation is an inherent phenomenon for DC applications and is also essential in cases of varying voltages when the dimension of the air gap is smaller than the travelling distances of the charged species. Recently, experiments have been carried out at ABB Corporate Research in Västerås (Sweden), where a large scale coaxial electrode arrangement was used to measure the level of the corona discharge current when triangular voltages of different frequencies were applied. The experiments were carried out both for free air and when a dielectric barrier was introduced in the discharge gap.

In the thesis, the experimental results obtained for the case of coronas with dielectric barrier are analyzed by means of computer simulations. A model was developed that couples partial differential equations describing drift and diffusion of charged species with Poisson's equation for computing space charge controlled electric field. The model accounts for field dependent generation and loss of free charges in gas and their accumulation on solid surfaces. The model was implemented in COMSOL Multiphysics. Simulations were conducted for conditions as close as possible to those used in the experiments including electrode system geometry, environmental parameters (temperature, pressure) and shapes of the applied voltages. Special attention was paid to correct representations of boundary conditions that was found to be a key for reproducing experimental results for voltages of low frequencies when the travelling length of ions was large. The results obtained from the performed simulations are in agreement with the experimental corona characteristics acquired by ABB. The performed computational study allows for analyzing experimental data and provides insight on physical mechanisms leading to experimentally observed phenomena.

Keywords: corona discharge, discharge modeling, corona current-voltage characteristics, barrier charge accumulation, triangular voltage, corona discharge simulation.

ACKNOWLEDGMENTS

I the author, would like to express my sincere and deepest appreciation to my supervisor and examiner, Associate Professor Yuriy Serdyuk, who has been a great help and inspiration when writing this thesis. Yuriy has patiently been explaining the phenomena of corona discharges and providing insightful and thorough answers and discussions to all the befuddled and not always very clear questions and ideas I have come up with throughout this work. For this I am truly thankful.

I would also like to say thank you to Olof Hjortstam and Birgitta Källstrand at ABB Corporate Research for providing me with results and research data from their experiments, as well as answers to my questions posted to them.

Here, I would also want to direct a thank you to Shailendra Singh at Chalmers for the fruitful discussions and input on the subject of the thesis. Shailendra is a man of great knowledge and I wish him all the best.

Finally, I would like to say thank you to my parents and my wife for their everlasting support to me through life.

TABLE OF CONTENTS

CHAPTER 1 INTRODUCTION	1
1.1. BACKGROUND	1
1.2. AIM	2
1.3. LAYOUT	2
CHAPTER 2 CORONA THEORY.....	5
2.1. GAS LAWS	6
2.2. BACKGROUND IONIZATION	6
2.3. IONIZATION, DETACHMENT, ATTACHMENT AND RECOMBINATION.....	8
2.4. IONIC DRIFT, MOBILITY AND DRIFT FLUX	11
2.5. DIFFUSION AND DIFFUSION FLUX	12
2.6. HYDRODYNAMICS AND SOURCE TERMS.....	13
2.7. TOWNSEND'S FIRST IONIZATION COEFFICIENT.....	14
2.8. ATTACHMENT COEFFICIENT	15
2.9. DETACHMENT COEFFICIENT	15
2.10. RECOMBINATION COEFFICIENTS.....	16
2.11. TOWNSEND'S SECOND IONIZATION COEFFICIENT.....	16
2.12. ELECTRIC FIELD	16
2.13. SURFACE CHARGE.....	17
2.14. SPACE CHARGE	17
2.15. DISCHARGE DEVELOPMENT	19
2.16. DISCHARGE CURRENTS.....	21

CHAPTER 3 EXPERIMENTAL MEASUREMENTS	23
3.1. EXPERIMENTAL SETUP.....	23
3.2. EXPERIMENTAL RESULTS	23
CHAPTER 4 MODEL IMPLEMENTATION.....	27
4.1. GEOMETRY AND MATERIALS.....	29
4.2. ELECTROSTATICS	29
4.3. TRANSPORT OF DILUTED SPECIES	30
4.4. BOUNDARY ODEs AND DAEs	32
4.5. REDUCED IONIZATION COEFFICIENT	32
4.6. REDUCED ATTACHMENT COEFFICIENT.....	32
4.7. REDUCED ELECTRON DRIFT VELOCITY.....	34
4.8. DIFFUSION COEFFICIENTS	34
4.9. APPLIED VOLTAGE SHAPE.....	35
4.10. CONSTANT PARAMETERS	36
4.11. VARIABLE PARAMETERS	38
4.12. BOUNDARY FLUXES AND CALCULATION OF SURFACE CHARGE.....	40
4.13. CURRENT CALCULATIONS.....	41
4.14. MESHING OF THE MODEL	43
4.15. STUDY SETTINGS.....	43
CHAPTER 5 SIMULATIONS AND RESULTS	47
5.1. SIMULATIONS WITHOUT PVC-BARRIER.....	48
5.2. CORONA CURRENT COMPONENTS	53
5.3. SPACE CHARGE ACCUMULATION IN GAS	55
5.4. EFFECT OF SPACE CHARGE ON ELECTRIC FIELD DISTRIBUTION	61
5.5. SIMULATIONS WITH PVC-BARRIER.....	62

5.6.	CORONA CURRENT COMPONENTS IN PRESENCE OF BARRIER	66
5.7.	CHARGE ACCUMULATION ON BARRIER SURFACES.....	68
5.8.	IMPACT OF SURFACE CHARGE ON THE BARRIER ON ELECTRIC FIELD DISTRIBUTION	73
CHAPTER 6 CONCLUSIONS		77
6.1.	EVALUATION OF THE MODEL	77
6.2.	FUTURE WORK.....	78
REFERENCES		81
APPENDIX 1		83
APPENDIX 2		87

CHAPTER

1

INTRODUCTION

Corona discharges have been a topic of studies for a long time, and while being nuisance for transmission companies, it has a wide arrange of industrial applications. Excessive studies of the phenomenon have rendered an extensive amount of empirical data concerning gaseous media. This thesis aims to shed some light upon the topic of modelling of corona currents. In the introduction chapter, a background to the problem as well as the aim of the thesis and the method of execution are described.

1.1. BACKGROUND

Comprehensive studies have been carried out on the impact of charge accumulation on dielectric surfaces and their effects on the electric field strength when a high DC-voltage is used. In contrast to that, not as many studies have been performed for alternating voltages of different shapes (triangular, squared, PWM) which appear in emerging applications due to the used op power electronic devices. This is of great importance when it comes to designing such components like bushings and bushing insulation. It is therefore necessary to study how charges accumulate on insulating materials, and to conclude how these charges affect the material not only in a long run but also in short-term with an increasing risk for flashovers.

ABB Corporate Research in Västerås has conducted experiments where the dynamic behavior of charge carriers produced by corona has been studied. The experiment was carried out in large scale coaxial geometry, utilizing a thin wire as a corona electrode surrounded by an external grounded cylinder (1 m in diameter, further details are provided in Chapter 3). The experiment was performed with two setups: one where both electrodes were immersed in free air and one where the wire was suspended inside a cylindrical insulator (PVC tube), separating the gas gap into two parts. A triangular voltage of different magnitudes and frequencies was applied between the wire and external cylinder and resulting corona currents were measured.

To evaluate the results of the experiment and to be able to draw conclusion on how different parameters influence the result, it is complicated to only use the experimental results. Therefore, a FEM-model is constructed, where variables easily can be altered and the resulting impact on the corona discharge current can be assessed (FEM, or Finite Element Method, is a numerical method to solve partial differential equations).

In a previous thesis, carried out by Georgii Karman in [1], a FEM-model has been developed to analyze the experiments for corona from the wire in free air under triangular voltages of higher frequencies. The present thesis can be viewed as a continuation of the work by G. Karman, but focus will instead be directed to modelling of lower frequencies with and without the cylindrical insulator.

1.2. AIM

The aim of the thesis is to develop the model further by refining boundary conditions and computational parameters to provide result for corona at alternating triangular voltages of low frequency (below 10 Hz). Since low frequency voltages provide a more intricate simulation environment, it is of utmost importance that correct boundary conditions are provided. Since the voltage utilized is changing polarity, it imposes further problems of how to deal with the change of the electric field. This is one of the problems this thesis aims to provide a solution for. When a PVC-barrier is included in the discharge volume, it is even more important that the boundary conditions at its surfaces function in a satisfying way, making sure that charged species are allowed to accumulate and move away with change of polarity, as they should.

Another problem when modelling this type of corona discharges is the great amount of computational power and time needed to resolve a solution. By refining the meshing in certain computational areas and allowing for a coarser mesh in other areas, the computational time can be reduced. However, it is still important to allow a mesh to be fine enough to get an accurate resolution to the solution.

1.3. LAYOUT

The master thesis project will be divided into five parts. The first part describes and discusses the theoretical physics involved and describes the processes of greater interest in a corona discharge. The second part describes an experimental setup of corona discharge geometry and the results obtained from this experiment. The third part describes how a mathematical simulation model is constructed and implemented into the FEM-modeling software. In the fourth part results obtained

from the simulations will be presented and discussed. Finally, in the fifth part, conclusions are drawn and a short discussion is provided about how the model can be developed further.

During project execution, literature studies were carried out to collect information about the physical processes involved in the corona discharge and how these are described mathematically. Also, different available sets of data for parameters of the model were analyzed.

CHAPTER

2

CORONA THEORY

In a uniform electric field, exceeding the dielectric strength of the surrounding media usually leads to a complete electric breakdown [2]. If the field distribution between electrodes is strongly non-uniform, e.g. in point-plane, sphere-plane or coaxial cylinders geometries, electrical discharges will be observed before a complete breakdown takes place. These discharges, or partial breakdowns, are commonly described by the term 'corona'.

Certain conditions must be met for corona discharge to take place. As mentioned above, the field distribution must be non-uniform, thus preventing complete breakdown of gap. The voltage applied to the corona electrode must be high enough to ensure electric field strength high enough to initialize ionization of the insulating gas medium. In practice, corona discharges are commonly found at high voltage power lines, or in apparatus being exposed to high voltage stress and are usually considered to be a problem. However, corona can also be utilized in certain industrial applications, e.g. high-speed printing, electrostatic precipitators or Geiger counters [2].

Coronas can be divided into impulse coronas and static field coronas. The first takes place when the voltage level surpasses corona onset voltage for a short duration of time, while the latter occurs when the onset voltage is surpassed over a longer period of time. With the longer time period, phenomena of space charge drift and accumulation can be observed. Coronas can also be classified as positive or negative depending on the polarity of the potential applied to the corona electrode.

This chapter aims to describe physical process in corona discharge, as well as to give a brief overview of the underlying theory. Physical processes that are of greater significance for corona in air such as ionization of neutral molecules, formation and destruction of negative ions, ionic recombination, will be defined and discussed together with descriptions of how these processes can be applied in a theoretical drift-diffusion corona model. Coefficients of importance, such as Townsend's first and second ionization coefficient will be briefly introduced, as well as physical occurrences such as the

importance of the electric field strength, surface charge and space charge and fluxes of ions and how these must be combined to formulate suitable boundary conditions. Finally, a theory of how corona discharge currents can be calculated will be presented.

2.1. GAS LAWS

To get a better understanding of corona discharges it is important to have a clear picture of the physical processes involved. Most gases exposed to normal temperature and pressure abides classic thermodynamic laws. If no external electric or magnet field is applied to a gaseous medium, the gas is in equilibrium meaning that equal amount of ionizing and decaying processes take place. Classic gas laws state that for a constant amount of gas at constant temperature, the product of pressure p and volume V is constant i.e.

$$pV = \text{const.} \quad (1)$$

Through mathematical derivations, e.g. [2], the equation (1) can be expressed as

$$p = N_A k_B T \quad (2)$$

where N_A denotes gas density, k_B is Boltzmann's constant ($= 1.3804 \cdot 10^{-23}$ J/°K), and T is the temperature.

Since a great number of reference values used for high voltage computations is derived from empirical data, it might be necessary to make corrections for differences in atmospheric conditions between different experiments. Corrections for discrepancies in temperature and pressure are accounted for by the usage of the relative air density-factor. The relative air density is denoted by δ and is calculated as

$$\delta = \frac{T_0 p}{p_0 T} \quad (3)$$

where T_0 is the reference temperature ($= 293$ °K), p_0 is the reference pressure ($= 101.325$ kPa), and T and p are the actual temperature and pressure respectively.

2.2. BACKGROUND IONIZATION

Air, at normal temperature and pressure, acts as a good insulator with the electric conductivity in the region of $10^{-12} - 10^{-13}$ S/m [2]. This background conductivity exists due to a final number ($\sim 10^9$ m⁻³) of free charged species (typically ions) created by cosmic radiation and radioactive substances, the so-called background ionization with a characteristic rate R_0 . The rate of background ionization differs

depending on the surrounding environment. Thus, for electron-ion pair appearance in air with normal concentration levels of radon, it is $R_0 \approx 1 - 10$ ion pairs $\text{cm}^{-3} \text{s}^{-1}$, with a corresponding maximum ion pair concentration $n_0 \approx 10^3 - 10^4 \text{ cm}^{-3}$ at equilibrium [3][4]. In the absence of an externally applied electric field, the ionization process is counteracted by a decay processes, and thus equilibrium is sustained.

Each ion pair carries a charge q that equals to the elementary charge of $1.6 \cdot 10^{-19} \text{ C}$, assuming that singly ionized atoms/molecules dominate. Pursuant to Coulomb's law, the charged particles will experience an electrostatic force F when subjected to an electric field E according to

$$F = qE. \quad (4)$$

The force F will create a drift motion for the ions in the gas. The corresponding velocity w of the drifting particles is given by

$$w = \mu E \quad (5)$$

where μ is the mobility of the particle. Particles moving randomly in the gas experience collisions which can be elastic or inelastic. In a weak electric field, elastic collisions dominate. This means that the collisions are purely mechanical, resulting in kinetic energy exchange. Inelastic collisions means that there is an energy transfer from kinetic energy into potential energy between the striking and colliding particle, and vice versa. Inelastic collisions include for example ionization, electron attachment and detachment.

The energy W gained by a particle that is moving a distance λ is described by

$$W = qE\lambda \quad (6)$$

where the free path λ is

$$\lambda = (N_0\sigma)^{-1}. \quad (7)$$

Here, N_0 is the density of gas molecules and σ is the cross-section of the process. By using (2) in (7) together with a typical scattering cross-section $\sigma \approx 10^{-16} \text{ cm}^2$ at normal pressure and temperature, it yields a free path $\lambda = 4 \cdot 10^{-4} \text{ cm}$ [3].

By combining Ohm's law

$$j = \sigma E \quad (8)$$

and the expression for the total current density

$$\mathbf{j} = \mathbf{j}_i + \mathbf{j}_e = n_0 q \mathbf{E} (\mu_i + \mu_e) \quad (9)$$

The conductivity of the gas is obtained as

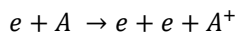
$$\sigma = n_0 q (\mu_i + \mu_e). \quad (10)$$

Since air is a fairly electronegative gas, free electrons do not exist for a long time and, hence, the mobility of electrons μ_e can be disregarded. By using (10) to calculate the conductivity of air σ_{air} due to the background ionization R_0 , the magnitude of $\sim 10^{-13}$ S/m can be obtained. This value is a good match with existing literature [2][5].

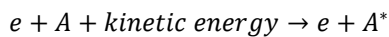
2.3. IONIZATION, DETACHMENT, ATTACHMENT AND RECOMBINATION

If an external electric field is applied, charged particles in the gas will start to move in the direction of the field. With an increase of field strength, the velocity of the charged particles will increase according to (5), thus allowing particles to accumulate higher energies while travelling the free path λ . At high enough energy levels, collisions will switch from being mostly elastic and instead be dominated by inelastic ones, i.e. an energy transfer between the involved particles will take place. The process that is of greater interest when studying electrical discharge is the ionization of gas molecules taking place due to electron impact [6].

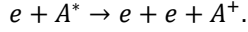
Equation (6) can be used to describe the average energy \bar{W} an electron gain over the mean free path $\bar{\lambda}$ in the direction of the field, according to $\bar{W} = qE\bar{\lambda}$. If the mean energy \bar{W} exceeds the ionization energy of the molecule, eV_i , when impact takes place it will eventuate in ionization. If the energy instead is not high enough, the struck particle may get excited and therefore render the opportunity to get ionized upon impact with a next electron of less energy. The electron impact ionization process can simply be described as



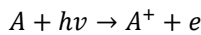
where e , A and A^+ denotes electron, atom/molecule and positive ion respectively. As mentioned earlier, electron impact will not always result in ionization, but instead might lead to excitation of the struck particle. The excitation process can be described as



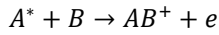
where A^* denotes an excited atom or molecule. If the excited particle is once again struck by an electron, in what is known as step-wise ionization, it can get ionized according to



Another scenario is that the excited particle will recover from the excited state, thus radiate energy as a photon $h\nu$. This happens within a time range of $10^{-7} - 10^{-10}$ s. If the radiated photon strikes a particle with ionizing energy low enough, ionization will take place according to

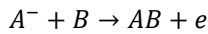


which is known as photoionization. Additional ionization processes that may lead to occurrence of free electrons are associative ionization, which is described by



Associative ionization will not be paid any further attention here, but could be studied from literature as for example [6].

If negative ions are present in gas, associative detachment may occur. This is a process where a negative ion interacts with an atom/molecule, thus render another type of molecule and a free electron, according to



The rate of detachment is described by

$$R_{det} = k_{det}n_nN \tag{11}$$

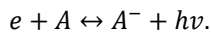
where k_{det} is a detachment coefficient, n_n the concentration of negative ions, and N the density of the gas that can be derived from (2). The detachment coefficient k_{det} is described further in section 2.9.

The varieties of ionization mechanisms can be treated as a generic process that is the case for this thesis. The rate at which the ionization process takes place, R_{ion} , is described by

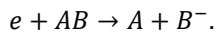
$$R_{ion} = \alpha n_e w_e \tag{12}$$

where α is Townsend's first ionization coefficient, n_e the density of electrons and w_e is the electron drift velocity in the applied field as described by (5). Townsend's first ionization coefficient is described further in section 2.7.

The types of collisions described above are processes that generate free electrons. Naturally, there are also course of events where free electrons are instead attached to ions or atoms/molecules, i.e. deionization. One such process is electron attachment which takes place in electronegative gases. These are gases that lack one or two valence electrons and have a strong tendency to attract free electrons in order to form stable ions. One such gas is oxygen, which lacks two electrons in its outer shell. Attachment can occur in several different ways. Radiative attachment, which is the inverse of photodetachment, can be described by



The process of dissociative attachment, which is predominant in molecular gases, utilizes the excess energy of the electron to split the molecule into a neutral particle and a negative ion [2] and can be described as

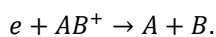


According to [3], for reasons of convenience the intensity of electron attachment can be described by introducing a generic attachment coefficient η , which is described as the number of attaching events occurring on 1 cm of length travelled by the electron in the direction of the field. The attachment coefficient η will be discussed further in section 2.8. Notice the similarity of the ionization coefficient α utilized in (12). Analogously to (12), the rate of attachments R_{att} is described by

$$R_{att} = \eta n_e w_e. \tag{13}$$

It is important to note that the above described approach is only valid in such cases where attachment can be treated as a lumped parameter. If the kinetics of each individual species is of interest, the corresponding rates for the reaction of each species must be considered [3].

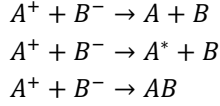
A process that gives rise to loss of electrons and positive ions is dissociative recombination. This process occurs mainly in gases with both large populations of ionized particles, such as plasmas under atmospheric pressure. Briefly, it can be described as the merging of an electron with a positive molecular ion, hence leaving two neutral particles, according to



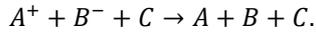
The electron-ion recombination rate R_{rec}^{ei} depends on the concentration of electrons n_e and positive species n_p in the gas and an electron-ion recombination coefficient β_{ei} according to

$$R_{rec}^{ei} = \beta_{ei} n_e n_p. \quad (14)$$

Not all processes include free electrons. Ion-ion recombination, which involves positive and negative ions, may occur as either two-body or three-body collisions; two-body collisions according to



and three-body collisions as



In a two-body collision, the excess internal energy is absorbed by one of the participating ions, while for a three-body collision the excess energy is instead removed by the third participating body [6]. A generalized rate for ion-ion recombination R_{rec}^{ii} can be expressed as

$$R_{rec}^{ii} = \beta_{ii} n_p n_n. \quad (15)$$

This rate depends on the concentration of positive and negative ions, n_p and n_n , as well as an ion-ion recombination coefficient β_{ii} . The recombination rates β_{ei} and β_{ii} will be discussed further in section 2.10.

It is important to know that all the above described collisions are just a selection of the total amount of processes included in the ionization/recombination pattern that is playing a fundamental part in corona glow discharges. They are in some cases also simplified and generalized to facilitate the understanding and modelling of the aggregated discharge process. For a deeper understanding and more complete descriptions of the processes for example [7] can be reviewed.

According to [2], the theoretically derived ionization constants rarely conform to experimental values. The reason for this is the theoretical assumption that every electron with an energy level transcending the ionization energy level will automatically lead to ionization. In reality only a small amount of electrons at the threshold level will cause ionizing collisions. Only at energy levels 4-6 times the ionization energy, a maximum 50 % of the collisions will cause ionization.

2.4. IONIC DRIFT, MOBILITY AND DRIFT FLUX

As mentioned earlier, when a swarm of electrons or ions are subjected to an electric field, it will start to drift in parallel with the direction of the field. The center of the swarm mass will gain a velocity $w = \mu_i E$ as described in (5). The mobility for any species in gas can be defined as

$$\mu_i = \frac{q_i}{m_i v_m} \quad (16)$$

where q_i is the charge of the species, m_i the mass, and v_m is the momentum transfer collision frequency. By using (5), the mobility of each species can also be described as

$$\mu_i = \frac{w_i}{E} \quad (17)$$

where w is average drift velocity of the particular species and E is electric field strength. Mobility of the species is in general a characteristic of the specific gas the ions constitute.

To make corrections for the differences in atmospheric conditions, the ionic mobility μ_i is divided with the relative air density factor δ . The corrected mobility coefficient is used to calculate the flux of each species due to the applied electric field according to

$$\Gamma_{drift} = \mu_i n_i E. \quad (18)$$

Drift together with diffusion are the components that make up the total flux that sets ions and electrons in motion in discharge plasma.

2.5. DIFFUSION AND DIFFUSION FLUX

Diffusion is a general term that is used to describe the movement of particles/mass from an area of higher concentration to an area of lower concentration. Diffusion is a natural occurring phenomenon which eventually will lead to equilibrium in any steady-state process. In corona discharge, diffusion will take place whenever a non-uniform concentration of charged species, i.e. a concentration gradient, exists. The subsequent impact will be an ionizing effect in regions of low concentration, and a correspondent deionizing effect in regions of high concentrations.

In the case of low field strength, i.e. when the velocity obtained from the external field is lower than the average velocity, the influence of diffusion on velocity will have greater impact. The ion concentration gradient will impose a force on the charged particles resulting in drift velocity in a way analog to the effect of the electric field in (18). Flux caused by diffusion Γ_{diff} is described by

$$\Gamma_{diff} = -D_i \nabla n_i \quad (19)$$

where D_i is a diffusion coefficient and ∇n_i is the concentration gradient of the species in question. The diffusion coefficient D_i for each ion species is linked to mobility μ_i through what is known as Einstein's relation, which is described by

$$D_i = \mu_i k_B \frac{T_i}{q}. \quad (20)$$

Here μ_i , k_B , and q stand for ion mobility, Boltzmann's constant and elementary charge respectively, and T_i describes the ionic temperature, which is field dependent, and can be evaluated through the expression

$$k_B T_i = k_B T_a + \frac{1}{3} (m_i + m_m) w_i^2. \quad (21)$$

Here T_a represents ambient air temperature, m_i and m_m are ion and molecule mass respectively, and w_i is the particle drift velocity described by (5).

2.6. HYDRODYNAMICS AND SOURCE TERMS

In a closed system, if all quantities involved are conserved, their transport can be described by a continuity equation. In a system where particle movement is governed by drift and diffusion, the continuity equation can be formulated in a general way by the Smoluchowski equation as

$$\frac{\partial c}{\partial t} = \nabla(D\nabla c) - \nabla(\mathbf{w}c) + S \quad (22)$$

where c is the variable of interest, D is the diffusion coefficient described in (20), \mathbf{w} the velocity variable described in (5), and S is a source or sink term which describes the increase or decrease of the quantity denoted by c . For derivation of the drift-diffusion balance equation for example [8] and [9] can be studied.

The source term S is made up by the process relevant to the plasma physics described in (12) - (15). As previously stated, the corona discharge is constituted by multiple processes, although some makes a more significant contribution. For each charged species; electrons, positive ions and negative ions, their respective source terms can be approximated as

$$S_e = R_0 + R_{ion} + R_{det} - R_{rec}^{ei} \quad (23)$$

$$S_p = R_0 + R_{ion} - R_{rec}^{ei} - R_{rec}^{ii} \quad (24)$$

$$S_n = R_{att} - R_{det} - R_{rec}^{ii} \quad (25)$$

By using the source terms in (22), the dynamics of the charged species in the discharge plasma can be described by the set of PDEs

$$\frac{\partial n_e}{\partial t} + \nabla(-n_e \mathbf{w}_e - D_e \nabla n_e) = S_e \quad (26)$$

$$\frac{\partial n_p}{\partial t} + \nabla(n_p \mathbf{w}_p - D_p \nabla n_p) = S_p \quad (27)$$

$$\frac{\partial n_n}{\partial t} + \nabla(-n_n \mathbf{w}_n - D_n \nabla n_n) = S_n \quad (28)$$

for each type of species, respectively. The drift component in (26) and (28) is implemented with a negative sign to signify movement against the electric field. Formation of positive ions and injection of ions mostly take place in the high field region, while formation of negative ions in air is entirely due to the oxygen content and occurs mostly in the low field area. Energy of species are not included in this model, hence there is no ion or electron inertia either.

2.7. TOWNSEND'S FIRST IONIZATION COEFFICIENT

Townsend's ionization coefficient α is defined as the number of ionizing collisions caused by one electron while moving one centimeter in the direction of the electric field. The total number of electrons n produced by one initial electron over a distance d is then given by

$$n = n_0 e^{\alpha d} \quad (29)$$

where n_0 is the initial number of electrons. Although α is a well investigated parameter, it cannot easily be calculated. As α is used to describe the behavior of a swarm of electrons, additional information about drift velocity and energy distribution for participating electrons must be known to perform accurate calculations [6]. For a constant temperature of a gaseous media, the energy distribution \bar{W} only depends on the field/pressure ratio E/p . Therefore, for a given energy distribution the ionization probability will be dependent on the gas pressure p [2]. Thus, the first ionization coefficient α can be expressed as

$$\alpha = p f(E/p) \quad (30)$$

or

$$\alpha/p = f(E/p). \quad (31)$$

Since pressure p is proportional to gas density N , $p \propto N$, equation (31) can be rewritten as

$$\alpha/N = f(E/N). \quad (32)$$

This relationship between the ionization coefficient α and the reduced field strength E/N has been verified through experiments as well as values derived through calculations. For examples of how experimental measurements are performed [9] can be consulted.

2.8. ATTACHMENT COEFFICIENT

Attachment of electrons is the process in corona discharge that leads to a depletion of electrons in the ionization region. The attachment process in air can be described by four processes; dissociative attachment, ion pair formation, three-body attachment and radiative attachment. The first and last of the aforementioned processes depends on the ion density N in the same way as α , while the three-body process depends on N^2 . The ion pair formation process does not remove electrons from the swarm; hence it does not have any effect on α [9]. The rate of attachment in air is different than the rates of separate components, and depends on, for example, humidity as water molecules will also attach electrons.

According to [10], the attachment coefficient η can be calculated as

$$\eta = \frac{1}{x_2 - x_1} \ln \frac{I_1}{I_2} \quad (33)$$

where x_1 and x_2 are two arbitrary points making up the edges of the geometry and I_1/I_2 is the ratio of currents measured in the respective points. However, this approach will not be utilized in the model developed in this thesis, but is mentioned more as a theoretic reference. Instead the attachment coefficient utilized in the model will be implemented through tabulated values, and is described further in section 4.6.

2.9. DETACHMENT COEFFICIENT

The rate of detachment is determined by the gas density N , the concentration of negative ions n_n and the detachment coefficient k_{det} . Detachment, as given by the name, is the process where electrons detach from ions and thus only negatively charged ions are involved. To determine an accurate detachment coefficient, the ion composition of the plasma must be known. However, according to [11] a generic coefficient k_{det} for air can be calculated as

$$k_{det} = 2 \times 10^{-16} \exp\left(-\frac{6300}{T_i}\right). \quad (34)$$

Here an abundance of O_2^- ions is assumed. The parameter T_i is the effective ion temperature which is calculated according to (21).

2.10. RECOMBINATION COEFFICIENTS

Recombination is the process where charged particles, i.e. electrons and/or ions, recombine to form neutral species, i.e. atoms or molecules. Recombination occurs as either electron-ion recombination or as ion-ion recombination. Results presented by Sayers in [12] shows that the coefficient of ion-ion recombination β_{ii} is dependent of pressure and can be described as

$$\beta_{ii} = k_{ii}N_A \quad (35)$$

where k_{ii} is the corresponding recombination rate constant and N_a the number of molecules in the gas. Therefore, β_{ii} when combined with (2), can be written as

$$\beta_{ii} = k_{ii} \frac{p}{k_B T} \quad (36)$$

where p is pressure, k_B is Boltzmann's constant, and T is absolute temperature. However, at pressures around 1 atm fluctuations have a small impact on the ion-ion recombination coefficient and according to [13], β_{ii} can be expressed as

$$\beta_{ii} = 2 \times 10^{-6} \left(\frac{300}{T_i} \right)^{1.5} \quad (37)$$

where T_i is the ion temperature and can be calculated as (21).

The electron-ion recombination coefficient β_{ei} depends mostly on the composition of the ions; simple ions like N_2^+ , O_2^+ and NO^+ will yield one value, while complex ions like N_4^+ , O_4^+ , $N_2O_2^+$ will yield a different value.

2.11. TOWNSEND'S SECOND IONIZATION COEFFICIENT

In a positive corona discharge, positive ions will move towards the cathode as they are being repelled from the anode. The impact of positive ions upon the cathode may induce injection of secondary electrons. The rate of emission of electrons is known as Townsend's second ionization coefficient γ . It has been shown that γ is dependent on electric field strength, gas pressure, the nature of the gas as well as the material and state of the electrodes [6].

2.12. ELECTRIC FIELD

As might have been noticed, most the previously considered processes are dependent of the electric field strength E . The electric field strength is usually obtained using Poisson's equation which is a PDE of elliptic type. Maxwell's first equations; Gauss' law for electricity, is stated as

$$\nabla \varepsilon \mathbf{E} = \rho \quad (38)$$

where ρ is the space charge density and ε the dielectric permittivity. The electric field \mathbf{E} is defined as a gradient of the scalar electric potential ϕ that can be expressed as

$$\mathbf{E} = -\nabla \phi \quad (39)$$

By combining (38) and (39), Poisson's equation is obtained as

$$\nabla(\varepsilon_0 \varepsilon_r \nabla \phi) = -\rho \quad (40)$$

where ε_0 is the permittivity of free space, ε_r is the relative permittivity, and ρ is the density of charges contained within the discharge domain.

2.13. SURFACE CHARGE

Surface charge is the charge present at the interface between two media. Surface charge density σ is defined as the amount of charge q present at a given area A , as

$$\sigma = q/A. \quad (41)$$

When a dielectric is placed in the discharge plasma, such an interface emerges. The rate of surface charge build up is dependent on fluxes of positive and negative species according to

$$\frac{\partial \sigma}{\partial t} = q(|\Gamma_p| - |\Gamma_n|) \quad (42)$$

where q is elementary charge, and Γ_p and Γ_n is the flux of respective charged particles. From theory in [14], it can be assumed that electrons and ions at the surface recombine instantaneously, and neutral particles are absorbed through the boundary, thus only leaving charges at the surface.

Surface charges affect the electric field. Together with the space charge, surface charge can be included into the right hand side of Poisson's equation (40). The accumulation of surface charge is therefore of great interest especially in low frequency application at dielectrics where no penetration into the material occur. In such cases, the charges have sufficient time to accumulate before dislodging in the opposite direction, and therefore might really influence the local field strength at the gas-solid interface.

2.14. SPACE CHARGE

During the ongoing process of a corona discharge, the accumulation of space charge in the gas region is a continuous process. Space charge accumulation has a considerable effect on how the electric

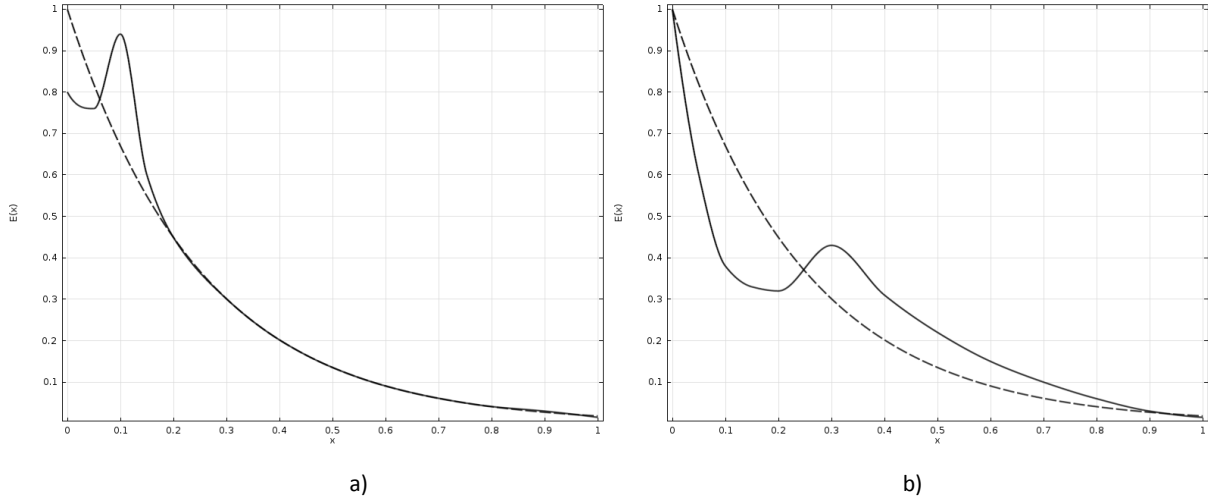


Figure 1. Distortion of the electric field due to space charge accumulation at a) positive voltage polarity and b) negative voltage polarity.

field is distributed in gas and lead to either interruption or an enhancement of the corona that may even result in a complete breakdown [15]. The effect of space charge build up is also crucial for transformation of an electron avalanche into a streamer.

The space charge density ρ is calculated as

$$\rho = q(n_p - n_e - n_n) \quad (43)$$

where q is the elementary charge and n_p , n_e and n_n are the concentrations of the charged species. The nature of space charge in corona is mainly ionic. Electrons created in a high field region at the corona electrode (also called ionization sheath), travel in the field at high velocity since they have much smaller mass than ions. Hence, electrons reach the anode/cathode before ionic species and can be absorbed. Ions, moving slower, remain in the gap and mainly constitute the space charge. Influence of free ions on the discharge process differ depending on the composition of gas medium, but in electronegative gases both positive and negative ions contribute to the space charge field [9].

At high density of accumulated space charges the field in the gas gap can be altered. Thus, in case of positive polarity of the corona electrode, when electrons are absorbed by the anode, slower moving positive ions cause a reduction of field strength in the area closer to the anode coincident with an augmentation of the field at a further distance. At a negative voltage, electrons are repelled from the corona electrode and drift away from it entering the region with relatively low field strength. In electronegative gases, these electrons are attached to electronegative molecules while positive ions tend to be trapped between the anode and the negative charges. Therefore, the field at the anode is greatly enhanced, but the size of the ionization region is instead reduced a lot. This might lead to a

termination of the ionization, and the space charge drift away from the cathode area according to the direction of the field. Distortion of the field for both coronas of both positive and negative polarity is visualized in Figure 1 a) and 1 b), respectively.

2.15. DISCHARGE DEVELOPMENT

Conditions for corona inception have been thoroughly investigated by numerous authors. Different electrode geometries (wire or cylinder, point or spheres, wire radius, etc.), voltage polarity, gas temperature and gas pressure have been studied in [15-[22]. Thus, the famous work by Peek [17] resulted in the empirical equation for corona onset electric field strength E_c at the surface of a cylinder, stated as

$$E_c = 30\delta \left(1 + \frac{0.3}{(\delta R)^{1/2}} \right) \quad (44)$$

where δ is the relative air density and R is radius of the wire. Equation (44) is known as Peek's equation. Reference temperature and pressure for validity of this equation are 25°C and 1 atm respectively.

A semi-empirical way of defining corona inception conditions is based on the fact that corona can be considered as a partial breakdown of gas at the electrode providing strong electric field. Thus as it is known [23], Townsend's breakdown criterion governs the onset of negative corona while the streamer inception criterion governs the onset of positive corona. In general and independently of the polarity, the breakdown criterion can be expressed as

$$\exp \left(\int \alpha' dr \right) = Q, \quad (45)$$

Here, the integration is to be performed over the ionization region, where α' (the net ionization coefficient) is larger than zero, dr is the element along the integration path, and Q is a constant. The net ionization coefficient is here considered as the difference between the actual ionization coefficient and the attachment coefficient $\alpha' = \alpha - \eta$. For Townsend's breakdown criteria where breakdown is due to the yield of secondary electrons from the cathode, the constant $Q = 1/\gamma$, where γ is Townsend's secondary ionization coefficient. For the streamer breakdown criteria where the space charge field gains magnitude of the breakdown fields, Q is instead the number of electrons necessary to create a space charge field with high enough magnitude.

According to the classical theory, as voltage between the two electrodes increases, a discharge current increases according to

$$I = I_0 \frac{e^{\alpha' d}}{1 - \gamma(e^{\alpha' d} - 1)} \quad (46)$$

where I_0 is the initial current (e.g. due to background ionization), α' is the first ionization coefficient, γ is the second ionization coefficient, and d is the distance between the two electrodes. At high enough voltage levels, the discharge transforms into a self-sustained discharge, and the current in (46) becomes mathematically indefinable. At this point, the condition of breakdown

$$\frac{\alpha\gamma}{\alpha - \eta} [e^{(\alpha-\eta)d} - 1] = 1 \quad (47)$$

becomes valid. In theory, the discharge current could become infinitely large, but it is actually limited by the external circuit. Equation (47) is commonly known as Townsend's breakdown criterion. It can be approximated by

$$\gamma e^{(\alpha-\eta)d} = \gamma e^{\alpha' d} = 1 \quad (48)$$

that is known as the ionization threshold. For $\gamma e^{\alpha' d} > 1$ the discharge continues to develop independently of the external current I_0 , i.e. the discharge is self-sustained. For $\gamma e^{\alpha' d} < 1$, formation of new avalanches do not take place and if I_0 is removed the discharge will be quenched.

During a Townsend discharge the electrons will travel in the plasma from cathode to anode. For the Townsend breakdown mechanism to be fulfilled and the discharge to be sustained electrons must be replaced near or at the cathode. The renewal of electrons is usually due to impact of positive ions at the cathode, emitting secondary electrons, as described in section 2.11. It can also be caused by photoelectric emission of electrons which is due to impact of photons emitted by the avalanche. Without such a replenishing process, all electrons in the plasma will eventually travel to the anode, and hence the discharge will be quenched.

If the rate of ionization surmounts the rate of losses of electrons, an increasing number of electrons will be available in the gas for collision with neutral particles to form positive ions and additional free electrons. This leads to so called electron avalanches, where electrons and positive ions are created at an exponential rate according to

$$n_{e,p} = n_0 \exp(\alpha d). \quad (49)$$

The avalanche, or swarm, will drift with the field; faster electrons will form the head drifting towards the anode while slower positively charged particles will form the tail drifting towards the cathode.

Electrons that reach the anode will be absorbed, leaving only the positive ions in the discharge domain. If ion concentration due to the avalanche continues to grow surpassing a number of 10^8 , the Townsend discharge might transcend into a streamer.

The streamer breakdown mechanism is instead dependent on the strength of the space charge field. If the electron avalanche takes on such proportions that the space charge field surpasses the magnitude of the breakdown field the streamer breakdown can proceed. This process is independent of the polarity of the corona, i.e. corona can be either positive or negative.

2.16. DISCHARGE CURRENTS

Corona discharge naturally gives rise to a current in the gas. The total current flowing between the electrodes in the discharge region can be described as

$$I_{tot}(t) = I_{ion}(t) + I_{disp}(t) \quad (50)$$

where I_{ion} is the ionic current component and I_{disp} is the displacement current component. These components can be calculated as

$$I_{ion} = A J_{ion} = AqE(n_p\mu_p - n_n\mu_n - n_e\mu_e) \quad (51)$$

$$I_{disp} = A J_{disp} = A \left(\varepsilon \frac{\partial E}{\partial t} \right). \quad (52)$$

Here A is the area of the electrodes and J is the current density. The displacement current in its turn consists of two components; one part due to geometrical capacitance of the domain and one part due to the space charge in the gap influencing the dynamic electric field. The capacitive current is calculated as

$$I_{cap0} = C \frac{dU}{dt} \quad (53)$$

where U is applied voltage and C is the capacitance, which for concentric cylinders is calculated as

$$C = \varepsilon \frac{2\pi h}{\ln(d_{outer}/d_{inner})}. \quad (54)$$

In (54), h is the height of the geometry, ε is the permittivity of gas, d_{outer} and d_{inner} are the diameters to the outer and inner electrodes in the coaxial system, respectively.

In the experiment conducted at ABB Corporate Research described in Chapter 3, the current that was measured at the cylindrical cage side was the total current described by (50). However, since the capacitive current component is constant for a given voltage level, the current shown for representation is chosen as total current minus the capacitive component. Hence, the current representation is given by

$$I_{repr}(t) = I_{ion}(t) + I_{disp}(t) - I_{cap0}(t) \quad (55)$$

with each current component as described in (51), (52) and (53) respectively.

CHAPTER

3

EXPERIMENTAL MEASUREMENTS

To study the behaviour of space charges in a corona discharge, a series of experiments has been conducted at ABB Corporate Research in Västerås, Sweden. In the measurements, time dependencies of corona currents in well-controlled environment have been recorded.

3.1. EXPERIMENTAL SETUP

Basically, two different experimental setups have been utilized; in the first one a wire was suspended in free air, and in the second a wire was encased by a insulating cylinder. Only the second experiment is of interest in this thesis.

The experiments were conducted utilizing a coaxial geometry with the wire surface as the inner electrode and a metallic cage as the outer electrode as shown in Figure 2. The corona current was measured at the outer electrode. To shield the experiment from external noise, an additional shielding cage was used. Two different wire diameters have been used; $d_{w1} = 0.5$ mm and $d_{w2} = 0.26$ mm. The insulating cylinder made of PVC had inner diameter of $d_i = 376$ mm and thickness $r_i = 13$ mm. The shielding cage had a diameter of $d_c = 2.5$ m. The height of both the wire and the shielding cage was 2.5 m, while the insulator tube has a height of 3 m.

3.2. EXPERIMENTAL RESULTS

The voltage applied to the wire was a triangular shaped AC with the magnitude of 20 kV. By utilizing the triangular shape, grow and decay rate were kept constant and always known and thus enabling possibilities for a more accurate analysis of results. For experiment where an insulator was incorporated into the geometry, only two frequencies has been tested; 1 Hz and 0.1 Hz. Plots of the experimental results (measured corona voltage-current characteristics) for these two frequencies is shown in Figure 3. To make comparisons easier, the current displayed is the total current according to (50), I_{tot} , with the linear capacitive current component, I_{cap0} , in (53) subtracted.

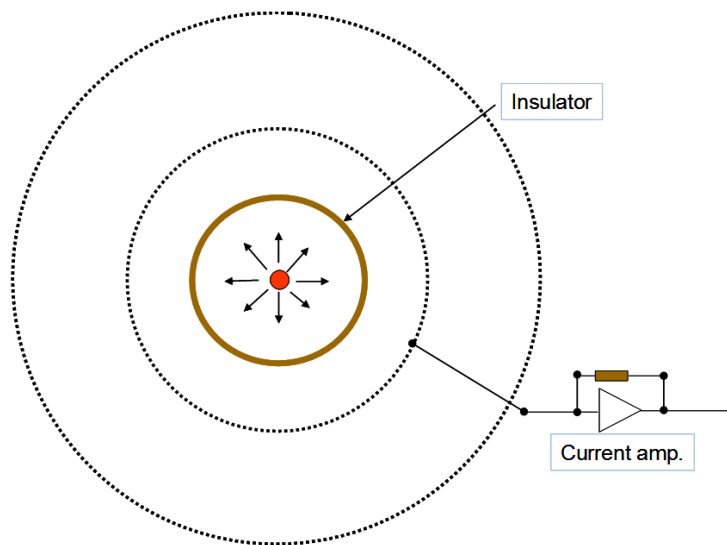


Figure 2. The sketch of the experimental setup utilized by ABB Corporate Research. The middle point is the energized corona wire, the first circle from the center is the PVC-barrier, the second circle is the metal cage where current is measured and the outer circle is the disturbance shield.

As seen, the discharge voltage-current characteristics adopt a “butterfly-like” shape due to the AC triangular shaped voltage applied. One may notice that the corona onset voltage is rather independent of the frequency. According to [1], this is not the case when the discharge media is free from any obstacles, e.g. the PVC-barrier is not included; instead a higher frequency renders a lower corona onset voltage. This observation can be explained by comparing the mean passage time needed for an ion to drift through the discharge volume (time of fly between the electrodes) with the period of the applied electric field. At high frequencies, the former is longer than the latter and this holds true even for voltage levels that is high enough to sustain the corona discharge, and hence contributes to accumulation of charges in the gap. The consequence of this is that charges generated during half of the period are left in the gap when the polarity of the voltage changes and an electric field due to the space charge exists even at voltage zero crossing. Moreover, the onset voltage is lowered due to availability of the initial charge carriers at relatively high densities. Note that the onset field strength does not change; the change is that a lower voltage is required to initiate corona. Further, space charge behavior is essential for corona current development. Thus, assuming for clarity that the voltage is changing from negative to positive, negative charge from the negative half cycle that is still remaining in the gap is attracted to the corona wire to be partly neutralized. The electric field within the ionic cloud is expected to be relatively constant, and thus the main voltage drop takes place at the edge of the charge cloud and the outer electrode. At maximum voltage, the voltage derivative dU/dt changes sign and, hence, create a capacitive current in the opposite direction which nullifies a part of the resistive current.

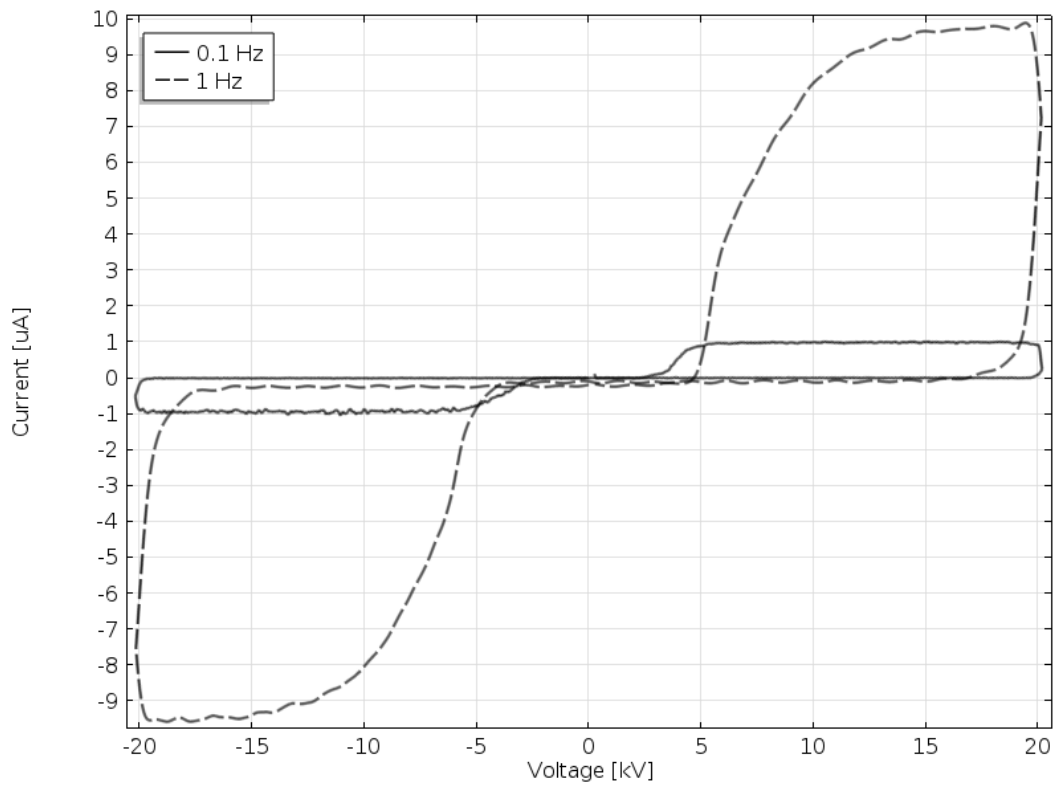


Figure 3. The experimental results acquired by ABB Corporate Research when utilizing a setup with a PVC-barrier and a voltage level of 20 kV.

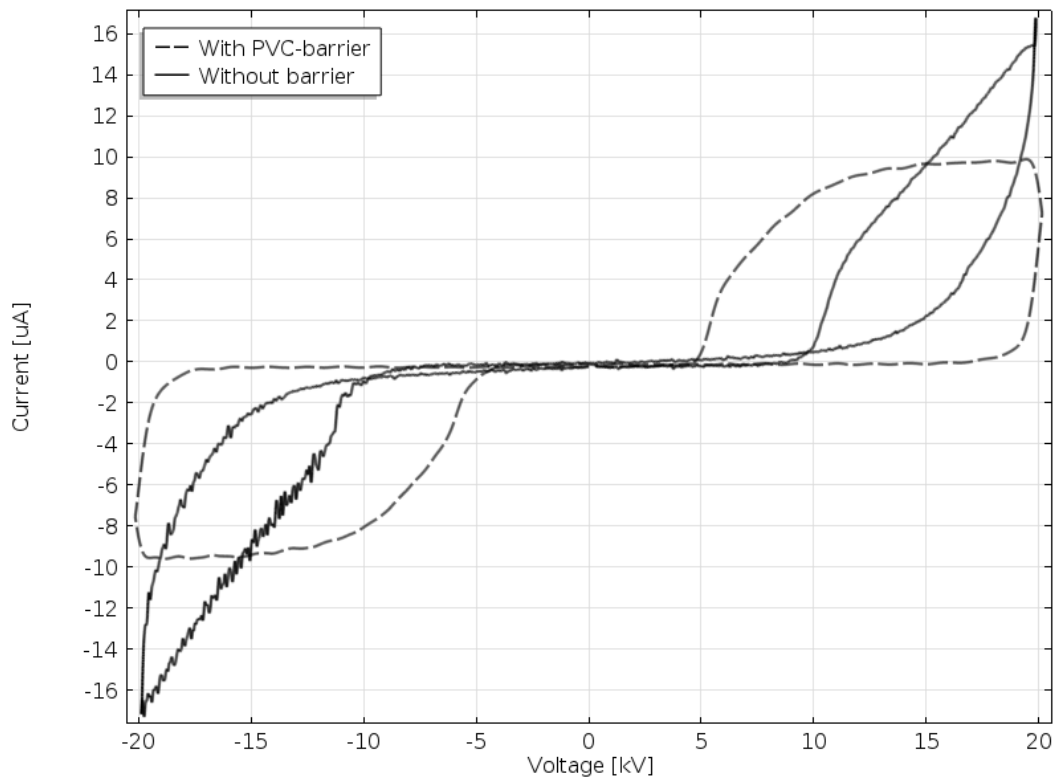


Figure 4. A comparison of experimental results from ABB Corporate Research for geometries with and without a PVC-barrier with a voltage with a magnitude of 20 kV and a frequency of 1 Hz applied.

As mentioned above, the linear capacitive current element is already deducted from the total current that leads to the conclusion that the capacitive current element must be nonlinear. This nonlinear current contribution can be assigned to the capacitance made up from the edge of the charge cloud. As the capacitive current is fully relaxed, the resistive current component will continue to a decrease only for the same procedure to be repeated with reversed polarity.

The inclusion of a PVC-barrier within the discharge volume results in the above described charge cloud being accumulated on the barrier surface instead. Corona onset will be reached at even lower voltages than in case of free air as seen in Figure 4. Charges confined in the anode-barrier domain enhance the field even further. The relaxation time of the charge accumulated at the barrier is typically very long. Once the barrier surface is charged, it will not be discharged until it is being recharged by corona with a different polarity. Therefore, onset voltage in a setup including the PVC-barrier becomes almost independent on frequency.

CHAPTER

4

MODEL IMPLEMENTATION

Modelling corona discharge currents for both positive and negative polarities is conducted considering discharges as being homogeneous in the radial direction between corona wire and cylindrical cage. The simulation model used is an extended version of the model presented in [1], which in its turn is a continuation of work done in [24]. Implementation of the model is presented below.

When solving and analyzing physical systems a method of deriving differential equations that relates concerned variables through physical principles such as Maxwell's equations, laws of thermodynamics, Newton's laws of motion, energy conservation, mass conservation, or equilibrium is often employed. Once such a problem is formulated, solving the mathematical model often proves to be close to impossible. The resulting models are often non-linear partial differential equations with complex geometries and boundary conditions. To be able to solve such intricate problems the finite element method (FEM) can be employed.

All modeling and simulations of the corona discharge current presented in this thesis are performed using finite-element package COMSOL Multiphysics which is widely considered to be the prime choice for problems where coupled PDEs are to be solved. In [1] version 4.3a was employed while for this thesis the latter version of 4.4 is utilized.

FEM can be described as a discretization technique where the continuum domain is divided into components (elements) of a simple geometry separated by imaginary lines or boundaries. These elements are connected to each other with a discrete number of nodal points that are situated at the element boundaries. The value of each element is given in terms of a finite number of degrees of freedom (DOF) that is characterized as the value of an unknown function at a set of nodal points. The solution to the mathematical model is then the approximation obtained from connecting or assembling all of the elements in the discrete model.

When running complex simulations there is always a problem with having enough computational power. To ensure that as little computer power as possible is claimed by the software, the model geometry should be kept as coarse and straightforward as possible but still deliver accurate results. Since the problem of interest is of cylindrical coaxial electrode geometry the simulated area can be described by a 1D axisymmetric domain. This means that the computational domain will consist of a radial slice with infinitesimal height extending from the surface of the wire to the surface of the cage described in Chapter 3.

COMSOL Multiphysics operates in a way where different physical aspects are implemented through so called physics-nodes. Each node creates a physics group, where sub-nodes can be added to accommodate for different functions. Each node and sub-node constitutes a set of mathematical equations that corresponds to the name of node. The equations included in the node are then added to the list of equations to be solved, e.g. the sub-node Convection and Diffusion governs the equations in (22) or Electric Potential-node applies a voltage to a domain point. Sub-nodes can either be valid for boundaries, i.e. for certain points in the geometry, or for whole domains. Usually each node or sub-node requires certain values or parameters/variables to be inputted by the user.

To select parameters or values for input in a corona discharge model is not always an easy task. A great number of scientific publications by various authors are available on the subject, where some are based on experimental results and some based on simulations. Differences in ambient conditions and/or accuracy in the corona models results in discrepancies between different authors. Parameter values in this thesis are primarily based on the choices made in [1]. According to Karman, it is supposed that [25] and [9] provide accurate data and, therefore, they also act as a base for values in this thesis. However, these parameters are going to be investigated and evaluated to provide a best fit to the experimental results.

In this chapter the way of how to implement the problem in COMSOL is described step by step, as well as how parameters and variables have been defined and chosen. It provides thorough descriptions of what physics are implemented, as well as how the settings are defined for these, how the meshing is applied and, finally, how the settings for the calculations are defined and how the calculations are performed.

4.1. GEOMETRY AND MATERIALS

The geometry of the problem utilizes axial symmetry of the actual geometry, i.e. the computational domain extends from the surface of the wire to a termination point at the grounded cylinder previously described in Chapter 3, as shown in Figure 5.

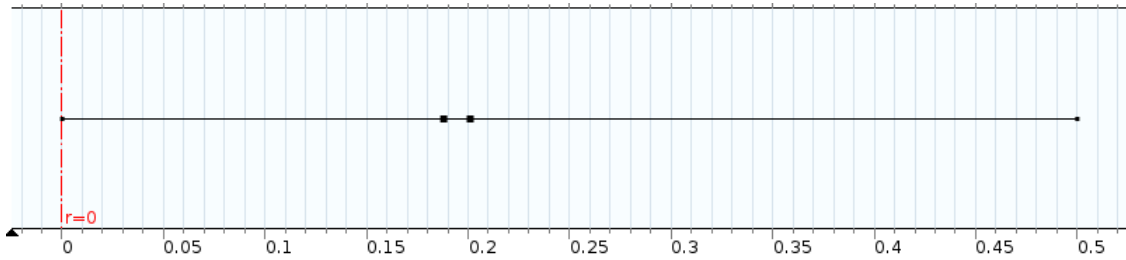


Figure 5. The geometry of the discharge domain as implemented in COMSOL Multiphysics. The leftmost point represents the wire where the voltage is applied, the two points in the middle represents the PVC-barrier, and the rightmost point represents the cage and ground side.

Table 1. Material properties assigned to the computational domains.

Material:	Relative permittivity ϵ_r :
<i>Air</i>	1.0
<i>PVC</i>	3.5

The leftmost point represents the surface of the inner coaxial electrode, i.e. the cylindrical wire, while the rightmost point represents the surface of the outer coaxial electrode, i.e. the cage-side. This is realized using an interval with the left endpoint defined at 0.13 mm and the right endpoint defined at 0.5 m. The surfaces of the PVC-barrier are indicated by two points located at 188 mm and 201 mm respectively. Further, under the *Material*-node, two materials are created of which properties (permittivities) are shown in Table 1 and are essential for calculations of the electric field. Air is applied to the leftmost and rightmost subdomains in Figure 5 while PVC is assigned to the barrier domain.

4.2. ELECTROSTATICS

The *Electrostatics*-physics is found in the *AC/DC*-module and is the physics application for computing the electric field strength utilizing Poisson's equation described in section 2.12. By default, a number of sub-nodes will be implemented when Electrostatics is applied. The *Charge Conservation*-node governs the charge conservation according to Gauss' law and constitutes the left hand side of the

equation (40). It is valid for all three of the computational domains. The setting for the relative permittivity is set to *From material*, i.e. the values given for relative permittivity in the materials settings previously described is used. The sub-node *Ground* is applied to the rightmost point (representing cage side) in Figure 5 while the sub-node *Electric Potential* is applied to the leftmost point (corona wire). The *Electric Potential* boundary condition applies a user input voltage $V = V_0$ (see section 4.9 for details). Since space charges only will appear in air, the sub-node *Space Charge Density* is implemented and only applied to be valid for the air domains, thus no space charge is assumed to exist inside the PVC-barrier. The sub-node demands a user input value for the space charge ρ_v , where a variable named *rho* is used (see a descriptions of *Variables* below in section 4.11). This node constitutes the right hand side of equation (40). At each side of the PVC-barrier a sub-node *Surface Charge Density* is applied. The surface charge, just as the space charge, adds to the total charge in the Poisson's equation. These sub-nodes account for all the charges accumulating at the surface of the PVC-barrier and are therefore no longer considered as space charges. The surface charge density is calculated as

$$\mathbf{n}(\mathbf{D}_1 - \mathbf{D}_2) = \rho_s \quad (56)$$

The transition from space charge to accumulated surface charge is described in the next chapter.

4.3. TRANSPORT OF DILUTED SPECIES

The physics node *Transport of Diluted Species* implements the drift-diffusion continuity equation (22) and can be found in the *Chemical Species Transport*-module. One physics node is added for each type of the charged species in the model, i.e. positive ions, negative ions and electrons and results in three such nodes in the model. Each node is given a dependent variable denoted *e* for electrons, *pos* for positive ions and *neg* for negative ions. Even though several species can be implemented through one physics node, this way have been chosen to make evaluation of simulation results more lucid. Since the barrier is assumed to work as a discontinuity (obstacle for the drift and diffusion), no transport of species takes place within the barrier. Hence, these physics are only applied to the air domains. As for *Transport Mechanisms*, the *Convection* option is chosen.

As for numerical stabilization methods, consistent and inconsistent stabilization can be chosen. In the former case both streamline diffusion and crosswind diffusion is selectable, while in the latter case isotropic diffusion can be selected. Isotropic diffusion dampens oscillations and impedes their propagation in the simulation that smoothens out sharp edges and derivatives of functions. The

tuning parameter δ_{id} is here given the value ad_p , which is defined in the list of constant parameters described in section 4.10.

The sub-node *Convection and Diffusion* governs the left hand side of the set of equations (26)-(28). The *Velocity Field* \mathbf{u} is implemented according to (5) utilizing the corresponding mobility variables (μ_e, μ_n, μ_p) and the inbuilt variable for electric field strength. The *Diffusion Coefficients* D_e, D_{pos} and D_{neg} are defined as the variables D_e, D_p and D_n respectively. How values for mobility and diffusion parameters are chosen is explained further in sections 4.7 and 4.8.

The sub-node *Reactions* is utilized to implement the right hand side of (26)-(28), i.e. the source terms of the drift-diffusion equations. The input values for each *Reactions*-node is given by the variables $source_e, source_p$ and $source_n$ which are implemented as described in the set of equations (23)-(25). Details on these variables are provided in section 4.11.

The sub-node *Flux* is used to describe how the charged species moves into and out of the computational area over the boundaries. Correct functionality of ionic and electron fluxes is of outermost importance, especially in low frequency simulations, where the species have sufficient time to travel the distance through the entire computational domain and may reach counter electrodes. The charged species move either in the direction or in the opposite direction of the electric field and, hence, it is important that the fluxes follow the changes in the electric field. As previously discussed, both diffusion and convection are assumed to have impact on the movement of the charged species, but for boundary fluxes it is assumed that only convective flux makes an impact. All fluxes are by default assumed to be inwards. Hence, outward fluxes needs to be compensated with a negative sign. Each boundary flux is assigned its own sub-node and its own flux variable as indicated in section 4.12.

For each charged species, a sub-node *Outflow* is also introduced which implements zero diffusive flux of charged species at metallic surface

$$-\mathbf{n}D_i\nabla c_i = 0. \tag{57}$$

This sub-node is applied also to the points on each side of the PVC-barrier. Once again, convection is assumed to be the dominating mechanism for transport and this node is used due to the fact that the charged species reaching the PVC-barrier will be accounted for through calculations described in the next chapter, and therefor needs to be removed to not be accounted for twice.

4.4. BOUNDARY ODEs AND DAEs

The node *Boundary ODEs and DAEs* is introduced through the *Mathematics*-module, a module used to implement partial differential equations independent of a specific physical application. The boundary ODE is used here to account for the surface charge accumulation described in section 2.13 and is also the reason why the *Outflow*-node is used as mentioned above. The sub-node *Distributed ODE* is added by default, and is also the one used here. The ODE is implemented as

$$e_a \frac{\partial^2 u}{\partial t^2} + d_a \frac{\partial u}{\partial t} = f. \quad (58)$$

If $e_a = 0$, equation (58) is identical to (42), where $d_a = 1$ and f is the source term described by

$$f = q(|\Gamma_p| - |\Gamma_n| - |\Gamma_e|). \quad (59)$$

For reasons of simplicity when making evaluations, two Boundary ODEs are implemented, one for each side of the PVC-barrier. When charged species and electrons move towards the PVC-barrier the *Outflow* accounts for them leaving the air domain. The ODEs calculate the rate of the accumulation. These values are then used as input for the surface charge in the Poisson's equation in the *Electrostatics*-node described in section 4.2.

4.5. REDUCED IONIZATION COEFFICIENT

The reduced ionization coefficient α/N is used to calculate the ionization rate R_{ion} as described in equation (12). As discussed in section 2.7, the reduced ionization coefficient is not always easy to determine. The values of α/N that are used in this model are the tabulated ones from [9] (see Appendix 1), which in their turn are based on experimental values from [26] and [27]. They are shown in Figure 6 in graphical form. Implementation of the data is done by using the *Interpolation Function* that is found under the *Global Definitions*-node.

4.6. REDUCED ATTACHMENT COEFFICIENT

The reduced attachment coefficient η/N is used to calculate the attachment rate R_{att} as previously described in (13). Analogous to α/N , the reduced attachment coefficient η/N is dependent of the reduced electric field strength E/N as shown in Figure 7 (see also Appendix 1). As seen, the values of η/N are quite high in the low field region and decreases rapidly with the increasing field.

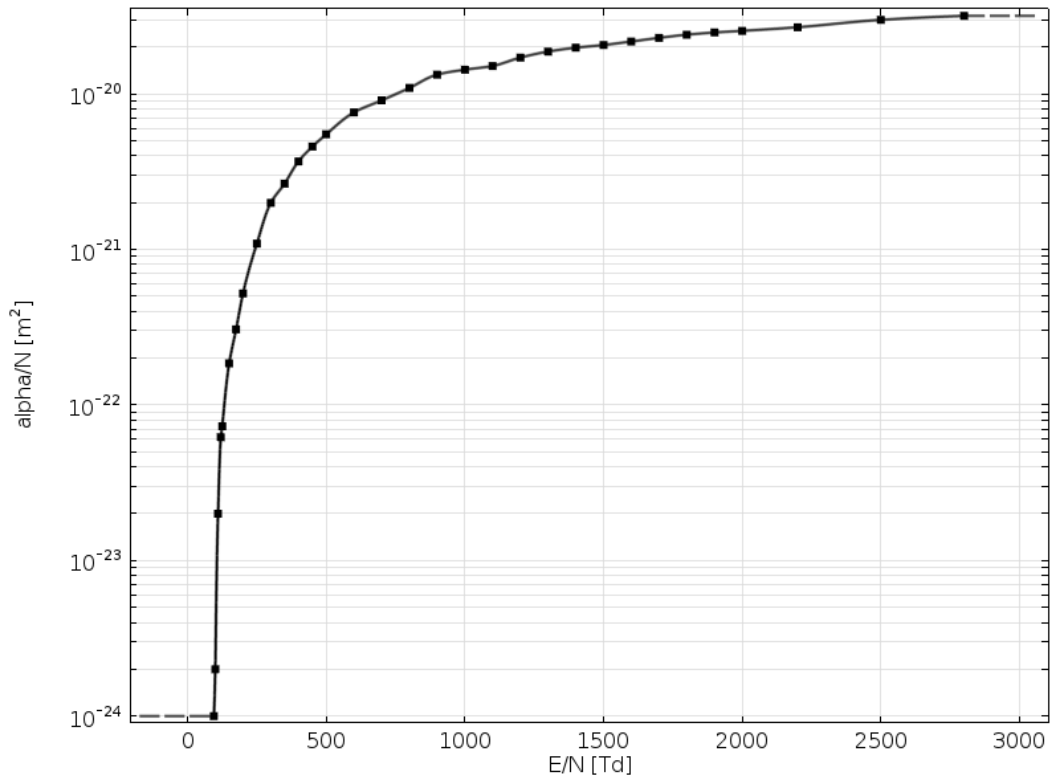


Figure 6. Plot of the tabulated values used for Townsend's first ionization coefficient α/N as a function of the reduced electric field E/N . Notice the logarithmic scale on the y-axis.

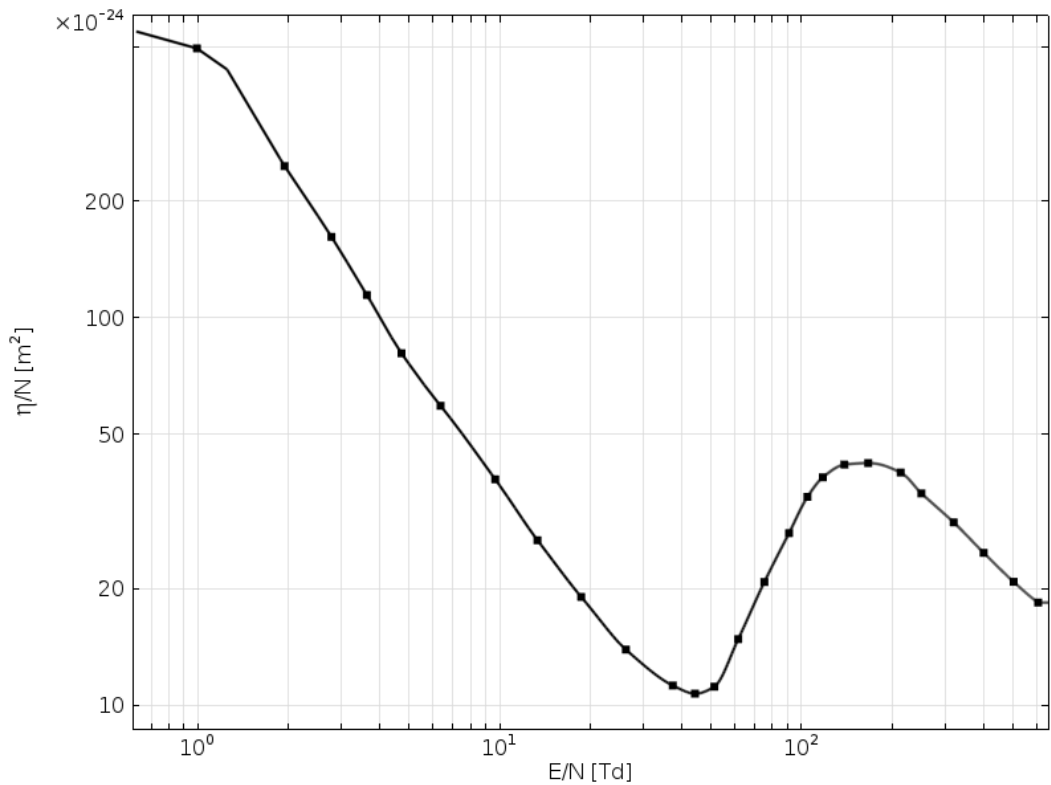


Figure 7. Plot of the tabulated values used for the reduced attachment coefficient η/N as a function of the reduced electric field E/N . Both x- and y-axis are on log scale.

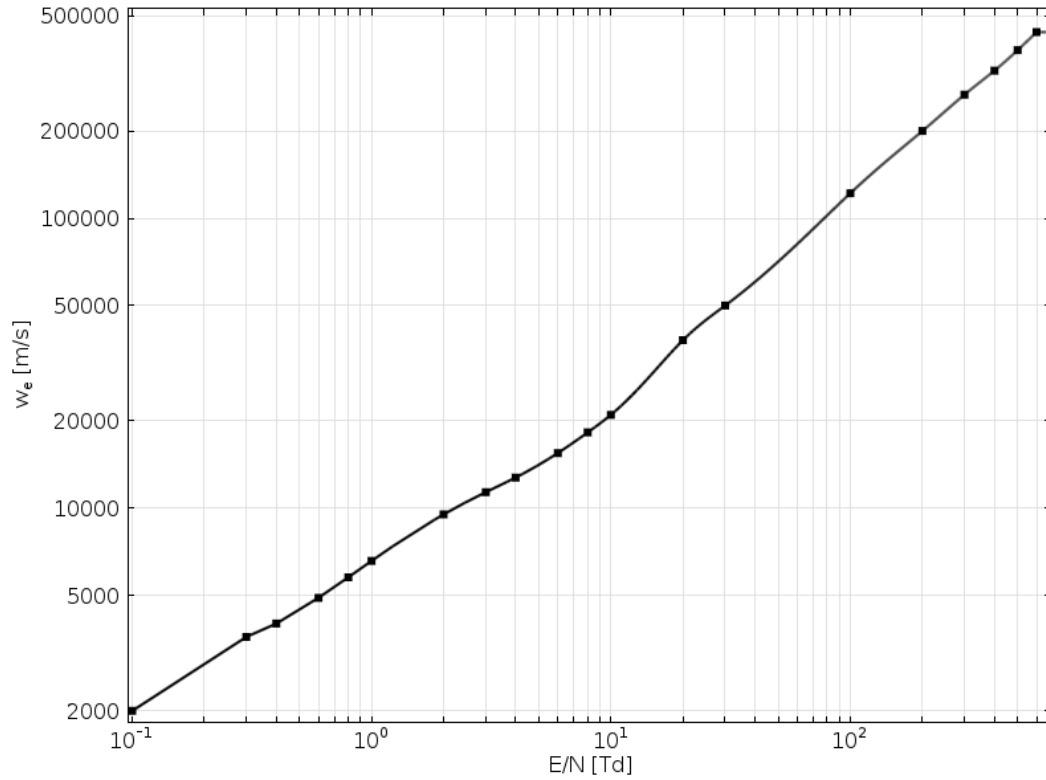


Figure 8. Plot of the tabulated values used for the reduced electron drift velocity w_e as a function of the reduced electric field E/N . Both x-axis and y-axis are on log scale.

This behavior is usually attributed to the dominating role of three body attachment processes in air. In the range of $40 < E/N < 150$ Td, the values of η/N increase due to an increase intensity of dissociative attachment and ion-molecule reactions [9] reaching the peak at 150 - 160 Td.

4.7. REDUCED ELECTRON DRIFT VELOCITY

As discussed in section 2.3 the rates for both ionization and attachment, R_{ion} and R_{att} respectively, are dependent of the electron flux (product of the drift velocity and density). Also, the rates depend on the ionization coefficient α and attachment coefficient η , respectively, that makes both to be highly non-linear. The dependence of electron drift velocity w_e on reduced electric field E/N is shown in Figure 8. As seen, the profile of w_e is rising linearly with an increase of field strength when plotted on a log scale. The tabulated values used in the model are taken from [9] and provided in Appendix 1.

4.8. DIFFUSION COEFFICIENTS

The diffusion coefficients for ions are calculated as shown in (20). To calculate diffusion for electrons, the electron characteristic energy D/μ is used, which is given as a function of the reduced electric field in Figure 9 (the tabulated values are provided in Appendix 1).

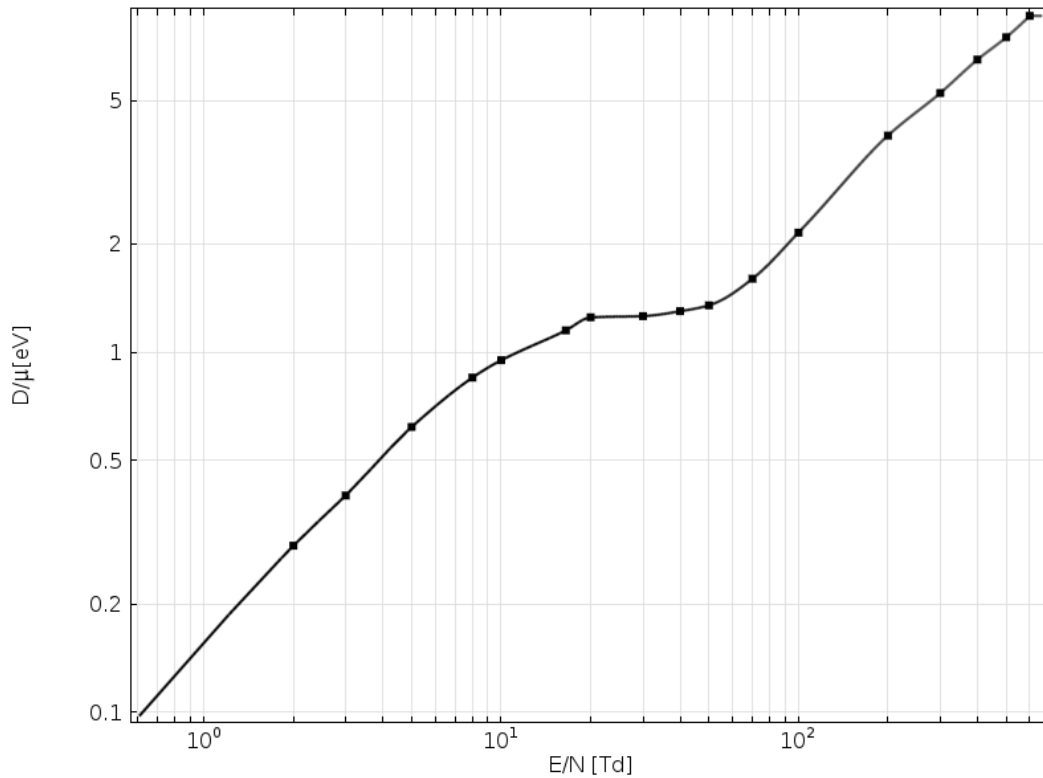


Figure 9. Plot of the tabulated values used for the characteristic electron energy D/μ as a function of the reduced electric field E/N . Notice that only the x-axis is log-scale.

4.9. APPLIED VOLTAGE SHAPE

As described in Chapter 3, the voltage applied to the wire in the coaxial geometry is a triangular voltage of varied magnitude and frequency. This is implemented in the model through a function *Waveform* under the node *Global Definitions*. For waveform-functions, a number of predefined shapes can be selected; saw tooth, sine, square or triangle. Here, the triangular shape is chosen. The setting for *Angular frequency* is given by the parameter w , explained further in section 4.10 below. Values for *Phase* and *Amplitude* are set as 0 and 1 respectively. Implementation carried out in this fashion renders a voltage wave with amplitude of 1 V. Later in the model, this value is to be scaled with a parameter u_amp to give it its correct amplitude. A plot of the voltage wave with amplitude 20 kV and frequency 1 Hz is seen in Figure 10 a).

As described in section 2.16, the displacement current component is dependent upon the derivative of the electric field. The electric field, on the other hand, is dependent of the applied voltage. The geometry of the triangular voltage wave imposes a problem at the peak points where the numerical derivative is not fully defined. To avoid computational errors at the time steps of the peaks, a smoothing needs to be introduced as in Figure 10b. In the software, the size of the transition zone can be defined for a particular frequency to get a correct capacitive current shape.

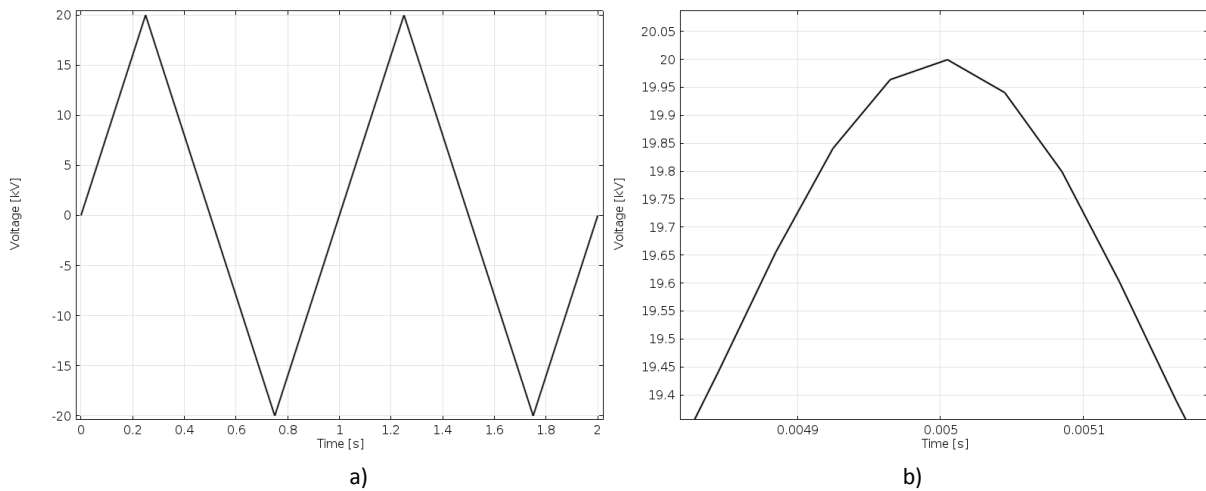


Figure 10. The a) triangular voltage wave applied to the anode wire and the b) smoothing applied to the peaks. Amplitude is set to 20 kV and frequency is set to 1Hz.

4.10. CONSTANT PARAMETERS

The sub-node *Parameters* is subordinated to the node *Global Definitions*. The parameters defined here are constant scalar values that valid throughout all levels of the model. Parameters can be either set by the software or inputted by user. The internally declared parameters used in this model are given in Table 2. Other parameters are user inputs. These are given in Table 3.

The geometric parameters $r0$, $r1$, $r2$ and $r3$ are used to define the computational area and the parameter h is the height of the cage or geometric area from the experiment. Further, eps_air and eps_pvc are used to give the material their characteristic properties, i.e. their relative permittivity as previously discussed in Chapter 3.

The initial ion concentration $n0$ and background ionization rate $R0$ are introduced as discussed in section 2.2. Mass of electrons, m_e , and mass of ions, m_p and m_n , are given through the inbuilt parameter for electron mass $m_e = me_const$, and the mass of the negative oxygen ion O_2^- . The mass of the O_2 molecule is then calculated as the mass of the negative ion with subtraction of the mass from the extra electron, and further the mass of the positive ion O_2^+ is calculated as the mass of the oxygen molecule minus the electron mass.

The mobility of ions is considered to be independent of the electric field and, hence, can be implemented as constant parameters. Values of mobility, mu_n and mu_p , differs between different authors and values used in this model is based on results given by [28].

Table 2. Parameters defined internally by software.

Description:	Parameter name:	Value:
Boltzmann's constant	k_B_const	$1.3806488 \cdot 10^{-23}$ J/K
Elementary charge	e_const	$1.602176565 \cdot 10^{-19}$ C
Mass of electron	m_e_const	$9.10938291 \cdot 10^{-31}$ kg
Permittivity of vacuum	$epsilon0_const$	$8.854187817 \cdot 10^{-12}$ F/m

Table 3. Constant parameters defined in the simulation model.

Description:	Name:	Expression:	Value:	Reference:
Boltzmann's constant	kb	k_B_const	$1.3806488 \cdot 10^{-23}$ J/K	
Elementary charge	q	e_const	$1.602176565 \cdot 10^{-19}$ C	
Permittivity of vacuum	$eps0$	$epsilon0_const$	$8.85418781 \cdot 10^{-12}$ F/m	
Point of wire surface	$r0$	0.00013	0.13 mm	
Point of barrier at wire side	$r1$	0.188	188 mm	
Point of barrier at cage side	$r2$	0.201	201 mm	
Point of cage surface	$r3$	0.5	500 mm	
Height of cage	h	2.5	2.5 m	
Relative permittivity of air	eps_air	1	1	
Relative permittivity of PVC	eps_pvc	3.5	3.5	
Background ionization rate	$R0$	$1.7e-7$	$1.7 \cdot 10^7$ 1/m ³ s	
Electron-ion recomb. rate	$beta_ei$	$5e-14$	$5 \cdot 10^{-14}$ m ³ /s	
Initial ion concentration	$n0$	$1e9$	$1 \cdot 10^9$ m ⁻³	[2][3]
Mass of electron	m_e	m_e_const	$9.10938291 \cdot 10^{-31}$ kg	
Mass of O ₂ ⁻ ion	m_n	$5.3e-26$	$5.3 \cdot 10^{-26}$ kg	
Mass of O ₂ ⁺ ion	m_p	$m_g - m_e$	$5.2998 \cdot 10^{-26}$ kg	
Mass of O ₂ molecule	m_g	$m_n - m_e$	$5.2999 \cdot 10^{-26}$ kg	
Mobility of negative ions	mu_n	$2.0e-4/delta$	$2.0 \cdot 10^{-4}$ m ² /Vs	[28]
Mobility of positive ions	mu_p	$2.7e-4/delta$	$2.7 \cdot 10^{-4}$ m ² /Vs	[28]
Secondary emission coefficient	$gamma$	$1e-3$	$1 \cdot 10^{-3}$	
Actual pressure	pg	101325	101 325 Pa	
Actual temperature	Tg	293	293 K	
Reference pressure	$p0$	101325	101 325 Pa	
Reference temperature	$T0$	293	293 K	
Relative air density	$delta$	$(T0*pg)/(Tg*p0)$	1	
Gas density	N	$pg/(kb*Tg)$	$2.5055 \cdot 10^{25}$ 1/m ³	
Tuning parameter	ad_p	0.3	0.3	
Voltage amplitude	u_amp	20e3	20 kV	
Voltage angular frequency	w	$2*pi*f$	$2\pi f$	
Voltage frequency	f	0.1 - 50	0.1 - 50 Hz	

Other authors, for example in [29], provide slightly lower values and therefore values for best fit will need to be evaluated. The secondary ionization coefficient γ , previously discussed in section 2.11, is implemented with the parameter name *gamma*.

The actual pressure and the actual temperature, p_g and T_g , are supposed to be given by the ambient conditions at the experiments discussed in Chapter 3. Since the experiment was conducted indoors in a large scale geometry, both the temperature and the pressure is assumed to be the same as the reference conditions p_0 and T_0 .

The tuning parameter ad_p is linked to the isotropic diffusion option previously described in 4.3 and is initially given a value of 0.3.

4.11. VARIABLE PARAMETERS

Under *Global Definitions*, a sub-node called *Variables* is created. All the expressions defined in this sub-node are global, i.e. they can be called anywhere in the model whether it be physical components or in geometric entities. Variables can also be defined as local, and will then only be available and valid for the special entity where they are defined. It is possible to create several groups of variables, even at global level, which can come in handy if many variables are to be defined. By separating them in groups it might be faster and easier to find and handle the variable of interest.

For a variable to become available for post processing a solution must first be computed, i.e. the variables will not become available only by stating them in the list. A variable is inputted into the model by stating a variable name, the variable expression and an optional description. If the parameters and values used to declare the variable expression will render a valid unit, this unit will automatically be shown by the software. The variables that are implemented into the model are seen in Table 4.

The diffusion coefficient for electrons is calculated as the characteristic electron energy multiplied with the mobility of electrons. The diffusion coefficients for the positive and negative ions are instead calculated according to (20). The space charge density is very straight forward and is implemented as described in (43). The source terms are implemented in the same straight forward way as described in (23), (24) and (25).

To calculate the detachment rate used in the source terms, the detachment coefficient k_{det} is calculated according to (33). The detachment coefficient is then multiplied with the gas density N to

Table 4. Variable parameters defined in the simulation model.

Description:	Name:	Expression:	Unit:
Diffusion coeff. electrons	D_e	$D\mu_e(EN_{td})*\mu_e$	m^2A
Diffusion coeff. pos. ions	D_p	μ_p*kb*T_p/q	m^2/s
Diffusion coeff. neg. ions	D_n	μ_n*kb*T_n/q	m^2/s
Space charge density	ρ	$q*(mod1.pos-mod1.neg-mod1.e)$	C/m^3
Source term electrons	$source_e$	$Rion + R0 + Rdet - Rrec_{ei} - Ratt$	
Source term positive ions	$source_p$	$Rion + R0 - Rrec_{ei} - Rrec_{ii}$	
Source term negative ions	$source_n$	$Ratt - Rdet - Rrec_{ii}$	
Detachment coefficient	k_{det}	$2.5e-19*exp(-6030/T_n)$	
Detachment frequency	nu_{det}	$k_{det}*N$	
Detachment rate	$Rdet$	$(nu_{det}*mod1.neg)*(mod1.neg>0)$	
Ion-ion recomb. coeff.	$beta_{ii}$	$1.5e-12*sqrt((300/T_p)*(300/T_p)*(300/T_p))$	
Ion-ion recomb. rate	$Rrec_{ii}$	$(beta_{ii}*mod1.pos*mod1.neg)*((mod1.neg>0)\&\&(mod1.pos>0))$	$1/m^3s$
Ion-electron recomb. rate	$Rrec_{ei}$	$(beta_{ei}*mod1.e*mod1.pos)*((mod1.e>0)\&\&(mod1.pos>0))$	$1/m^3s$
Reduced electric field	EN_{td}	$abs(mod1.es.Er)/N*1e21$	Vm^2
First ionization coeff.	α	$\alpha N(EN_{td})*N$	$1/m$
Attachment coefficient	η	$\eta N(EN_{td})*N$	$1/m$
Attachment rate	$Ratt$	$(\eta*mod1.e*W_e(EN_{td}))*(mod1.e>0)$	$1/m^3s$
Ionization rate	$Rion$	$(\alpha*mod1.e*W_e(EN_{td}))*(mod1.e>0)$	$1/m^3s$
Electron mobility	μ_e	$(W_e(EN_{td})/abs(mod1.es.Er))*(abs(mod1.es.Er)>0)$	m^2/V s
Neg. ion temp.	T_n	$tg+(m_n+m_g)*((\mu_n*abs(mod1.es.Er))^2)/kb/3$	K
Pos. ion temp.	T_p	$tg+(m_p+m_g)*((\mu_p*abs(mod1.es.Er))^2)/kb/3$	K

give the detachment frequency nu_{det} which is finally multiplied with the internal variable for concentration of negative ions to give the detachment rate as in (12). Note that the detachment rate is only valid as long as the concentration of negative ions is positive.

The ion-ion recombination coefficient is calculated as described in (37), while the ion-electron recombination coefficient $beta_{ie}$ is described in 4.10. The ion-ion recombination rate and the ion-electron recombination rate are calculated as (14) and (15) respectively. Notice that both recombination rates have conditions. The concentrations of the ionic species and the electrons need to be positive values for the recombination rates to be valid.

The other two source term components, the ionization rate and the attachment rate, are calculated as (12) and (13) respectively using the reduced ionization coefficient described in section 4.5, the reduced attachment coefficient described in 4.6 and the reduced electron drift velocity described in 4.7. Temperature for both positive and negative ions is calculated as described in (26).

4.12. BOUNDARY FLUXES AND CALCULATION OF SURFACE CHARGE

To control the ionic and electron fluxes at the boundaries is of utmost importance. The electric field strength controls the direction of the fluxes and the direction must change according to the direction of the field. If the fluxes over the boundaries are not configured in a correct way, this might lead to charged species accumulating at the wrong time instance and thus affecting the local field in a non-physical way.

To be able to compute the accumulated surface charge at the included PVC-barrier, it is also important to implement correct fluxes. The fluxes need to assure that the space charge leave the air domains, and instead is treated as surface charge as mentioned in section 4.4. If the charged species would not leave the domain as they should, they might instead be treated as both surface charge and space charge in the same point and therefore render a charge accumulation that is too high as compared with reality. One flux is defined for each species at each boundary or point. At the wire point, if the electric field strength is greater than zero, the flux of electrons and negative ions are assumed to be positive convective flux. This might seem strange, as the Flux-node is defined as inward and a positive wire voltage should attract electrons and negative ions and transport them out of the domain. Although, the variables are implemented as positive and the sign that ensures an outflow is taken care of by an internal vector direction. At positive field strength the flux of positive ions at the wire is assumed to be zero.

When the field strength reverts polarity, e.g. in the negative voltage cycle, there is a convective outflow of positive ions at the wire, while the flux of negative ions is zero. At the same time, Townsend's secondary ionization coefficient comes in to play as positive ions impact with the wire, and hence there is a flux of electrons into the discharge domain controlled by the gamma-coefficient.

The cage side fluxes function in a similar way. If the field strength at the cage is greater than zero, positive ions will be transported out of the domain and the flux of negative ions and electrons will be zero. This might seem contradictive to the above reasoning, but one must remember that when the field strength is positive and the cage side an even greater positive field is present at the wire side, thus repelling positive ions towards the cage. Even though positive ions will impact the cage in the same manner as they will on the wire, the energy they will produce upon impact is assumed to be too small to let Townsend's secondary ionization have any effect.

Table 5. List of variables used to calculate the corona discharge current.

Description:	Variable name:	Expression:	Unit:
Total capacitance	Ccyl	$((1/C1)+(1/C2)+(1/C3))^{-1}$	F
Capacitance domain 1	C1	$2*\pi*h*\epsilon_0*\epsilon_{air}/\log(r1/r0)$	F
Capacitance domain 2	C2	$2*\pi*h*\epsilon_0*\epsilon_{pvc}/\log(r2/r1)$	F
Capacitance domain 3	C3	$2*\pi*h*\epsilon_0*\epsilon_{air}/\log(r3/r2)$	F
Displacement current density	J_cap	$-\epsilon_0*d(Vr,t)$	A/m ²
Displacement current at wire	I_cap_wire	$2*\pi*r0*h*J_{cap}$	A
Displacement current at cage	I_cap_cage	$2*\pi*r3*h*J_{cap}$	A
Capacitive current component	I_cap_0	$Ccyl*d(wave,t)$	A
Ionic current density at cage	J_ion_cage	$-q*(pflux_{cage}-nflux_{cage}-e_{flux_{cage}})$	A/m ²
Ionic current density at wire	J_ion_wire	$q*(pflux_{cage}-nflux_{cage}-e_{flux_{cage}})$	A/m ²
Ionic current at cage	I_ion_cage	$2*\pi*r3*h*J_{ion_cage}$	A
Ionic current at wire	I_ion_wire	$2*\pi*r0*h*J_{ion_wire}$	A
Total current at cage	I_tot_cage	$I_{ion_cage}+I_{cap_cage}$	A
Total corrected current at cage	I_tot_cage_corr	$I_{tot_cage}-I_{cap_0}$	A

When the field strength at the cage side turns negative, the field strength at the wire side will have an even greater negative value and thus there will be a convective flux of negative ions and electrons out of the domain. At the same time, the flux of positive ions is assumed to be zero.

As described in the chapters Transport of Diluted Species and Boundary ODE's and DAE's, charged species that reaches the PVC-barrier in the discharge domain is assumed to take the form of surface charge on the barrier. To allow this, the *Outflow*-nodes are used as in 4.3. At the same time, the ODE's from 4.4 needs an input or a source term, and this input is calculated through the two variables j_{bar_w} and j_{bar_c} . These variables calculates the convective flux for each species and scales in with the elementary charge which gives the current density and is then integrated over time and used as input for the surface charge-nodes described in the Electrostatics chapter. This is only valid in the case were a PVC-barrier is introduced in the discharge domain.

4.13. CURRENT CALCULATIONS

Since the current is measured at the cage or ground electrode in the experiment, the same option is implemented into the simulation model. Current calculations are done according to the theory explained in section 2.16. Implementations of calculations are done locally in the model. Under the model-node, a sub-node Definitions is available. For easy access to current calculations, a sub-node for variables called Currents is created. Variables for current calculations are implemented according to Table 5.. Following (50), the total current at the cage is calculated as an ionic current component

summed with the displacement current component. Furthermore, the displacement current also consists of two components; one part due to the geometrical capacitance and one part due to the space charge influence. Since effects due to the ionic movement are of greater interest in this study, the geometric component is subtracted from the total current. The total current and the capacitive element are calculated as (50) and (53) respectively.

The ionic current at the cage is calculated in accordance with (51); a geometric variable A multiplied with the current density. The current density at the cage is in its turn calculated as the flux of positive ions at the cage minus the fluxes of negative ions and electrons scaled by the elementary charge q . Fluxes are calculated as described in 4.12. A negative sign is introduced to make correction for the current direction.

The displacement current component is calculated with a geometrical variable A multiplied with current density according to (52), and the displacement current density is calculated by using the parameter ϵ_0 multiplied with $d(V_r, t)$, the time derivative of internal variable V_r (which is the potential gradient in the r-direction, i.e. the electric field strength).

The geometrical capacitive current component is calculated according to (53), where a constant capacitive value is multiplied with the time derivative of the applied voltage. The constant C_{cyl} calculates the capacitance of the geometry, in accordance with (54). However, since the discharge geometry is made up of media with different permittivities, the total capacitance is calculated as three capacitances in series, according to

$$C_{cyl} = \left(\frac{1}{C_1} + \frac{1}{C_2} + \frac{1}{C_3} \right)^{-1} \quad (60)$$

where C_1, C_2 and C_3 are capacity of the three domains respectively. C_1, C_2 and C_3 are in their turn calculated as

$$\begin{aligned} C_1 &= \epsilon \frac{2\pi h}{\ln(r_0/r_1)} \\ C_2 &= \epsilon \frac{2\pi h}{\ln(r_1/r_2)} \\ C_3 &= \epsilon \frac{2\pi h}{\ln(r_2/r_3)} \end{aligned} \quad (61)$$

where C_1 is the capacitance from the wire point to inner barrier point, C_2 is the capacitance of the barrier, and C_3 is the capacitance from the outer barrier point to the cage. The time derivative of the

voltage is calculated as the derivative of the voltage wave described in 4.9. From the above described variables the corrected cage current is now calculated.

As seen in Table 5., the current at the corona wire is also calculated. This current is not used to present the total discharge current, but only for purposes of evaluation. It is calculated analog to the current at the cage side, only with parameters changed to be valid for the wire side instead.

4.14. MESHING OF THE MODEL

Although applying a mesh that is refined in the right areas can be crucial, the meshing of this model turns out to not be of any greater significance as long as enough elements are used. Since the geometry is 1D, meshing elements naturally is only applied along the line.

The size of the mesh is predefined as extremely fine and is calibrated for plasma studies (options provided by the software). A *Distribution*-mesh is applied to all domains with 750 elements per domain with an element ratio of 500. This gives a total of 2250 elements with an element length ratio of 86.96 μm for the models where the PVC-barrier is introduced. For the models without the PVC-barrier, these settings simply mean that 750 elements will be distributed for the whole discharge domain with an element length ratio of 2 mm. Using these settings render perfect element quality for both cases.

Since most of the events of greater interest occur at the boundaries, it is important to have a greater mesh resolution at these areas. Therefore, the *Distribution method* is set to *Geometric sequence* and *symmetric* which results in a denser mesh close to the wire point, the barrier points, and the cage point.

Applying a mesh with a higher number of elements might eventuate in a slightly finer resolution in the result graphs, but at the same time increases the time lapse for simulations. Since additional elements in the middle of the domains are not necessary and the element ratio setting attend to high resolution in the points of interest an increase of elements is not needed.

4.15. STUDY SETTINGS

To render a solution for the simulation, the *Study*-node is used. This node is where the settings for the solver are defined and from where a simulation can be executed. It is of outermost importance to determine correct study settings for a low frequency time dependent problem. If the time steps taken are too big, there might be a lack of resolution which will result in loss of accuracy. Too small time steps will instead render huge computational time and demand a great computational power.

Naturally, all implemented physics will be solved with time dependency. The time range and time step of the solution will differ depending on the studied frequency. The sub-node *Time-Dependent Solver* is where most settings are defined. For the settings of *Absolute Tolerance*, the option *Scaled* is chosen for *Global Method* with a tolerance of 0.001. This controls the error in each of the integration steps. The option *Update scaled absolute tolerance* is selected, which means that the step is accepted if the equation

$$\left(\frac{1}{M} \sum_j \frac{1}{N_j} \sum_i \left(\frac{|E_i Y_i|}{A_{s,i} + R|Y_i|} \right)^2 \right)^{1/2} < 1 \quad (62)$$

is valid. Here M is the number of fields, N_j is the degrees of freedom in the field j , E_i is the local error estimate of the solution vector during the performed time step, $A_{s,i}$ is the scaled absolute tolerance for the number of degrees of freedom i , R is the relative tolerance, and Y_i is the scaled solution vector.

As *Time Stepping Method*, backward differentiation formulas (BDF) are used with different order of accuracy. BDF is known for being stable but might introduce a certain damping in the solution, more common for lower-order methods. The damping might introduce smoothness where sharp gradients are expected, which is especially true for high frequencies. This is not expected to have any influence in regard to the problems solved in this thesis as only low frequencies are of interest.

For solving the multiphysics problem, *Fully Coupled* node was chosen which attributes for a damped invariant version of Newton's method that is valid for time dependent problems and solves nonlinear systems. The *Nonlinear method* chosen is *Automatic (Newton)*. The problem can then be described as

$$f(U) = 0 \quad (63)$$

where $f(U)$ is the residual vector, and U is the solution vector. From an initial guess U_0 , a linearized model with U_0 as the linearization point solves the discretized linearized model

$$f(U_0)\delta U = -f(U_0) \quad (64)$$

where δU is the Newton step. Solving the linearized problem is done by the selected linear solver, in this case the *Direct-solver* described above. The solution vector is updated in an iterative way according to

$$U_1 = U_0 + \lambda \delta U \quad (65)$$

where λ ($0 \leq \lambda \leq 1$) is the damping factor. The solver then estimates the error E for the iteration by solving

$$f(U_0)E = -f(U_1). \tag{66}$$

If the error E is larger for the current iteration than for the previous, the damping factor λ is reduced and a new value for U_1 is recalculated. The reduction of λ and the recalculation of U_1 will proceed until the error E is less than for the previous iteration or until λ will fall below the *Minimum damping factor* value.

When a step is successful the solver will continue with the next Newton iteration. Termination of the Newton iterations eventuates when the estimated relative error is smaller than the specified value. For every solution, a maximum number of iterations are specified, and Newton's method will be terminated even if the set tolerance is not accomplished.

CHAPTER

5

SIMULATIONS AND RESULTS

The complexity of modeling a corona discharge implicates that certain simplifications has to be accepted in the mathematical model. The corona discharge incorporates up to a hundred different physical processes (e.g. plasma chemical reactions) and describing and accounting for all those processes in a single model will not only be hard to realize, but will also demand a lot of computational power. Certain processes are more accentuated and are therefore chosen as the processes of interest and are included in the mathematical model. To analyze if including these processes is enough to acquire correct results which will correspond to reality is not always an easy task. A lot of parameters are included in the mathematical equations, and sometimes small modifications or deviations of these parameters will have a great impact on the simulated results. Therefore, the included processes might be enough but wrongly configured. Even though parameters and processes are well studied and defined in literature, most values are empirical and cannot be derived through mathematics. In this thesis some base values are chosen, as described in Chapter 4, and need to be verified through simulations and by comparison of the results with experimental values. In the cases where these parameters does not provide good fit, the values might be altered within limits defined by typical deviations between various data sets presented in literature to make sure that simulated results are as conform to the experimental results as possible.

Since simulations at higher frequencies without an inclusion of a PVC-barrier implicate a more simple physical description, the simulations are at first carried out with such properties to analyze the parameter values selected and to validate values for a best fit. Thereafter, the frequency is lowered and once again simulations are performed without including the PVC-barrier to apprehend if the parameter values still hold true. Last, the PVC-barrier is introduced into the model, the necessary equations to govern the newly introduced physical processes are implemented and analysis of the results determines if the same parameter values still renders a good fit or if further alteration of parameters are necessary. In some cases this will imply that certain parameters might obtain non-

physical values or values that do not have support from literature. However, the aim is to derive a simulation model that provides results as closer to the experimental data as possible.

5.1. SIMULATIONS WITHOUT PVC-BARRIER

To be able to verify the functionality of the model and the input parameters, the simulations are first performed without including the PVC-barrier in the discharge domain. By leaving out the barrier the ionic transport is more straightforward as the ions and electrons can move freely. Therefore, evaluation of the literature parameters is easier to assess. According to [1], modifications of the parameters given from the literature presented in Chapter 4 do not provide the best fit possible. By modifying the parameters according to Table 7, a better fit can be achieved for 50 Hz.

From Figure 11 it can be seen that the discharge current will give different results depending what cycle is studied. In the first cycle the onset voltage is high at 15.6 kV while at the second cycle it is much lower at around 4.5 kV, to finally reach a steady state onset at 5.4 kV in the third cycle. After the third cycle a steady state condition is reached, meaning that for subsequent cycles the voltage-current characteristics will obtain the same appearance. For the case of 1 Hz voltage frequency, it is found that it only takes two cycles for the voltage-current characteristics to obtain steady state and for a frequency of 0.1 Hz steady state is obtained already from the first cycle.

The obtained differences in the onset voltages can be explained by the fact that charges have more time to move into the domain at lower frequencies. In the 50 Hz case, charges only move a short distance before the voltage reverses and hence it takes one cycles before the domain hold enough charge to affect the onset voltage and two or more cycles for the charges to have accumulated enough amount to reach a steady state. In the 0.1 Hz case the situation is reversed. Since the time period is long enough for the charges to move across the gap even before the first onset of the corona there will be no differences between the first and the successive voltage cycles.

Table 6. Modified values for parameters to provide a best fit [1]

Parameter:	Value in literature:	Modified value:	Unit:
Mobility of positive ions μ_p	$2.0 \cdot 10^{-4}$	$1.5 \cdot 10^{-4}$	m^2/Vs
Mobility of negative ions μ_n	$2.7 \cdot 10^{-4}$	$1.7 \cdot 10^{-4}$	m^2/Vs
Secondary ionization coefficient γ	$1 \cdot 10^{-3}$	$2 \cdot 10^{-5}$	-
Detachment rate coefficient k_{det}	$2 \cdot 10^{-16} \cdot \exp(-6030/T_n)$	$2.5 \cdot 10^{-19} \cdot \exp(-6030/T_n)$	m^3/s
Ion-ion recombination rate β_{ii}	$2 \cdot 10^{-12} (300/T_i)^{1.5}$	$1.5 \cdot 10^{-12} (300/T_i)^{1.5}$	m^3/s

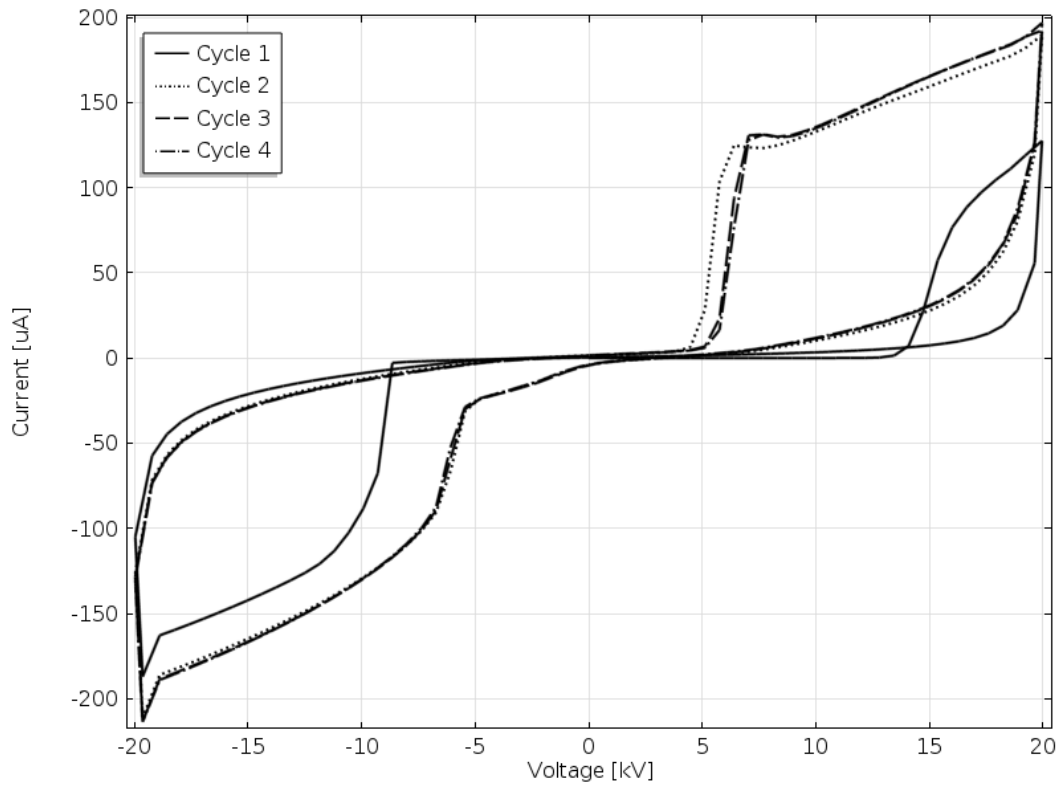


Figure 11. The discharge current for the first four voltage cycles for the 50 Hz case. At cycle 4 a steady state value is reached.

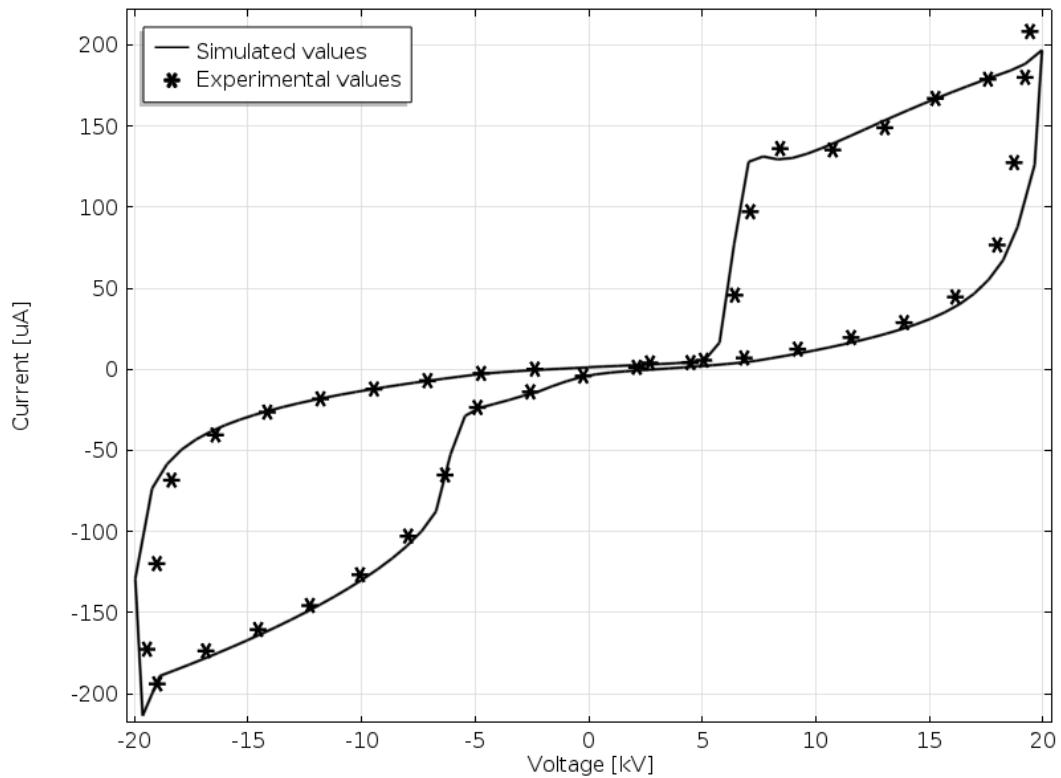


Figure 12. Comparison between 50 Hz 20 kV simulated values and experimental values.

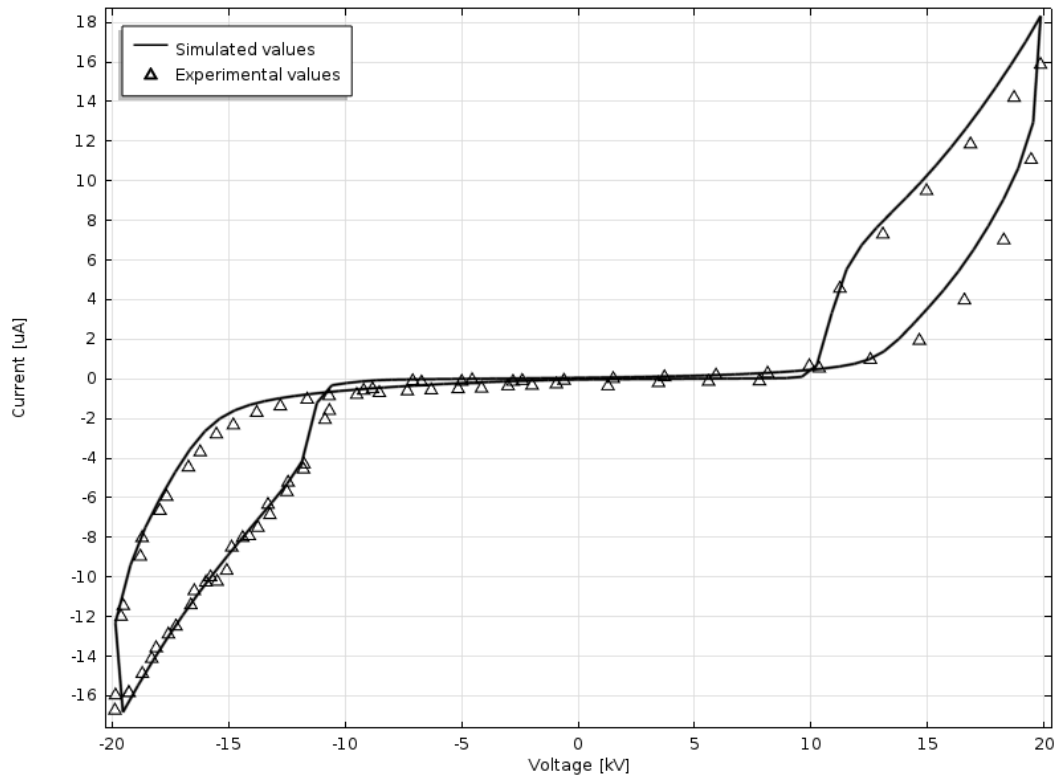


Figure 13. Comparison between 1 Hz 20 kV simulated values and experimental values.

The discharge current is calculated according to (50) and, as seen in Figure 12, the parameter values described above render a good fit when compared to the experimental values. The onset of the corona appears at the same voltage level for both positive and negative corona and the peak current also shows a good match.

With the same parameter settings, but the frequency of the voltage reduced to 1 Hz, the fit is still good for the negative corona cycle but a certain discrepancy occurs in the positive corona cycle, as seen in Figure 13. The current magnitude is still on point, but the rise time of the simulated values is steeper and the extinction of the discharge is more rapid.

The same reasoning holds true for when voltage frequency is reduced further down to 0.1 Hz, as seen in Figure 14. The values for the negative corona cycle are very much on point, although the onset voltage is slightly lower for the experimental values. For the positive corona cycle, the discrepancy is similar to the 1 Hz case but reversed; the onset voltage is slightly higher and the rise and decay time is faster for the experimental values. Here, it is also notable that the peak current for positive semi-cycle is almost 1 μA less than that for the simulated values. It should be noted that Figure 12 only shows the result for the fourth cycle while Figure 13 shows the second cycle and Figure 14 shows the first cycle, i.e. the steady state cycle.

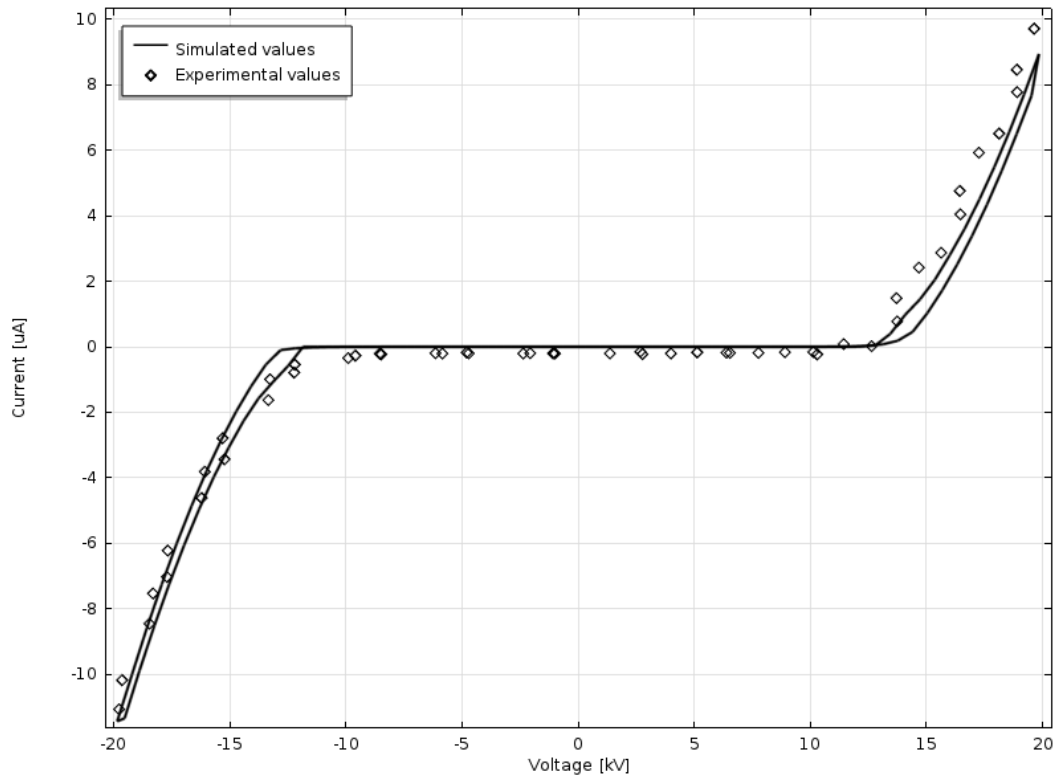


Figure 14. Comparison between 0.1 Hz 20 kV simulated values and experimental values.

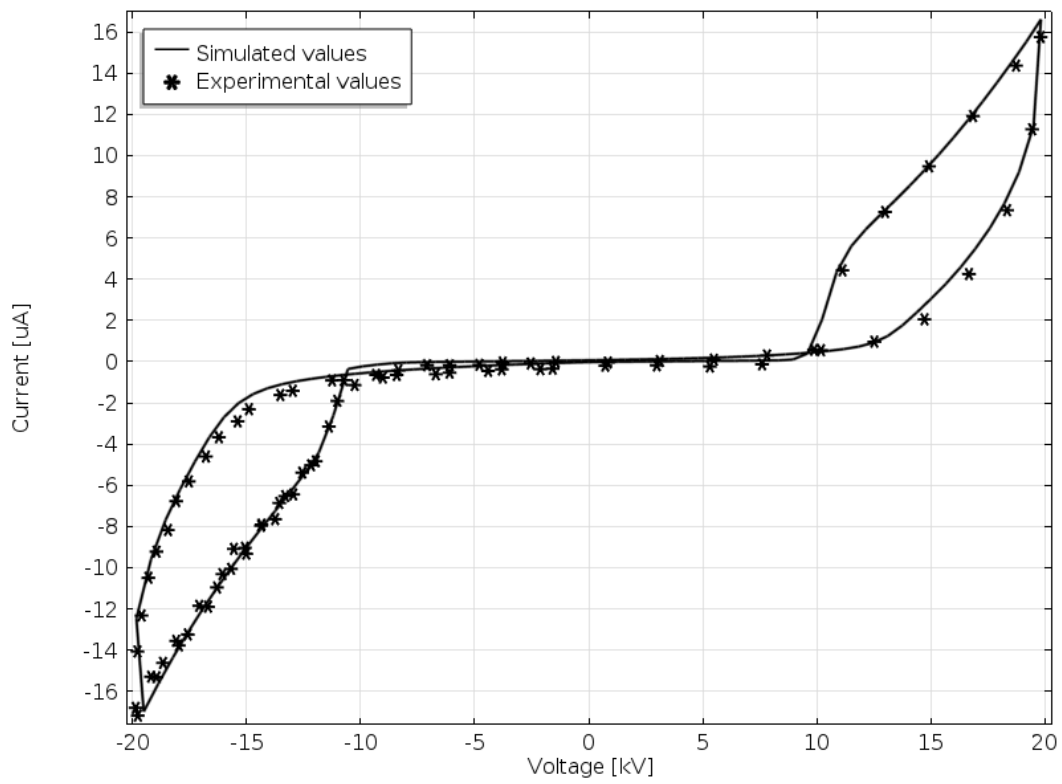


Figure 15. Comparison between the simulation of 20 kV with a frequency of 1 Hz and the experimental result with same settings. Mobility of ions has been reduced further compared to Figure 13.

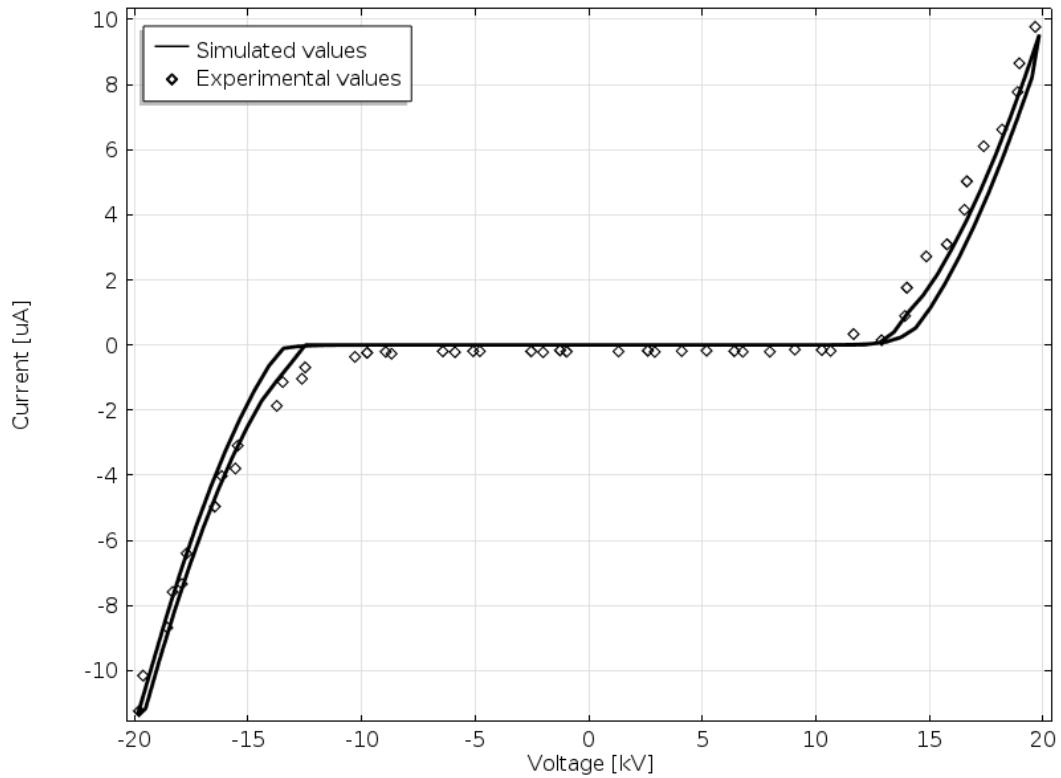


Figure 16. Comparison between the simulation of 20 kV with a frequency of 0.1 Hz and the experimental result. Mobility of ions has been increased and secondary ionization coefficient has been decreased compared to Figure 14

The agreements between the data for 1 Hz and 0.1 Hz cases can be improved by slight modifications of the parameters values. Thus, by reducing the mobility of positive and negative ions slightly below the values shown in Table 6, results in very good fit between experimental and simulated currents as seen in Figure 15.

However, for the 0.1 Hz case, a slight increase in the mobility for positive and negative ions together with a reduction of the secondary ionization coefficient provides the best fit to the experimental values as seen in Figure 16. As seen in the figure, the peak current of the positive corona cycle is now much closer to the experimental values, even if there is still a small discrepancy in onset voltages.

Although further adjustments of the simulation parameters are possible to ensure even more accurate results, the results presented here are deemed to be good enough. Since detailed information regarding pressure and humidity variations from the experiment is lacking (these might affect the ion mobilities), it is close to impossible to fully recreate the same settings and, therefore, the deviations of the simulated results can be considered as acceptable.

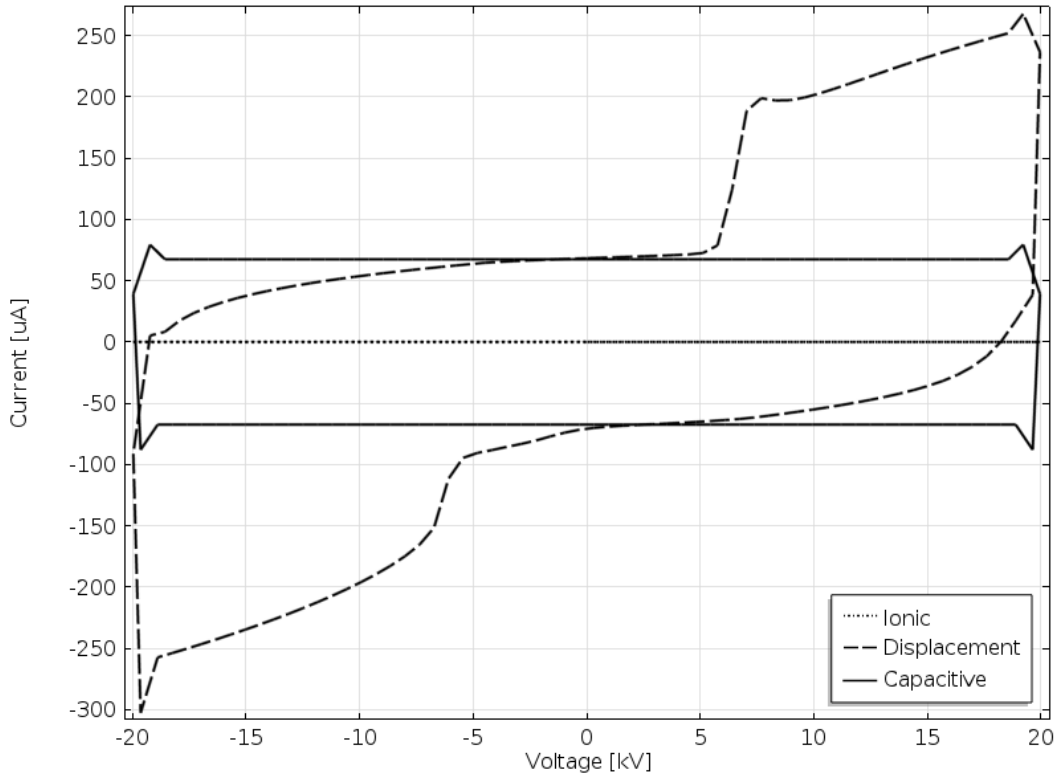


Figure 17. The ionic, displacement and capacitive current components at 50 Hz frequency and 20 kV voltage magnitude.

5.2. CORONA CURRENT COMPONENTS

In Figures 17, 18 and 19 the current components described in section 2.16 are plotted for 50 Hz, 1 Hz and 0.1 Hz respectively. It is notable that for the higher frequency 50 Hz (Figure 17), the ionic or conductive current component is practically zero at the measuring point. This means that none of the charge carriers has reached all the way over the gap to flow into the external circuit. At lower frequency (1 Hz, Figure 18), the ionic component is no longer zero, but instead reaches a magnitude of almost half the total magnitude, $I_{ion} = 8.8 \mu\text{A}$ and $I_{disp} = 18.2 \mu\text{A}$, respectively. For an even lower frequency (0.1 Hz, Figure 19) this effect is enhanced even further and the ionic component constitutes the major part of the total current with $I_{ion} = 9 \mu\text{A}$ and $I_{disp} = 2 \mu\text{A}$. The reason for the increased ionic current at lower frequency is that the time frame for the charge carriers to flow through the domain is increased before the polarity reversal and the charges start to move in the opposite direction. The capacitive current component, that is defined according to (53) as the product of the time derivative of the electric field and the capacitance of the coaxial cylindrical system, should in theory yield a constant value since the derivative of the triangular voltage is constant. However, the shape of this current is affected by the quality (e.g. stability) of the test voltage supply in experiments and smoothness of the function used for representing the applied voltage in the simulations. Therefore, it is hard to expect a good match for this current component.

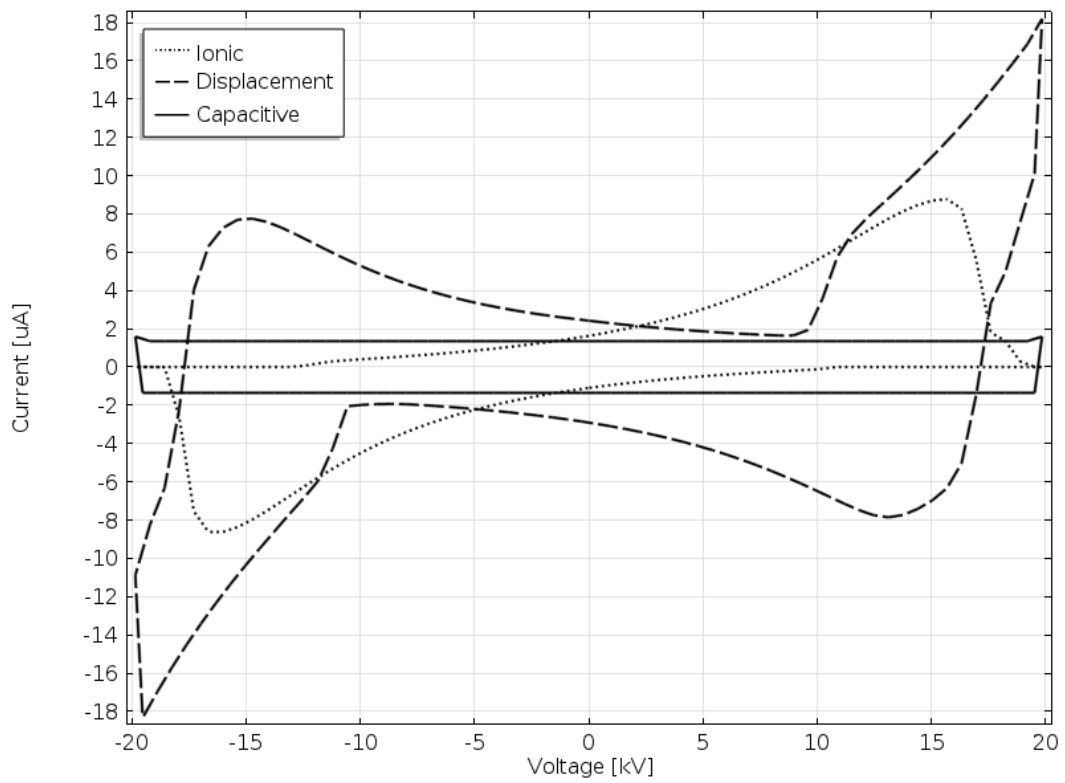


Figure 18. The ionic, displacement and capacitive current components at 1 Hz frequency and 20 kV voltage magnitude.

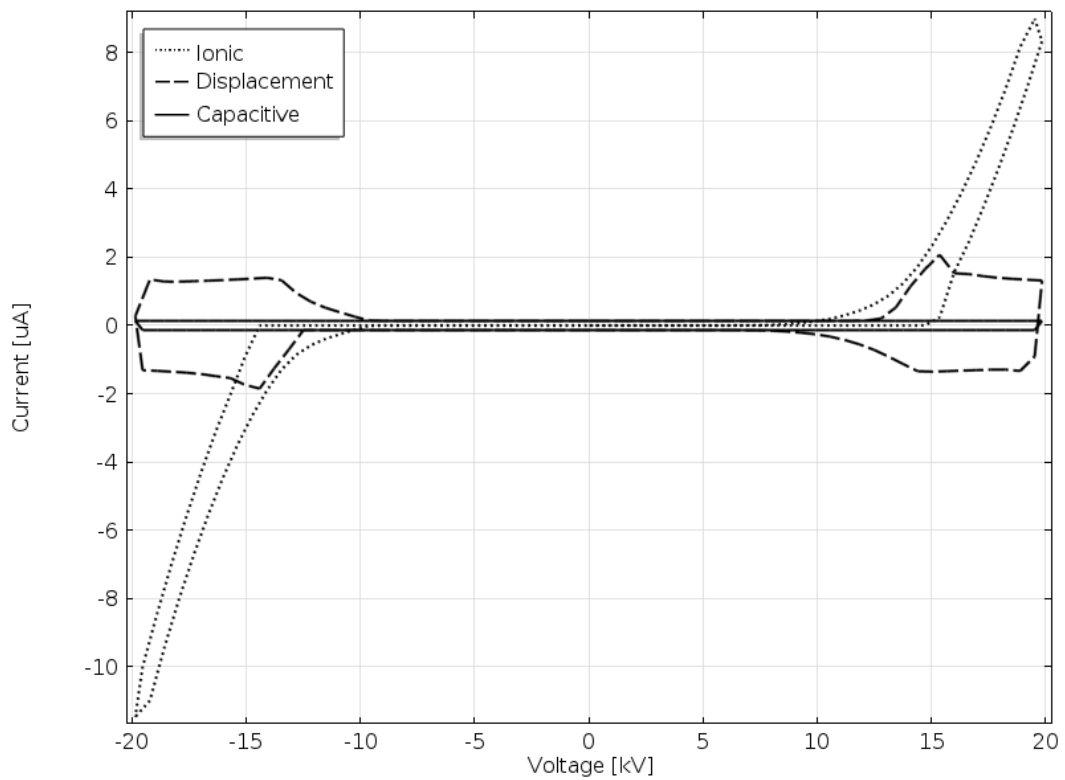


Figure 19. The ionic, displacement and capacitive current components at 0.1 Hz frequency and 20 kV voltage magnitude.

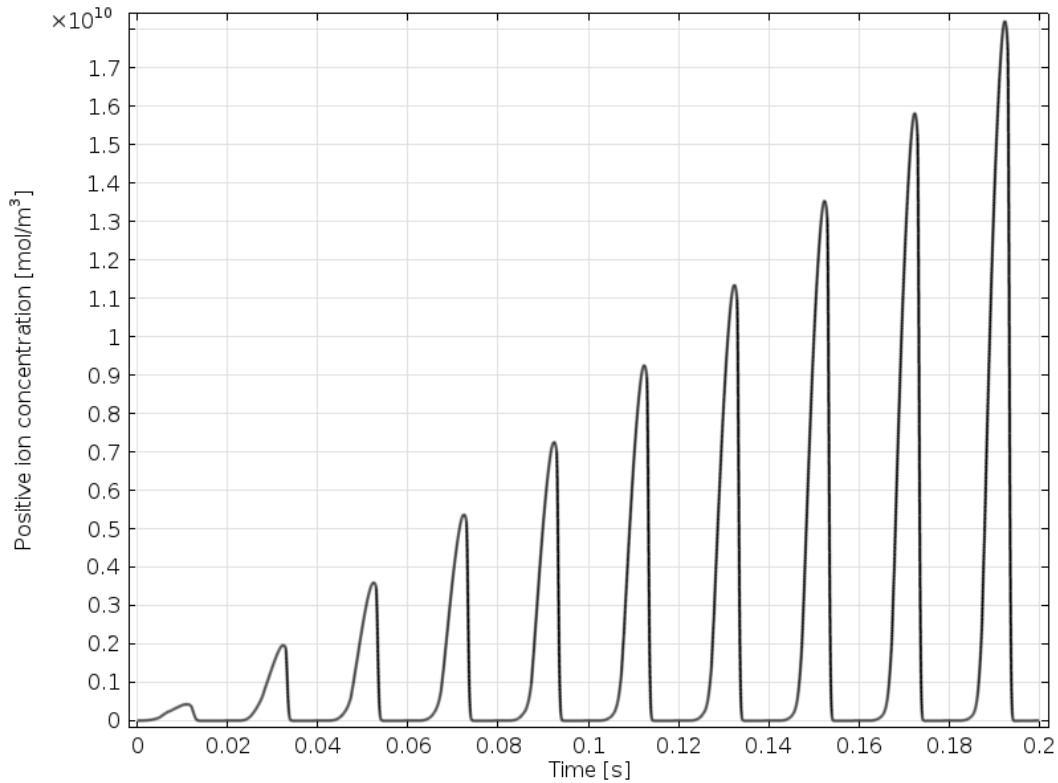


Figure 20. Concentration of positive ions accumulated at the cage for the 50 Hz case for the first 10 cycles. No steady state is reached, as the concentration increases for each cycle.

This same issue also seems to affect the boundary transitions of the displacement current component. Since the same phenomenon is observed even in the experimental values it is concluded that a smoothing function has been applied in the experiment as well. This “disturbance” is more accentuated at 50 Hz frequency and has less impact at 1 Hz and 0.1 Hz respectively.

5.3. SPACE CHARGE ACCUMULATION IN GAS

As previously shown, it takes one, two or three cycles respectively for the 0.1 Hz – 50 Hz cases to have the discharge current to reach a steady state. Next step is to evaluate if charges accumulated at the cage side will also reach steady state. To do this, simulation of 10 cycles has been run for each frequency; 50 Hz, 1 Hz and 0.1 Hz.

To run a simulation for 10 cycles and provide time steps small enough to ensure a good resolution requires huge computational power and extremely long computational time, especially in the 50 Hz case. The results of such long calculations are presented in Figure 20 and Figure 21. As it can be seen, no steady state for concentrations of charge carriers is obtained. The maximum density of electrons

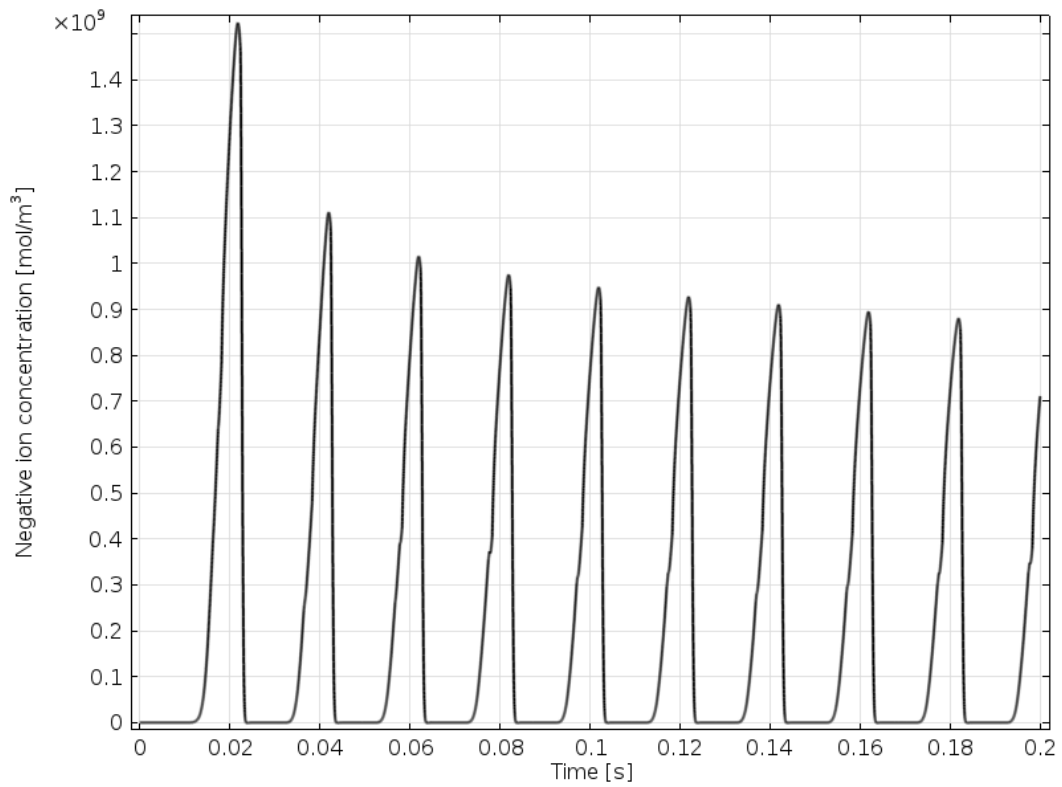


Figure 21. Concentration of negative ions at the cage side for the first 10 cycles in the 50 Hz case.

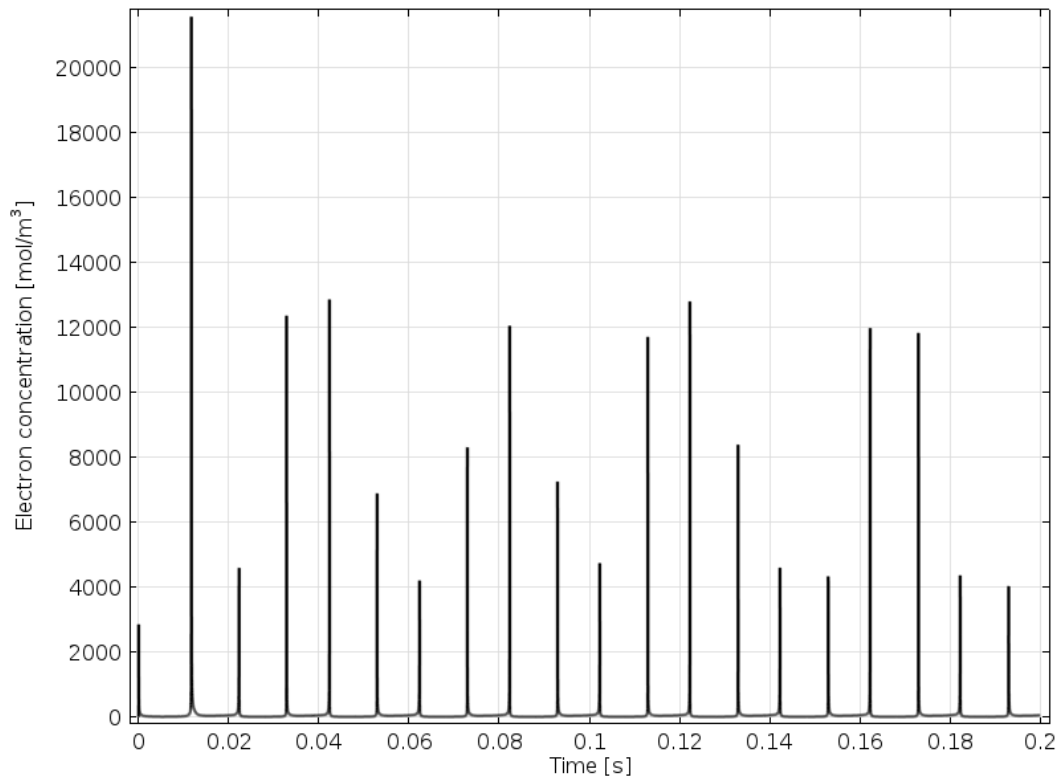


Figure 22. Concentration of electrons at the cage side for the 50 Hz case. The figure shows variations for 10 cycles.

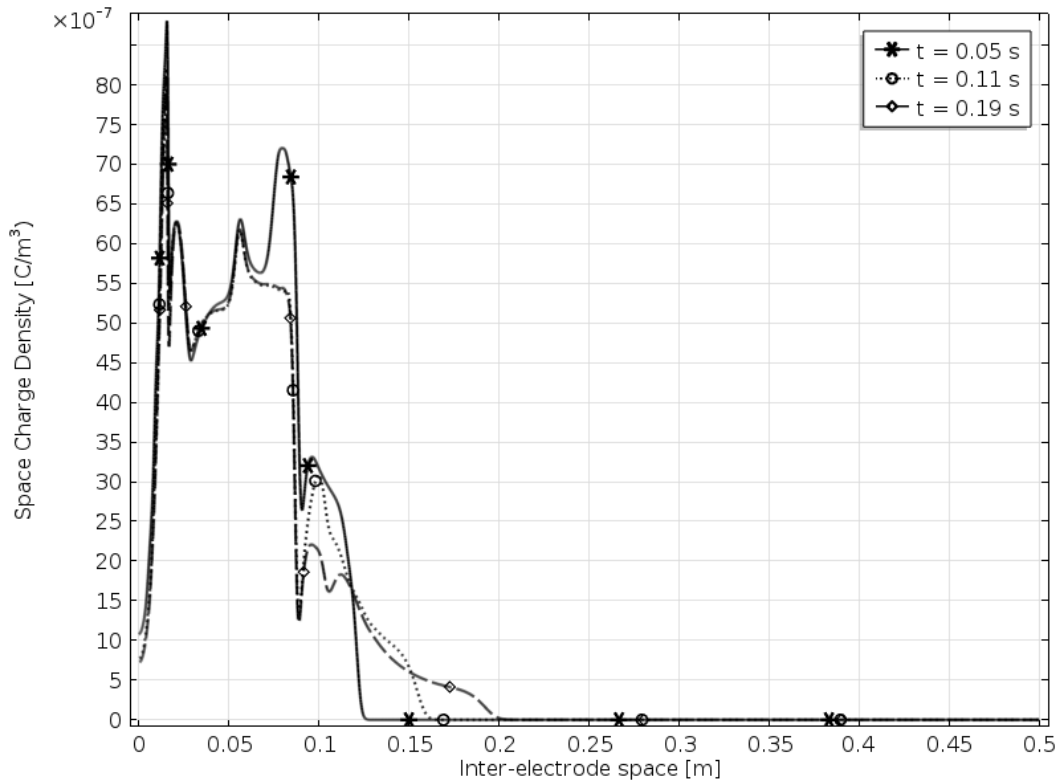


Figure 23. The space charge density in the inter-electrode space at three different instants in time for the 50 Hz case. The space charge does not traverse the gap, but only reaches about 0.2 m into the inter-electrode space.

changes with time (Figure 22) while the positive ions keep accumulating at higher concentrations for each cycle (Figure 20). These variations are associated with decreasing concentrations of the negative ions (Figure 21). One may guess that reaching a steady state for charge carriers densities would require additional voltage cycles to be simulated.

By analyzing the presented plots, one may notice that the peaks of electron concentration at the cage occur at the times when positive and negative ion concentrations are at their lowest. The lack of ions amount to a low rate of ion-electron recombination and hence free electrons are allowed to exist for a longer period of time. The fact that a steady state is not reached is explained by the high frequency and the short time for charged species to traverse the discharge domain before the voltage polarity is reversed. Thus, it can be seen in Figure 23 that the space charge density expands into the inter-electrode space with time, but a substantial space charge density appears in a layer ~ 0.2 m at the corona wire. No further expansion of the space charges is observed.

In contrast, the situation is different in 1 Hz case. Even after the first cycle, steady state values are reached for the densities of charged species, see Figure 24. This can be explained by long time frame enough for the charged species to traverse the inter-electrode space during the positive half cycle.

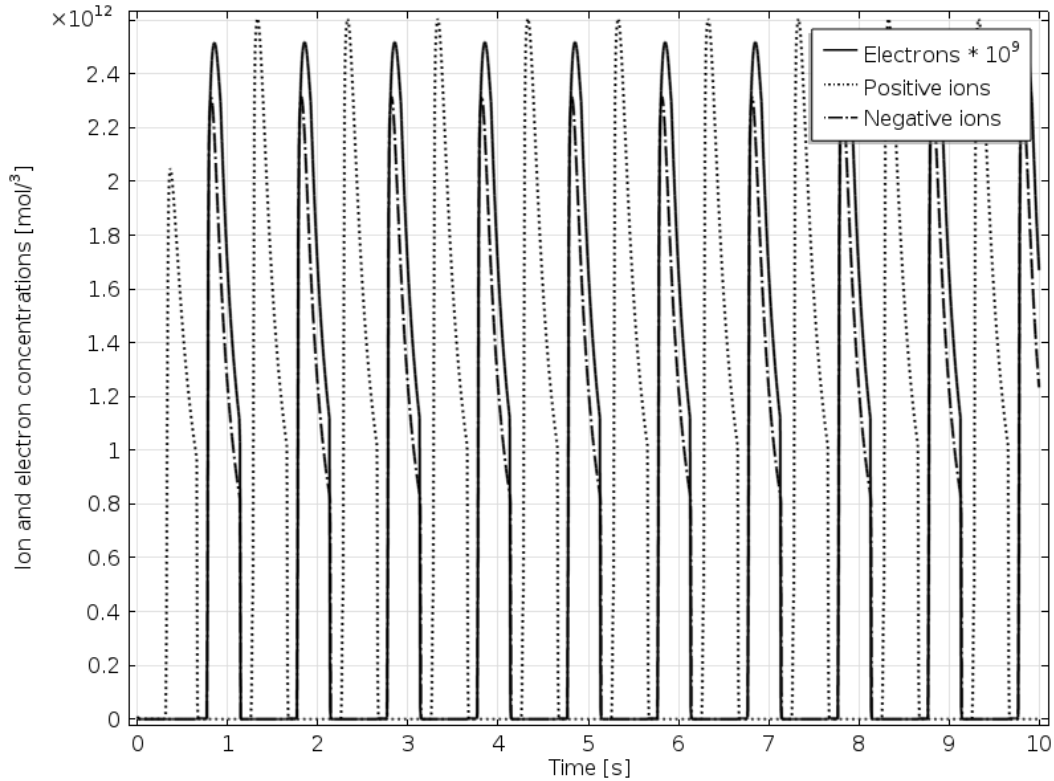


Figure 24. Concentration of electrons and positive and negative ions at the cage. The figure shows the first 10 cycles for the 1 Hz case. Notice that the electron concentration is magnified 10^9 times to be seen in the same plot.

The time variations of electrons and positive and negative ions during each cycle are similar to those during previous cycles.

The dynamics of the processes leading to the profiles in Figure 24 can be seen as follows. Since the simulations started from positive semi-cycle of the triangular voltage wave, the positive ions created in corona region are repelled from the wire and move towards the cage. The number of positive ions accumulating at the cage during the first cycle is smallest compared to other cycles. At steady state which is reached after the second cycle, the density is about $2.6 \cdot 10^{12} \text{ m}^{-3}$. The negative ions accumulate during the negative cycle; reaching almost the same value at $2.5 \cdot 10^{12} \text{ m}^{-3}$. Free electrons accumulate at the cage only during the negative cycle and at very low numbers reaching a maximum concentration at 250 m^{-3} .

The fact that the charged species have enough time to traverse the whole inter-electrode space even in the first cycle is more visible in Figure 25. One can observe that the space charge density at the cage side is significantly increased even after the first positive half cycle (for the frequency is 1 Hz, the first positive half cycle extends to 0.5 s).

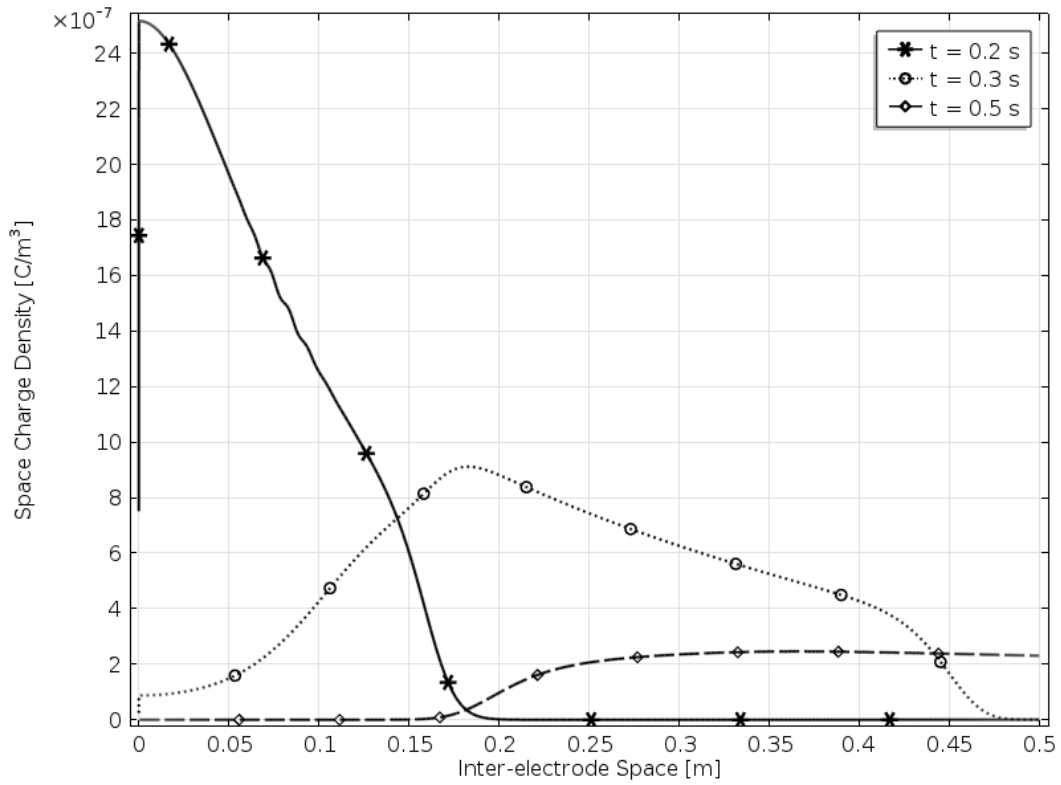


Figure 25. Space charge density levels in the inter-electrode gap at three different instants in time for the 1 Hz case. The space charge traverses the gap even within the first cycle.

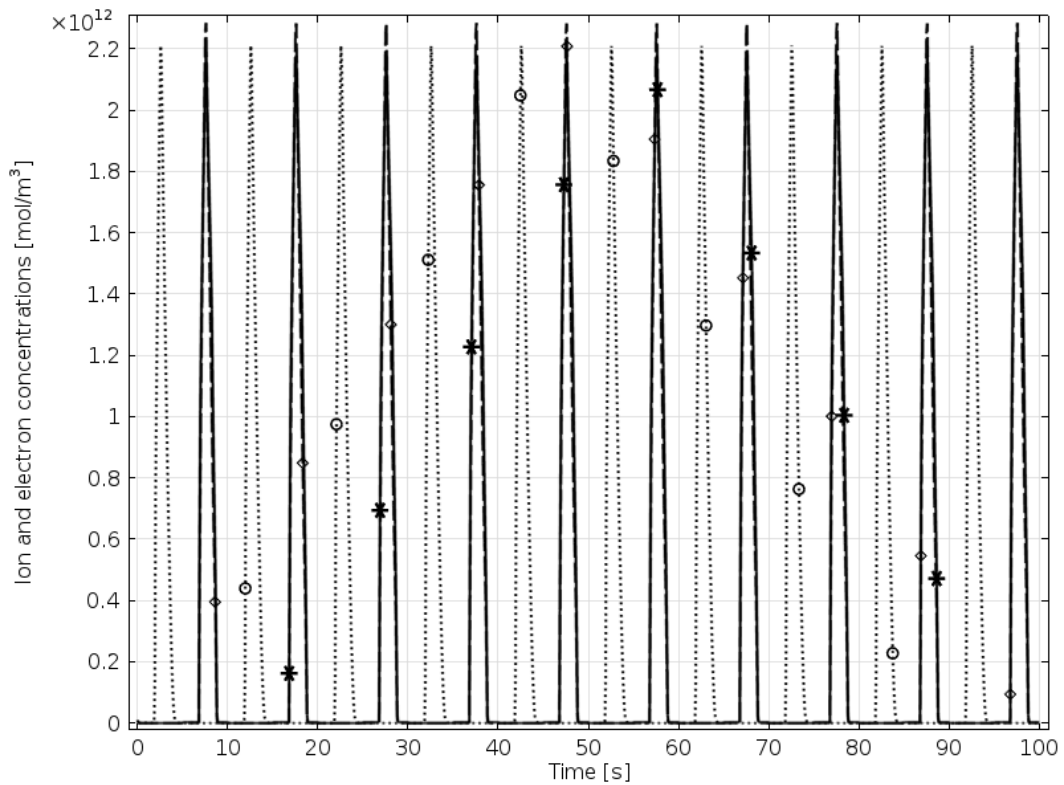


Figure 26. Concentration of electrons and positive and negative ions at the cage for the first 10 cycles in the 0.1 Hz case. The electron concentration increases with the concentration of negative ions and might be hard to see in the figure.

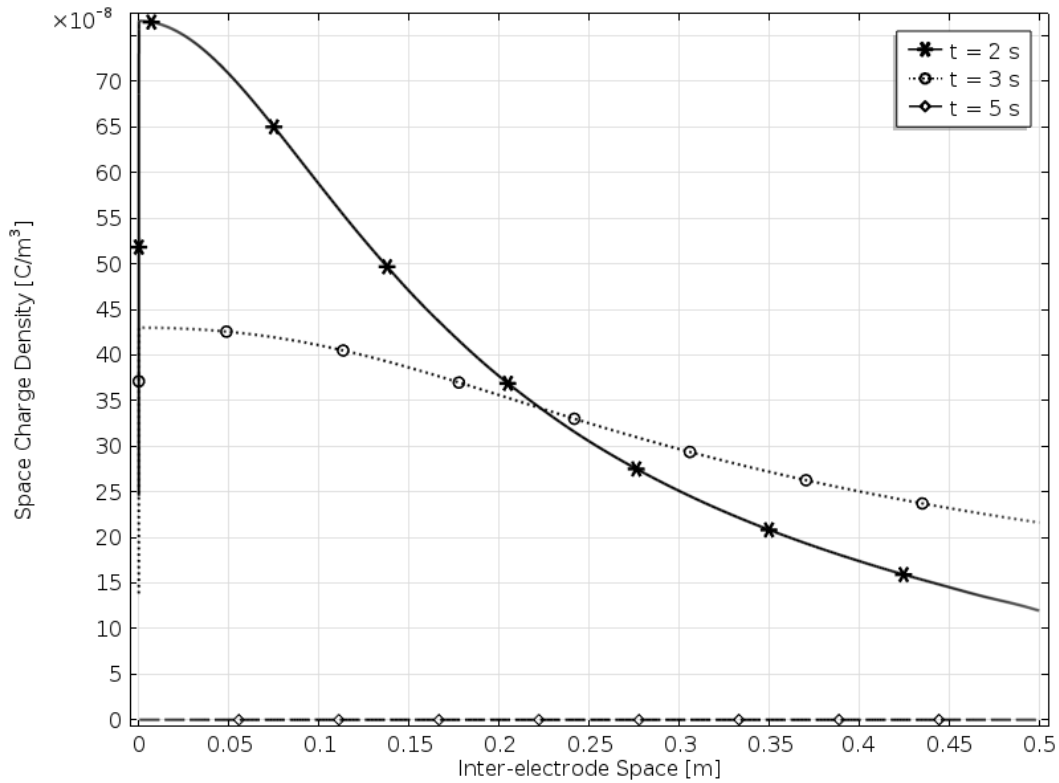


Figure 27. Space charge density in the inter-electrode space for the 0.1 Hz case. The space charge distributes in the gap very rapidly.

After 0.2 s, the space charges have travelled almost as far into the discharge domain as it does over all cycles in total compared to the 50 Hz case (Figure 23). After 0.3 s, the charges have almost reached the cage and at 0.5 s they start accumulating at the cage boundary.

As expected, the 0.1 Hz case is similar to the 1 Hz case, as seen in Figure 26. The difference is that the density of accumulated positive ions at the cage side reaches a steady state value even in the first cycle at $2.2 \cdot 10^{12} \text{ m}^{-3}$. The concentration of negative ions accumulating during the negative half cycle reaches a maximum of $2.3 \cdot 10^{12} \text{ m}^{-3}$, i.e. the accumulation of negative ions is slightly more intensive compared to the 1 Hz case where accumulation of positive ions were slight higher. The explanation to this is probably the altering of the ion mobility and the gamma coefficient previously performed to obtain a discharge current fit matching experimental values as close as possible. The electron accumulation once again occurs in the negative half cycle and yields a low number at 218 m^{-3} .

As seen in Figure 27, the space charge distributes in the discharge volume rapidly. Already during the first cycle of positive voltage the charges have reached the barrier and start to accumulate.

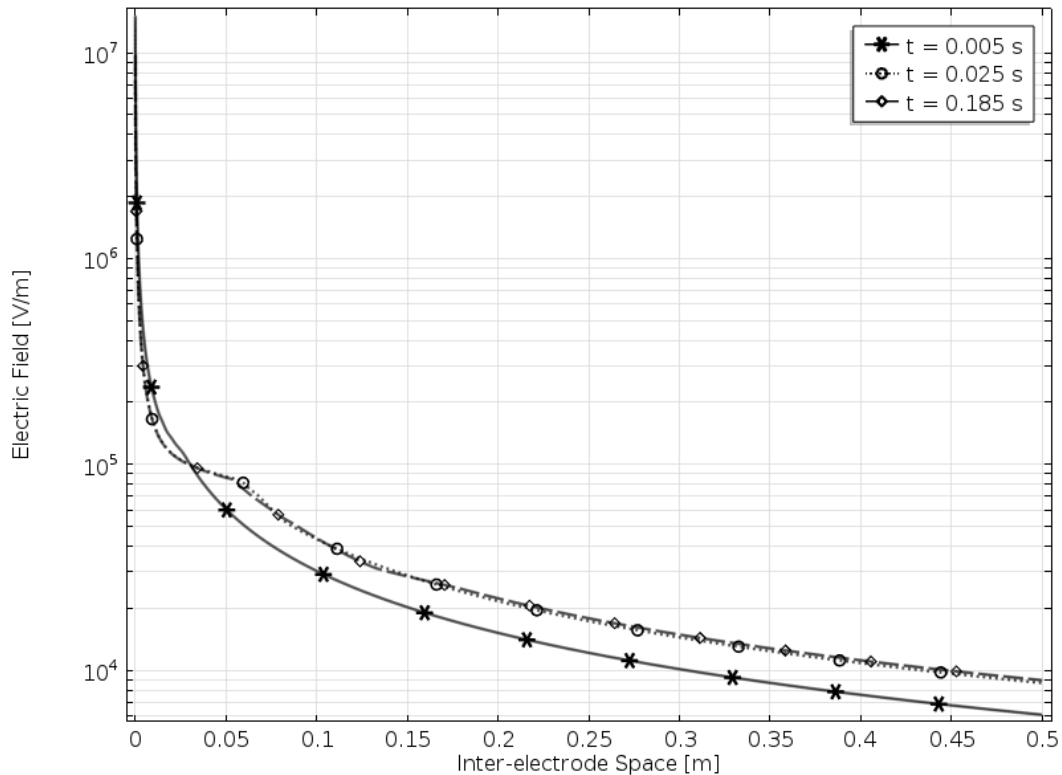


Figure 28. Electric field distribution in the inter-electrode space at peak voltage for the 50 Hz case. Notice the logarithmic scale on the y-axis to better enhance the difference in field strength. The field is enhanced more in the vicinity of the wire, as the space charge tends to not drift further into the gap.

5.4. EFFECT OF SPACE CHARGE ON ELECTRIC FIELD DISTRIBUTION

The space charge movement in the inter-electrode space has a clear impact on the electric field magnitude and distribution. This is most obvious for the 50 Hz case. The time instants discussed below are all from when a positive voltage is applied at the wire side. Figure 28 shows the distribution of the electric field at peak voltage for three time instants. As seen in the figure, at the first voltage peak reached at $t = 0.005$ s the space charge has little impact, while at the next voltage peak occurring at $t = 0.025$ s the field is distorted. Notice the similarities to the theory explained in section 2.14. As the space charge moves further into the gas volume, the field further away from the wire is impacted. Even though the impact is not huge, a logarithmic scale is used to visualize it, it is still pronounced. As explained above, even after 10 cycles the charges have not moved any greater distance into the inter-electrode space, and hence the field distortion occurs at more or less the same point even at the last voltage peak at $t = 0.185$ s. For the 1 Hz case, the space charge distributes in the whole discharge area at a much faster rate and, hence, the difference in field distortion between the first voltage peak at $t = 0.25$ s and the second voltage peak at $t = 1.25$ s only shows a difference in the region closest to the cage side. This is seen in Figure 29.

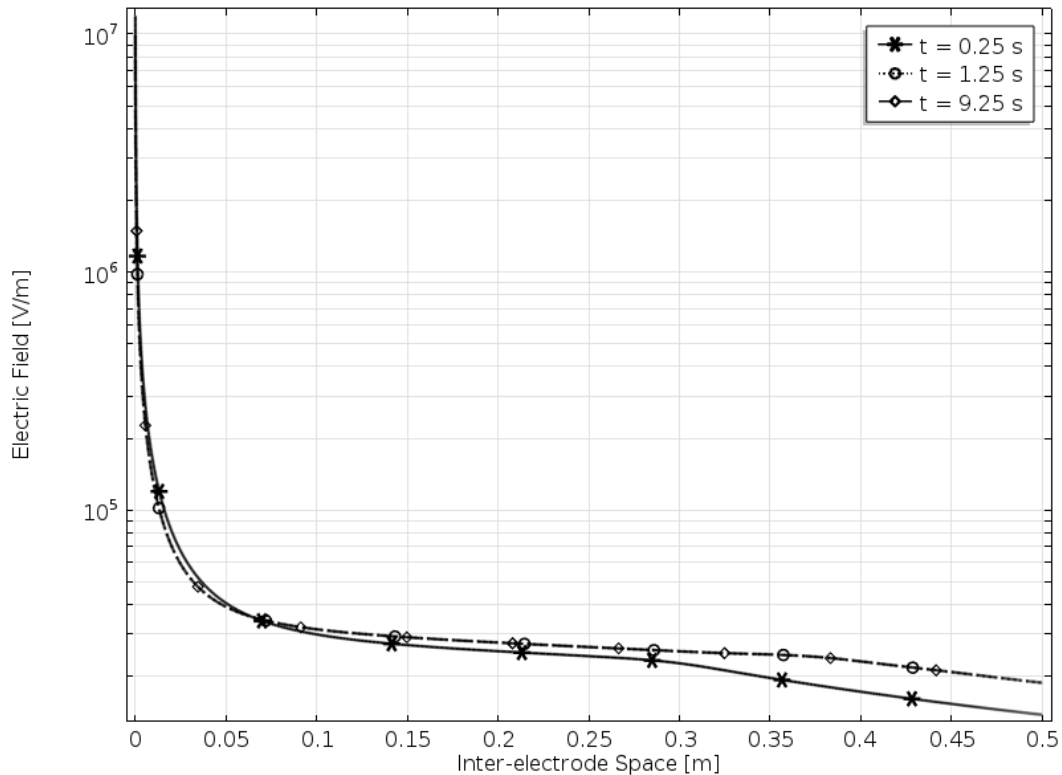


Figure 29. The electric field distribution in the inter-electrode space for the 1 Hz case at peak voltage. Notice the logarithmic scale on the y-axis to enhance the difference in field strength. As the space charge has traversed the gap, the field is enhanced closer to the cage side.

At even lower frequency, the space charges have time to spread through the discharge area during the first cycle, and hence there is no difference in how the field is affected at the different voltage peaks. The 0.1 Hz case is seen in Figure 30.

A noticeable difference is how the space charge distribution affects the electric field strength closer to the cage side depending on the frequency. For 50 Hz voltage frequency the field strength at steady state reaches 8850 V/m. When the 1 Hz voltage is utilized, the field strength reaches a value of 18 800 V/m at steady state, while for 0.1 Hz the field strength is 20 140 V/m. Since the voltage is positive at the time instants studied this holds true to theory as the field strength should increase when positive charges are repelled from the wire into the discharge domain.

5.5. SIMULATIONS WITH PVC-BARRIER

As can be seen from the analysis above, the simulations yielded results which agreed well with experimental data for the case of pure air. Thus, the next step is to include the PVC-barrier into the model. As previously described, the barrier acts as an obstacle for the fluxes of charged species, i.e. no charge carriers (electrons or ions) are allowed to pass through it and the current in the barrier is solely capacitive.

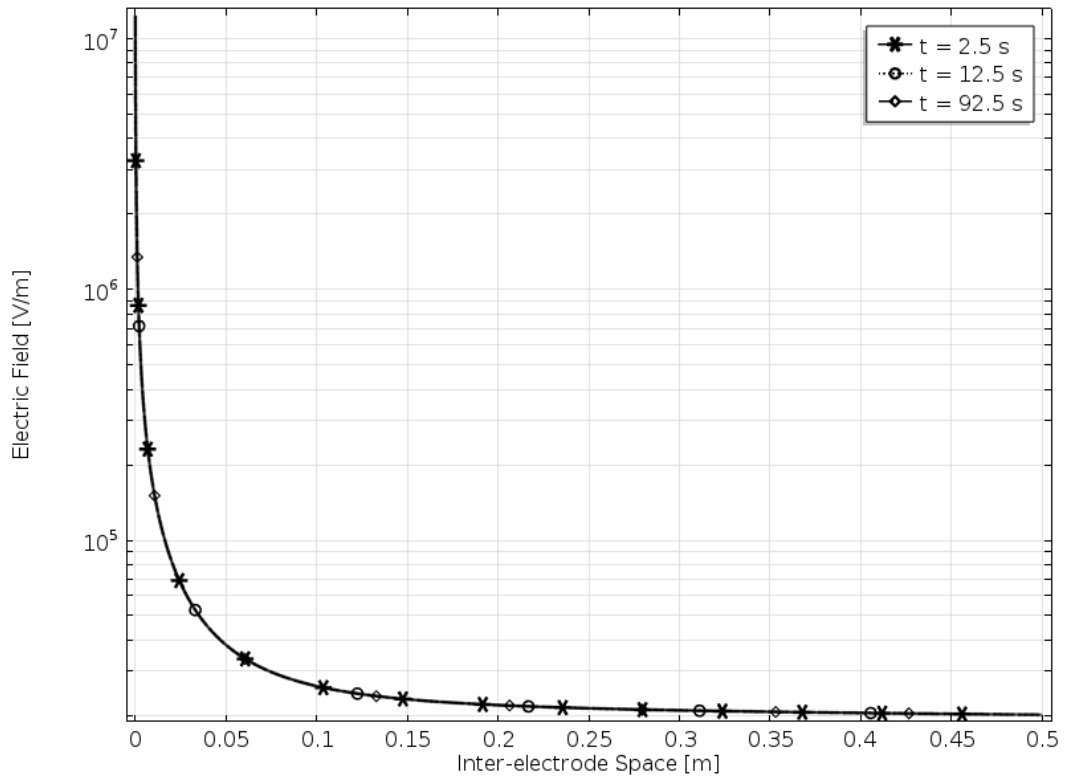


Figure 30. Distribution of the electric field strength in the inter-electrode space in the 0.1 Hz case at peak voltage. The difference in field distribution at the different time instants is so small that even with a logarithmic y-axis it will not show.

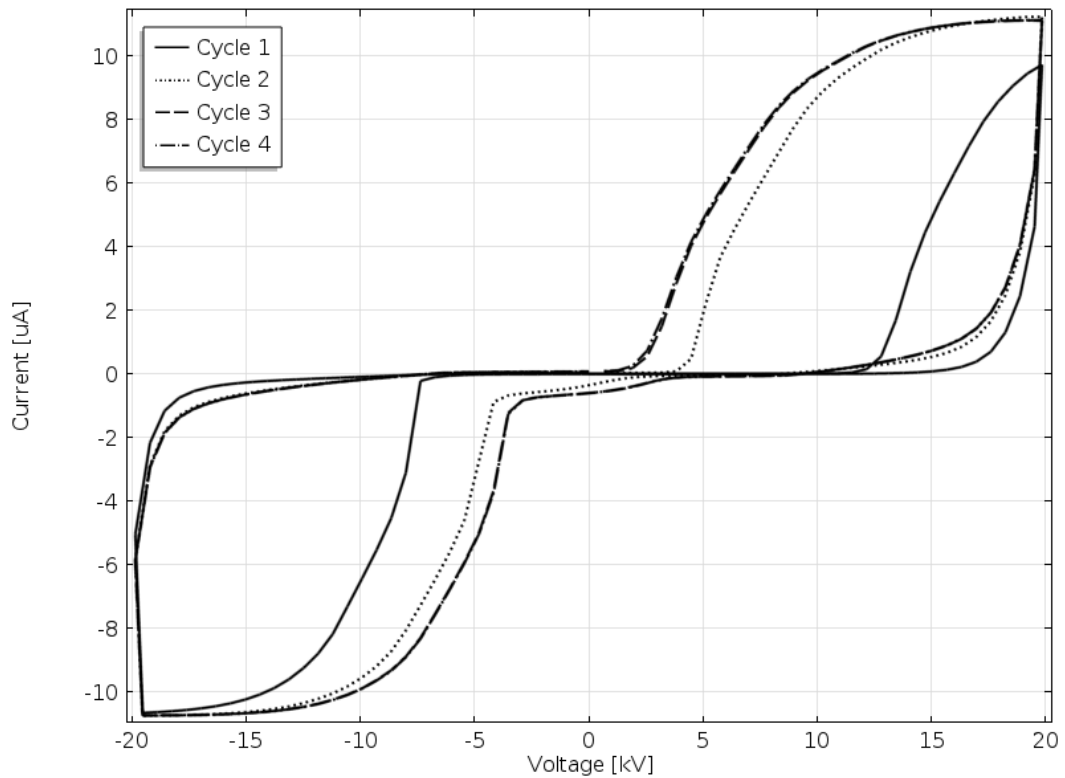


Figure 31. The current-voltage characteristics for the first four cycles for the 1 Hz case with a PVC-barrier. In the third cycle, a steady state value is reached for the discharge current and hence the third and the fourth cycles overlap.

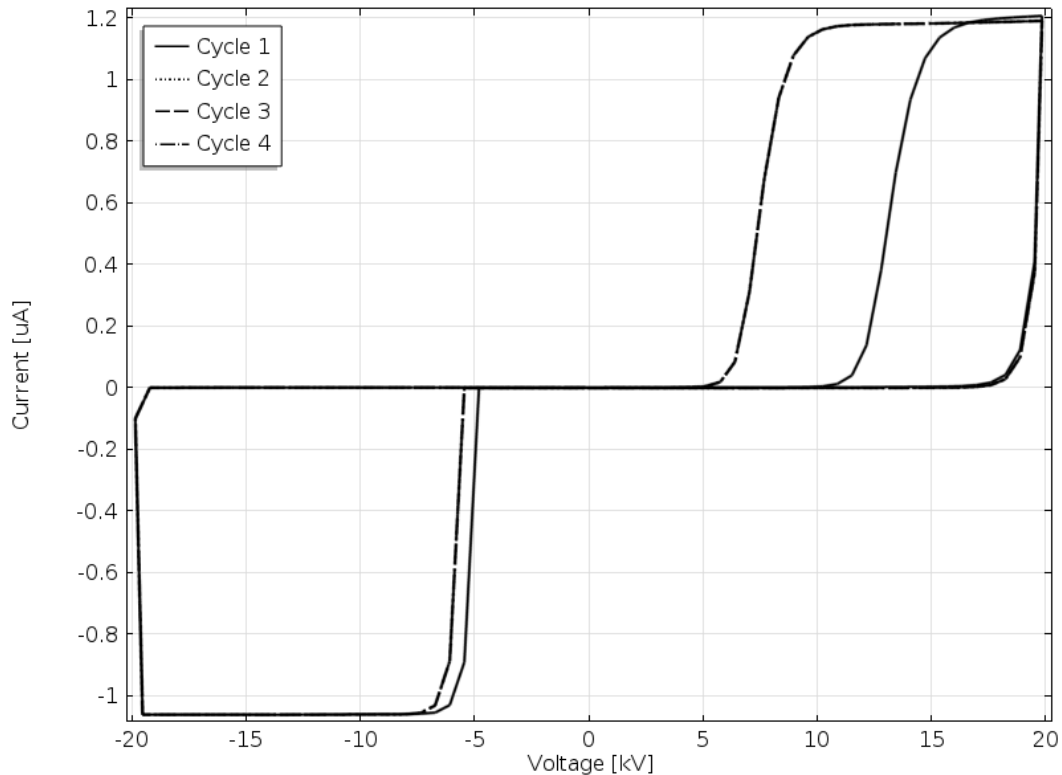


Figure 32. The current-voltage characteristics for the first four cycles in the 0.1 Hz case with the barrier. Steady state is reached at the second cycle, hence cycles 2-4 overlap.

Thus, the charges arrived at either side of the barrier are going to be accumulated. Since the simulations performed for the 50 Hz voltage in pure air showed that the charged species did not traverse the discharge gap and only moved a short distance into inter-electrode space, it is hard to expect formation of any significant surface charge layers at this frequency. Therefore, the simulations for the case with the barrier were performed for lower frequencies utilizing parameters indicated in the second column of Table 6.

The voltage-current characteristics computed for the first four cycles of the applied voltage are shown in Figure 31 and 32. As can be seen, it takes three cycles for the discharge current at 1 Hz to reach a steady state while in case of 0.1 Hz the current reaches steady state on the second cycle. As compared to the no-barrier equivalents (Figures 15 and 16, respectively), the currents levels are significantly lower. Here, the current peaks reaches 11 μA for the 1 Hz case and 1.2 μA the 0.1 Hz case while for the no-barrier case the respective values are 18 μA and 9 μA .

For the 1 Hz case, the positive onset voltage is 12.8 kV for the first cycle; it decreases down to ~ 5 kV at the second cycle and finally settles at around 2.4 kV. The negative onset voltage is lower, ~ 7.4 kV, for the first cycle, but does not reduce as dramatically, and becomes ~ 3.5 kV when the steady state is reached. For the 0.1 Hz case, the onset voltage for the first cycles is 11.1 kV for positive corona and

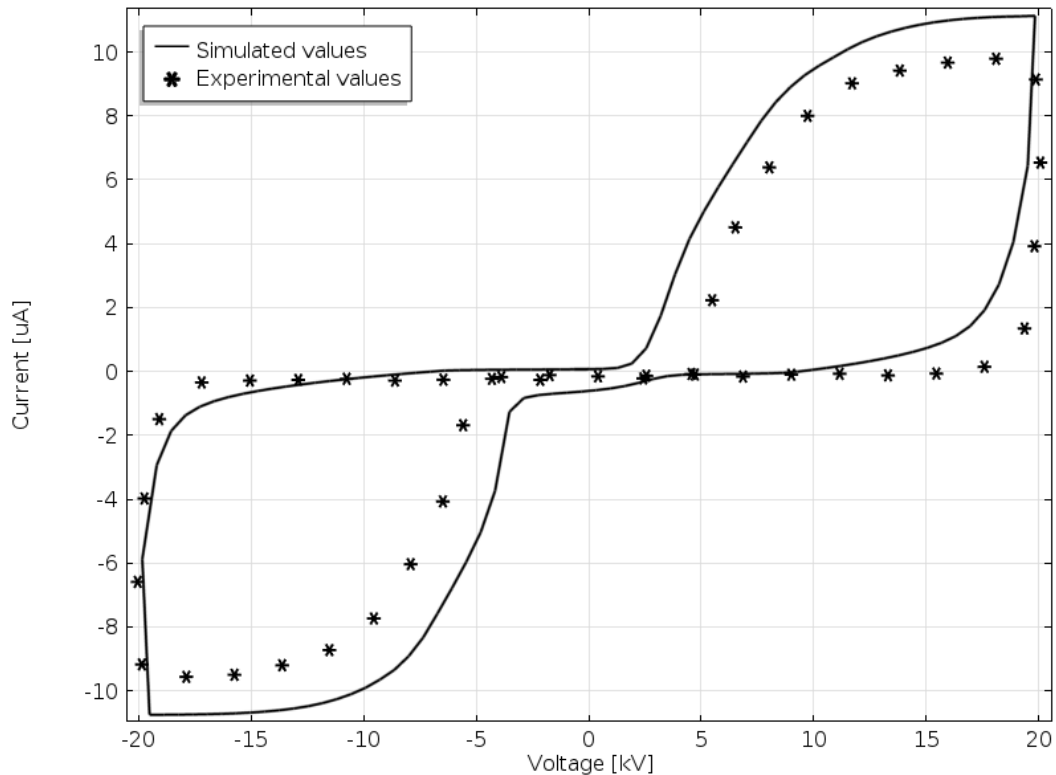


Figure 33. Comparison of the computed and measured current-voltage characteristics at steady state for 1 Hz case. Here, the original parameters described in Chapter 4 are used in the simulations.

5.5 kV for negative discharge during the first cycle of the voltage. At steady state, the corona onset stabilizes at 5.3 kV and at 4.9 kV for positive and negative polarities, respectively.

A comparison between the simulated and the experimental characteristics, Figure 33 and 34, shows in general a good fit. Although the agreement is not perfect, the basic features of the voltage-current characteristics are preserved in both (1 Hz and the 0.1 Hz) cases. As it is seen, the onset voltages for both positive and negative corona are lower in the simulations for the frequency of 1 Hz. As mentioned above, the calculated positive onset voltage is about 2.4 kV whereas the experimental value is around 5 kV. The peak current obtained from the simulations is 11.2 μA that is slightly higher than the experimental value 9.8 μA . Also, the computed currents drop more rapidly than the measured ones while the voltage starts to decrease after passing the maximum values. In the 0.1 Hz case, the onset voltage is instead higher for the simulations and it is ~ 5.3 kV that is to be compared to ~ 2.3 kV from the experiments. The peak current reaches a slightly higher value ~ 1.18 μA as compared to the measured 0.98 μA . A better fit can be obtained for both cases by adjusting some of the model parameters. Such sets of data are provided in Appendix 2 and the results presented below are obtained using the parameters providing best agreement between the computed and measured discharge characteristics.

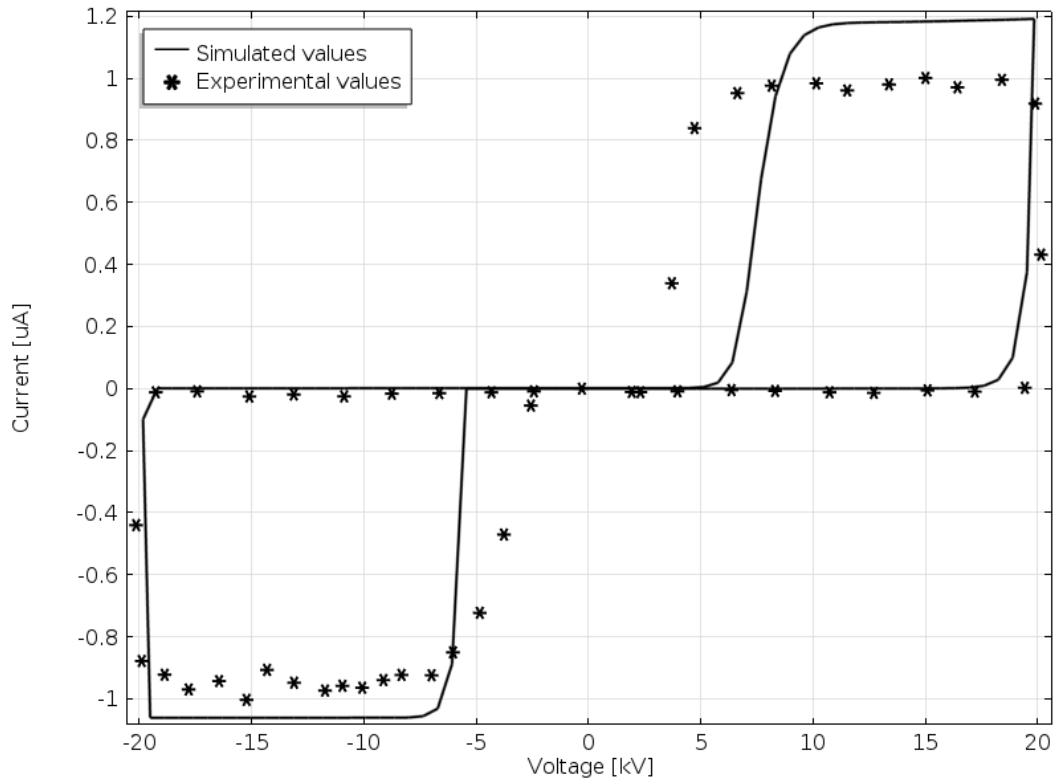


Figure 34. Comparison of the computed and measured current-voltage characteristics at steady state for the 0.1 Hz case. The original parameters from Chapter 4 are used in the simulations.

5.6. CORONA CURRENT COMPONENTS IN PRESENCE OF BARRIER

The current components described in (55), for both 1 Hz and 0.1 Hz are plotted in Figure 35 and Figure 36, respectively. When the current component plots are compared to their counterpart in the non-barrier case (Figures 18 and 19, respectively), it is obvious that there is no resemblance between the two 1 Hz cases or the two 0.1 Hz cases. Moreover, the simulations with barrier yield similar current components as for the 50 Hz non-barrier case (Figure 17). In general, this can be expected since the PVC-barrier blocks the ionic species from traversing the inter-electrode space just as in the 50 Hz non-barrier case where charge carriers are able to move only for a certain distance into the gas gap. This can also be an indication that the barrier is actually functioning as it should, not letting any charges pass through, and it is implemented into the software in a correct way. As seen from the figures, the ionic current is practically zero at both frequencies. As it comes to the capacitive current component, one may notice maximum magnitudes $I_{cap\ 1Hz} = 1.35\ \mu A$ and $I_{cap\ 0.1Hz} = 0.135\ \mu A$ showing the difference in ten times that is reasonable in regards to the difference in frequencies. The displacement current for the 1 Hz case is symmetric and reaches its maximum at $11.65\ \mu A$ for both semi-cycles. For the 0.1 Hz case, the positive peak displacement current has a slightly higher value, $1.445\ \mu A$, compared to the negative maximum at $-1.195\ \mu A$.

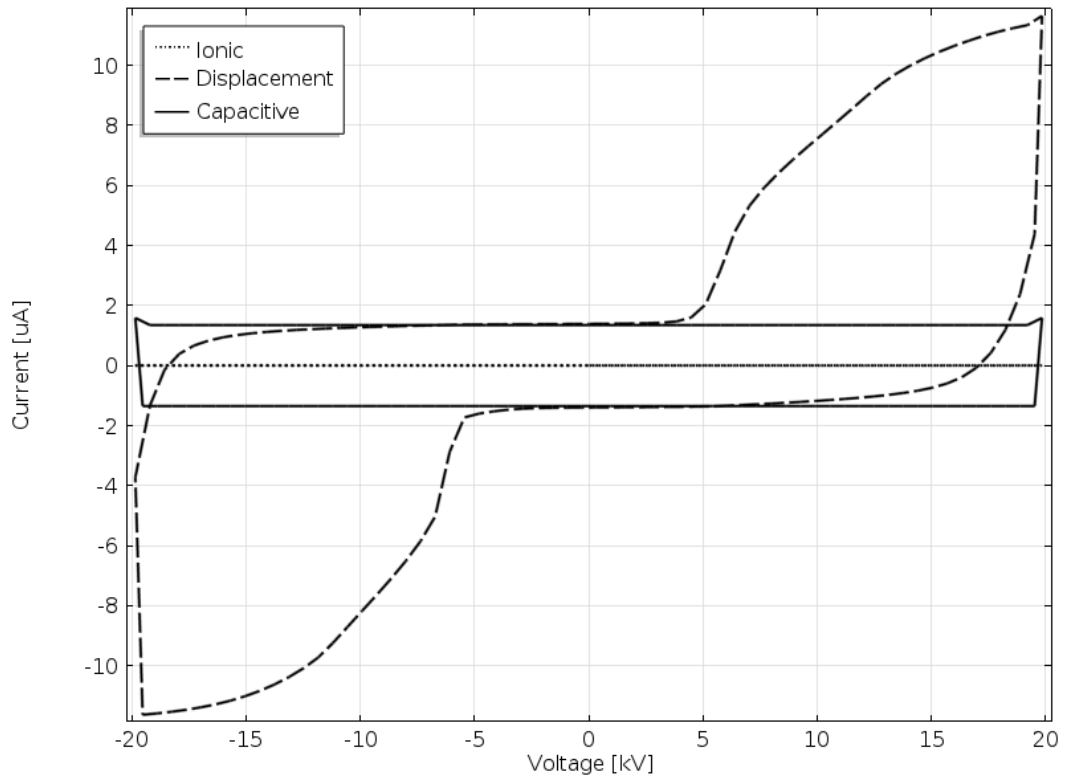


Figure 35. The current components versus voltage for the 1 Hz case. The ionic current is zero, since the PVC-barrier blocks the ionic discharge from reaching the cage side where the current is measured.

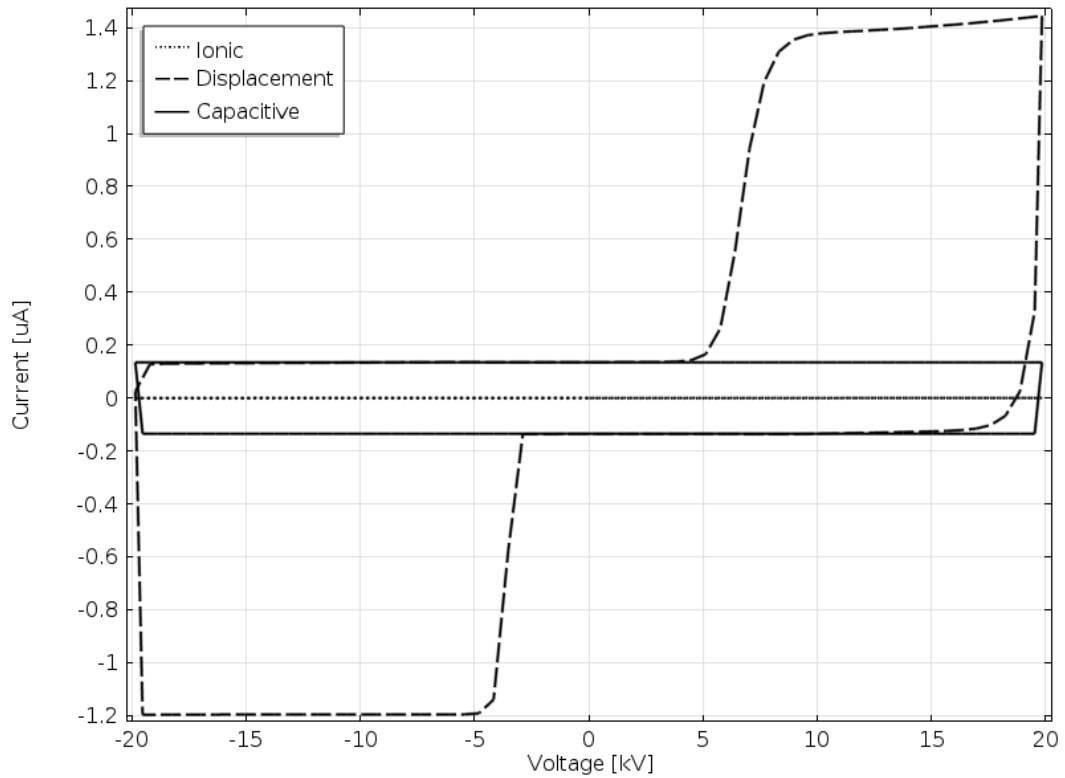


Figure 36. The current components plotted against voltage for the 0.1 Hz case. As for the figure above, the ionic current is zero since the PVC-barrier is blocking.

5.7. CHARGE ACCUMULATION ON BARRIER SURFACES

In this chapter the accumulation of the charged species, i.e. ions and electrons, at the PVC-barrier is investigated. As in the case of corona in pure air, there is still an accumulation of charged species in gas, in particular, at the cage. However, the accumulated space charges are expected to be weaker due to the fact that the gas volume is split into two smaller parts by the insulating element. Since the barrier interrupts the fluxes of charge carriers, the space charge collected at its surfaces is transformed into surface charge generating fields opposite to the applied field and thus affecting discharge development. Thus, time to steady state is much shorter. As it was mentioned above, a steady state is reached already after two cycles of the applied voltage. Due to this reason, the results of the simulations are shown below for the first four cycles only (compared to the first ten cycles in the case without barrier). Also, the dynamics of surface charges is studied for the internal side of the barrier facing to the corona wire since more charges tend to accumulate on this surface and, hence, have greater impact on the electric field distribution.

As seen in Figure 37, the electron concentration at the barrier at frequency of 1 Hz is close to zero during positive semi cycle of the applied voltage. The accumulation starts after polarity reversal and the peak is reached around the time instants when the voltage applied to the wire reaches its zero crossings. After the second cycle the peaks become regular with the maximum electron concentration $\sim 1.2 \cdot 10^4 \text{ m}^{-3}$ that is quite high as compared to the level of 250 m^{-3} accumulated at the cage in pure air (Figure 24). The relatively high electron concentrations can be explained by the fact that at the instants when they are reached, the ion-electron recombination rate is low. Even though the attachment rate increases along with the increase of electrons density, a certain time lag before the electron peak is reached allows for high intensity of electron detachment, which leads to the possibility of increased concentrations of electrons.

Variations of the densities of ionic species at the internal surface of the barrier are shown in Figure 38. It can be seen that the levels of magnitudes of ions densities are also higher than in the case of pure gas by 3-4 times. As compared with electrons, the accumulation of ions is more straightforward; positive ions reach the peak value as the applied voltage is at positive maximum and thus repelling positive ions away from the wire, and vice versa for negative ions.

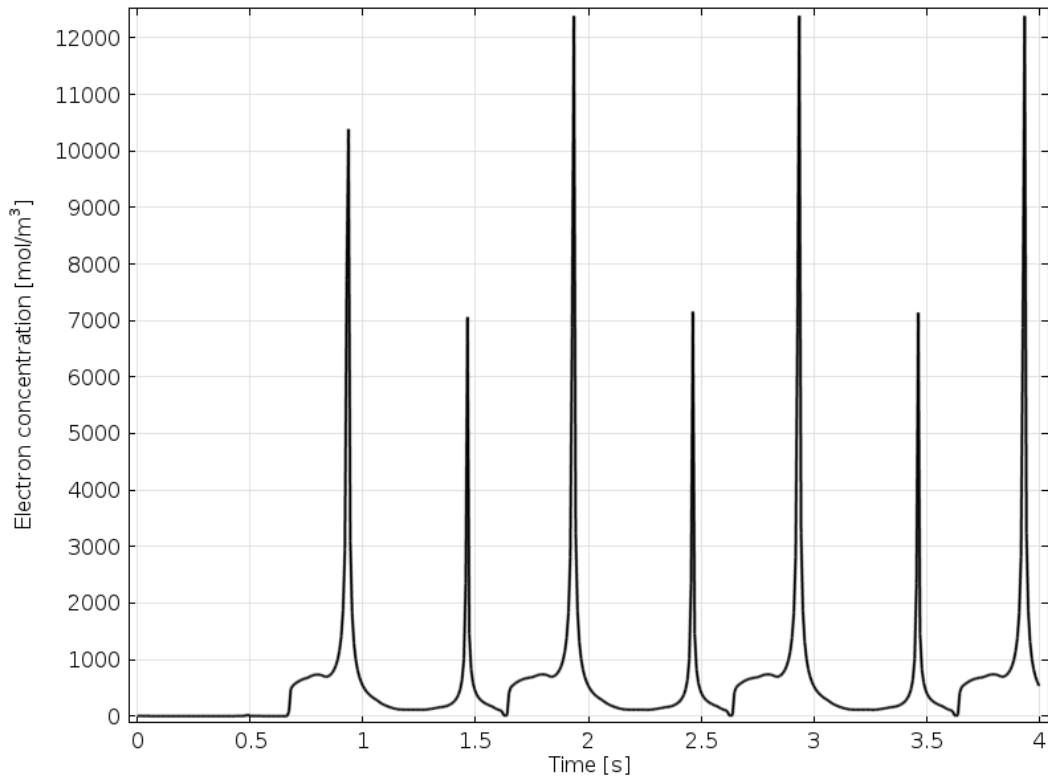


Figure 37. Electron concentration at the wire side of the PVC-barrier for the first four cycles in the 1 Hz case. The maximum peaks occurs at the instants when the concentration of ionic species at the barrier is very low.

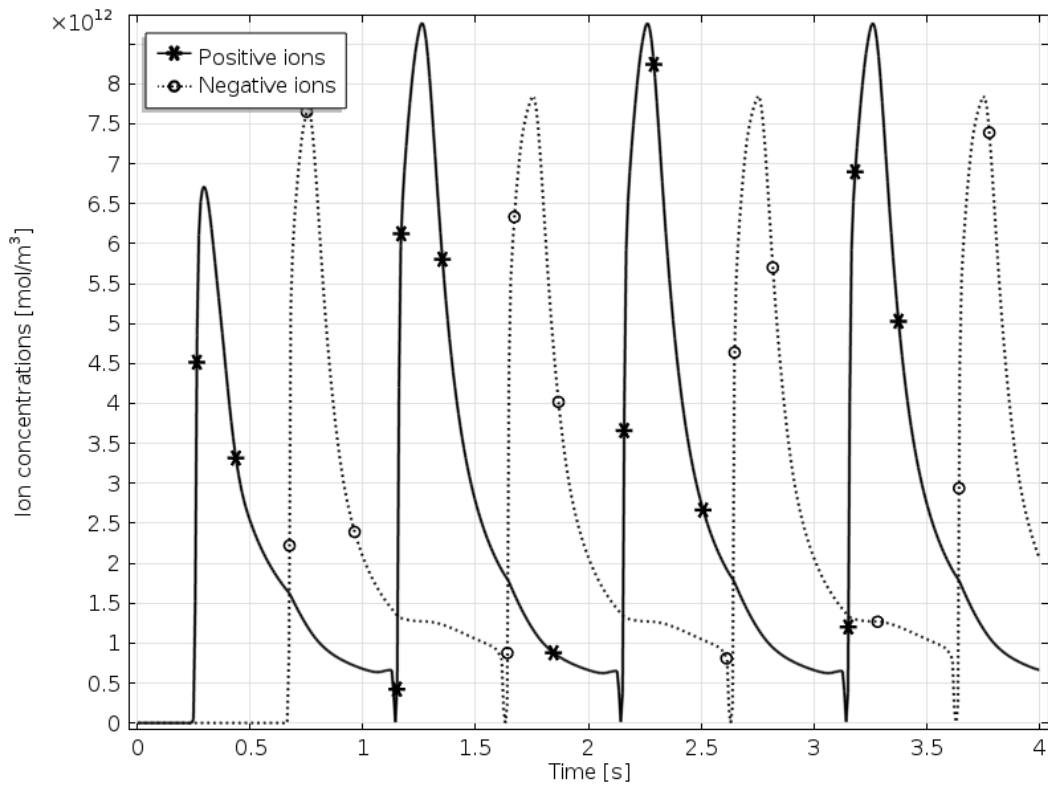


Figure 38. Concentrations of positive and negative ions at the wire side of the PVC-barrier for the first four cycles at frequency of 1 Hz.

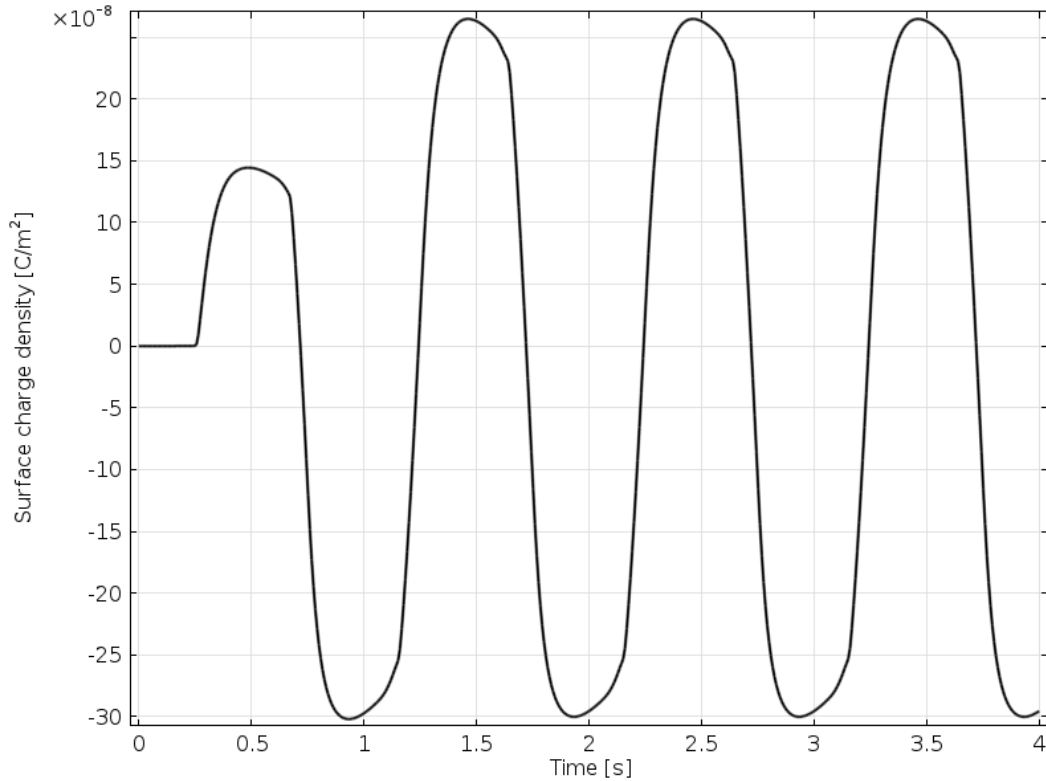


Figure 39. The surface charge density accumulated at the wire side of the PVC-barrier during the first four voltage cycles at 1 Hz. As can be seen, the charge accumulation reaches a steady state value already on the second cycle.

The surface charge density calculated using (42) as a function of time is shown in Figure 39. As seen, the accumulation of surface charge follows a smooth almost sinusoidal pattern with maximum growth at the time instants where the applied voltage has its peaks. That is expected as the fluxes tend to be strongest at these moments. In the positive voltage cycle, the positive charges dominate and continue doing so until the voltage reaches its zero crossing. On the negative voltage semi cycle, negative charges are dominant. One can notice also that the negative charge density is slightly higher with the maximum of -300 nC/m^2 while the maximum density of positive charges reaches 265 nC/m^2 . This difference may be attributed to the slightly higher mobility of the negative ions.

For the frequency 0.1 Hz, the electron accumulation reaches its highest rate already on the first cycle when the voltage is decreasing towards zero. The maximum electron peak reaches the value of 795 m^{-3} at $\sim 4 \text{ s}$ as can be seen in Figure 40 (note that half a cycle corresponds to 5 s). At this time instant, the concentrations of positive and negative ions are very low (Figure 41), allowing for a greater number of electrons to be accumulated. At steady state (after the first period), the pattern of electron density variations becomes regular and peaks of their concentrations reach the value of 170 m^{-3} . There are also longer time periods when the concentration is constant at 125 m^{-3} , which coincides with peaks of concentrations of negative ions.

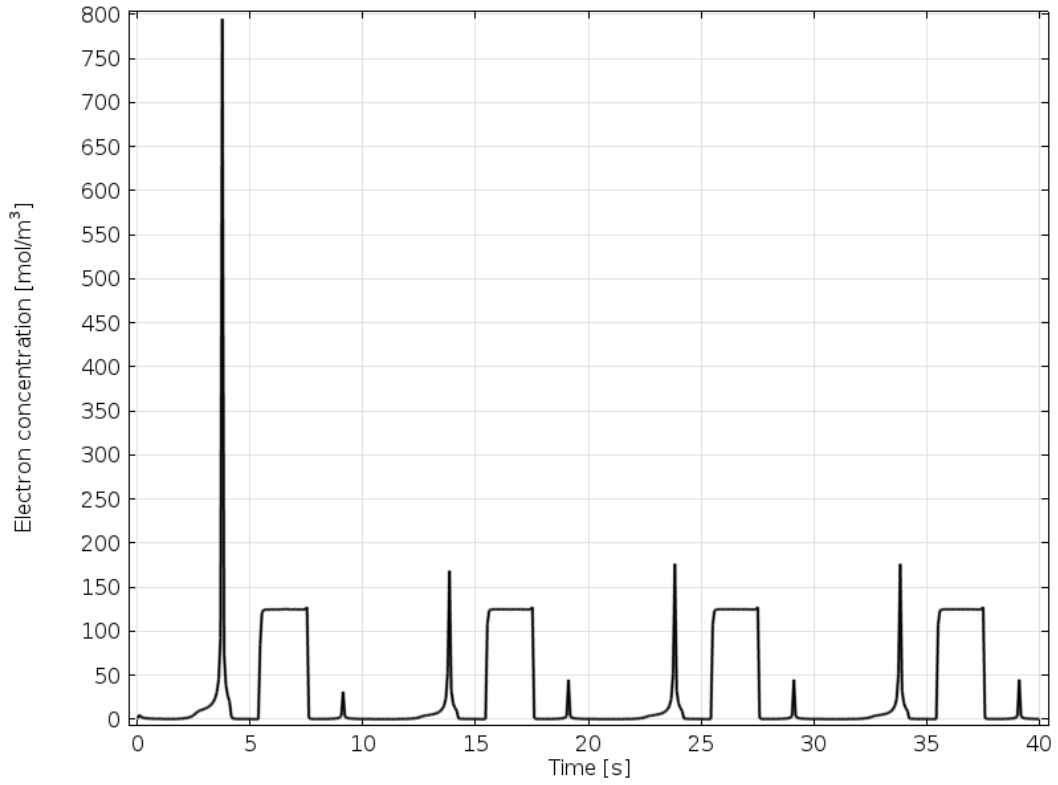


Figure 40. The concentration of free electrons at the wire side of the PVC-barrier during the first four cycles in the 0.1 Hz case.

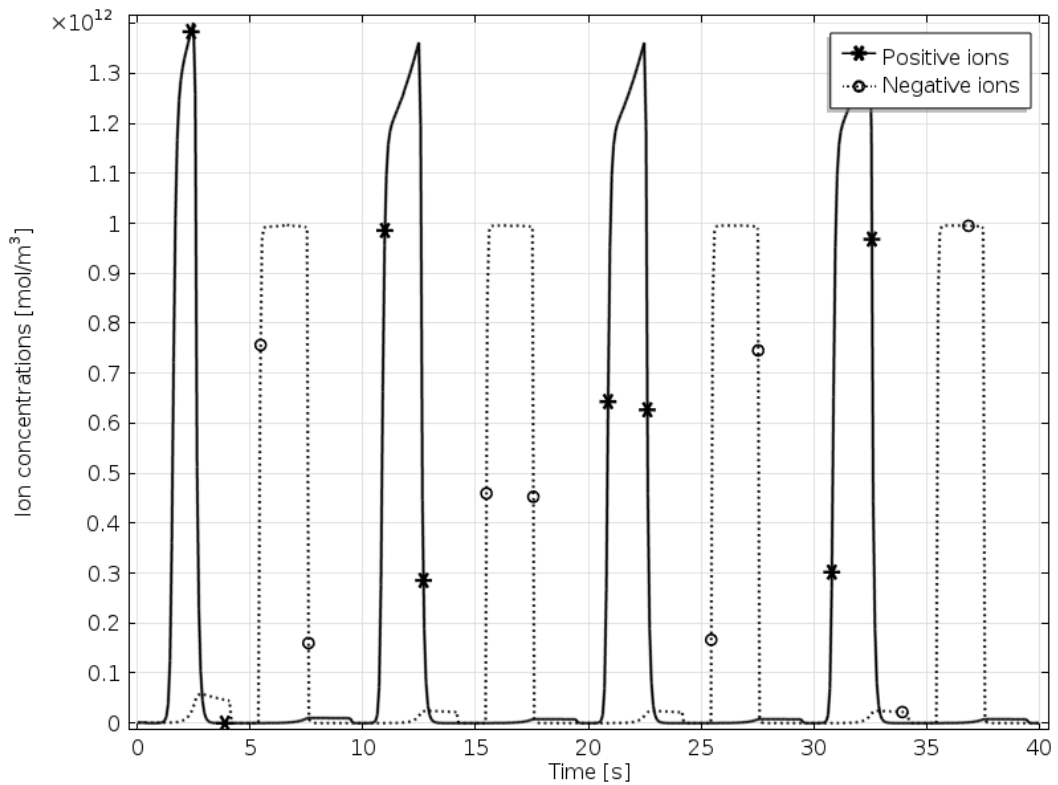


Figure 41. The concentration of positive and negative ions at the wire side of the PVC-barrier for the first four voltage cycles in the 0.1 Hz case.

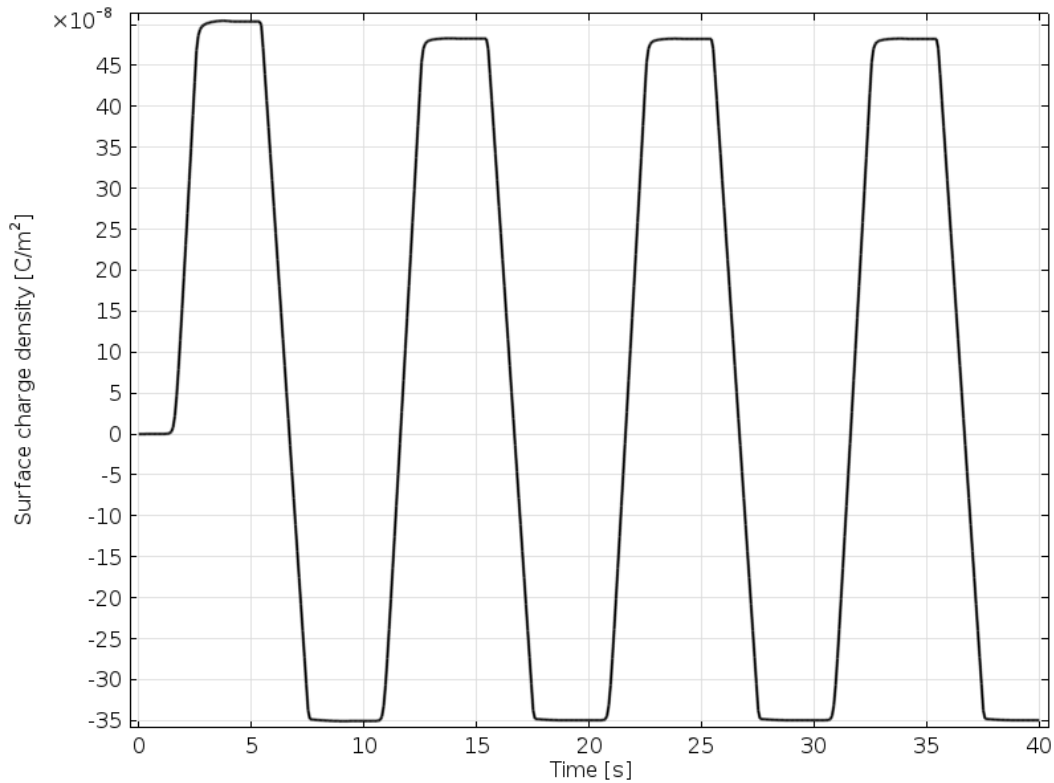


Figure 42. The surface charge density at the wire side of the PVC-barrier accumulated over the first four voltage cycles in the 0.1 Hz case.

As seen in Figure 41, the steady state peak concentrations of positive and negative ions at the barrier surface at frequency 0.1 Hz ($1.3 \cdot 10^{12} \text{ m}^{-3}$ and $1 \cdot 10^{12} \text{ m}^{-3}$, respectively) are lower than the corresponding magnitudes at frequency 1 Hz ($8.9 \cdot 10^{12} \text{ m}^{-3}$ and $7.8 \cdot 10^{12} \text{ m}^{-3}$, respectively, Figure 38). This may be attributed to much longer characteristic times during which ion-ion recombination becomes essential.

The variations of the surface charge density at the PVC-barrier are shown in Figure 42. As seen, the surface is recharged periodically. At steady state (after the first cycle), the positive charge density reaches 480 nC/m^2 while the maximum of the negative charge density is -350 nC/m^2 . In general, these values are higher than the corresponding magnitudes obtained for higher frequency of 1 Hz (compare with Figure 39). Another difference is that the higher value of charge density was acquired for negative charge in the 1 Hz case where the positive charge instead accumulates the higher value in the 0.1 Hz case. Two reasons for this might be that the concentration of free electrons is much higher at the PVC-barrier at all instants of time for the 1 Hz case, and also that there is a bigger difference in accumulation between positive and negative ions in the 0.1 Hz case.

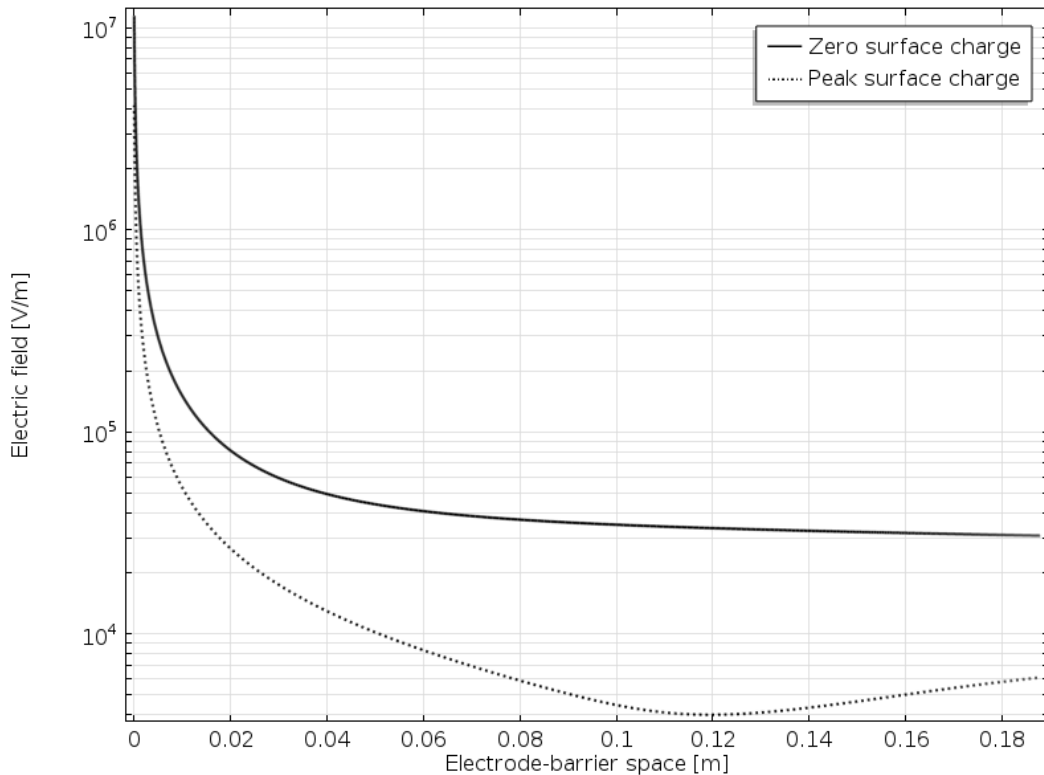


Figure 43. The electric field distribution in the electrode-barrier space for the 1 Hz case. The field strength decreases as more surface charges are accumulated at the wire side of the PVC-barrier.

5.8. IMPACT OF SURFACE CHARGE ON THE BARRIER ON ELECTRIC FIELD DISTRIBUTION

One of the most interesting questions related to accumulation of charges at the PVC-barrier is how they influence the electric field strength within the barrier and in surrounding air. This question is also of practical significance because if the field strength reaches too high values, in the long run it accelerates ageing process and may eventually lead to a complete breakdown or flashover. The following studies of the electric field strength are done both within the PVC-barrier and also between the wire and the barrier. The analysis is to be conducted for two cases - when the surface charge is zero and when the charge accumulation reaches its positive peak. The electric field strength between the wire and the barrier is expected to be higher in the former case and decrease while charge is accumulated. The situation inside the barrier is instead reversed. The field is expected to be lower when the charge accumulation is negligible and to be more enhanced with the increase of accumulated charges.

As shown in Figure 43 for the case of 1 Hz, the electric field in the gap between the wire electrode and the barrier is strongest at the points closest to the wire that is expected. The field peak at zero

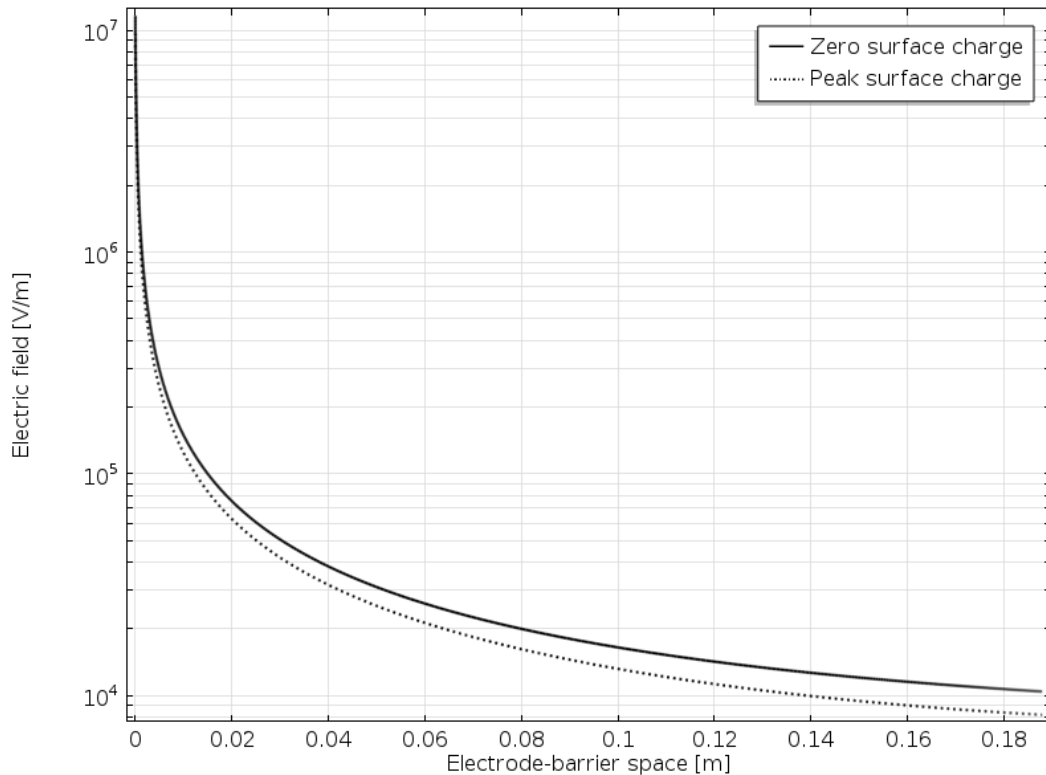


Figure 44. *The electric field distribution in the electrode-barrier space for the 0.1 Hz case. Even though the field strength decreases with accumulation of charges, the decrease is not as pronounced as for the 1 Hz case.*

surface charge reaches $11.48 \cdot 10^6$ V/m. When the positive accumulated charge is at maximum, the peak of the field is reduced to $4.14 \cdot 10^6$ V/m. Moreover, the field strength in the entire gap between the wire and the barrier is significantly reduced. In the vicinity of the PVC-barrier, the field drops from 31 kV/m at zero charge down to 6 kV/m at peak charge accumulation.

At frequency 0.1 Hz (Figure 44), the alteration of field strength outside the barrier is less pronounced with a maximum of 11.7 MV/m close to the wire at zero charge accumulation and a maximum of 9.7 MV/m when the charge accumulation is at peak. Closer to the PVC-barrier, the difference is even smaller; 10.5 kV/m at zero charge accumulation compared to 8.3 kV/m at peak accumulation.

The increase of field strength within the barrier is not very dramatic for the 1 Hz case. As seen in Figure 45, the field increases from a maximum of 8.45 kV/m at zero charge accumulation to a maximum of 9.78 kV/m at peak surface charge accumulation. In the 0.1 Hz case (Figure 46), the change is more essential; from a maximum value of just under 4 kV/m with no charge accumulation up to the value of 17 kV/m at full charge accumulation. As seen in Figure 46, the distribution of the field inside the barrier is linear, with a lowest value of 15.9 kV/m at the side of the barrier facing the cage.

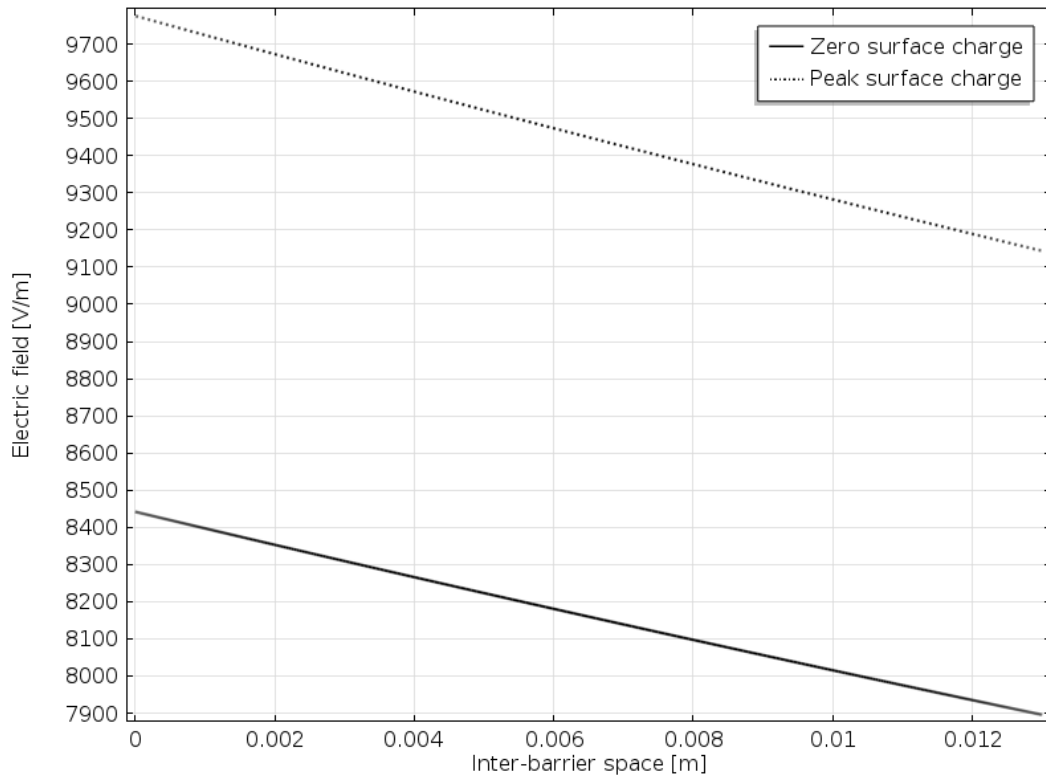


Figure 45. The electric field distribution inside the PVC-barrier for the 1 Hz case. The field strength inside the barrier increases with increased accumulation of charges.

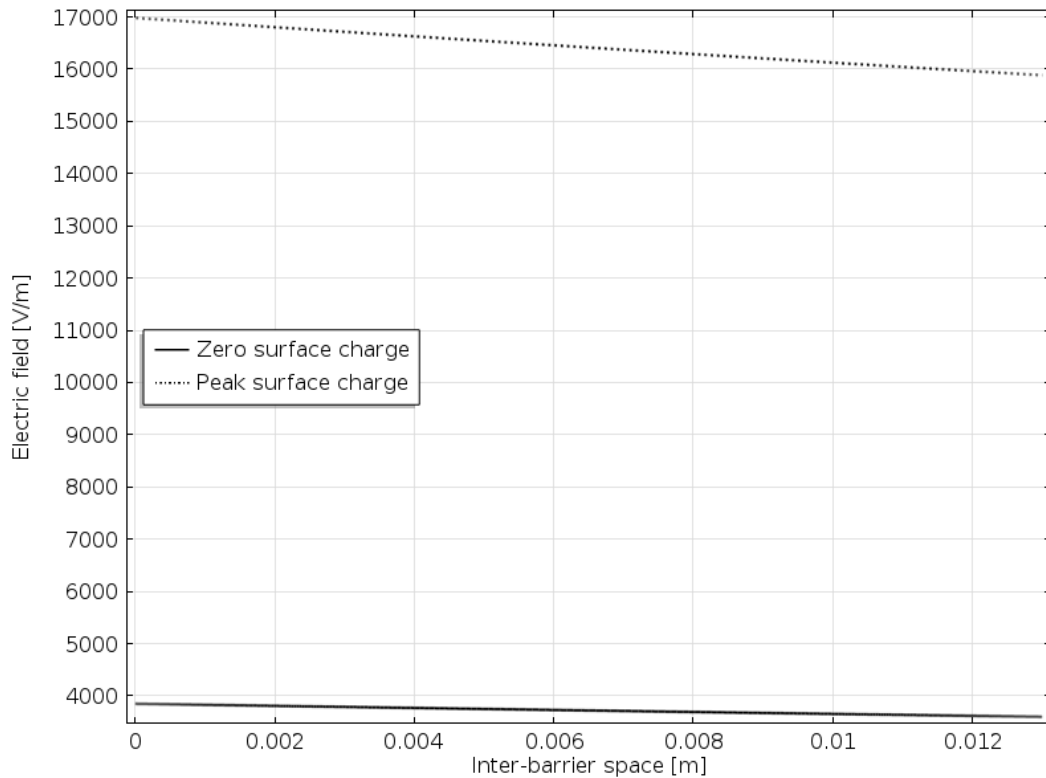


Figure 46. The electric field distribution inside the PVC-barrier for the 0.1 Hz case. The field strength inside the barrier increases with increased accumulation of charges and thus increases the risk for a flashover and increased rate of ageing.

CHAPTER

6

CONCLUSIONS

As shown in Chapter 5, the simulation model implemented in COMSOL Multiphysics proves to function in an accurate way. In this chapter some further evaluation of the model and a brief review of how the model could be developed further are discussed.

6.1. EVALUATION OF THE MODEL

The fact that COMSOL Multiphysics software can be used to successfully solve corona discharge models and provides accurate and trustworthy results have been proven without doubts. The simulations conducted for all considered cases (pure air and barrier included at different frequencies) yielded the current-voltage characteristics which are in general in a good match with the experimental results.

Alteration of some basic parameters, as discussed in Chapter 5, was necessary to provide a fit as accurate as possible although these changes were within the limits of typical variations of the parameters reported in the literature. However, only a few parameters have been subjected to the alteration, and it is not proven that by adjusting a different parameter the same result might be obtained.

Modelling of corona discharges with an alternating voltage is not straightforward, as some of the variables included are dependent on the direction of the electric field. As can be assessed from the simulation results, the field dependent variables seem to function as expected and no non-physical occurrences has been discovered, such as unwanted ion accumulation due to the flux been directed in the wrong direction. This could easily be a problem, as the direction vectors defined internally in COMSOL does not always show very clearly.

One big problem when working on this thesis has been how to implement the PVC-barrier in a correct physical way. Is it accurate to assume that no ionic transport takes place through it? How can the charges accumulating at the barrier be accounted for in a good way? When studying the current

components, it is obvious that the barrier behaves as expected since no ionic current from the wire reaches the cage side when it is included. There is also an accumulation occurring which works with the direction of the electric field, i.e. accumulation of the correct type of charged species occurs at the barrier when it is supposed to.

How the accumulation of charges impact on the electric field distribution has also been studied, both inside the PVC-barrier and outside. When charges accumulate, the field strength inside the barrier increases while the field strength outside decreases, which is according to theory and also shows that the accumulation functions in a correct way.

Not all parameters and variables accounted for have been investigated separately, and therefore no deeper evaluation of each parameter is available. Probably, some parameters may have stronger impact than other, while some might prove unnecessary. However, inclusion of these parameters seems reasonable from a theoretic point of view, and as the results obtained are pleasing it is assumed that they all combine when providing the result.

All in all, the simulation model functions in a satisfying way and the mathematical implementation of the problem seems to be trustworthy even for cases where there are no precedent experimental results to be compared to for evaluation.

6.2. FUTURE WORK

It has been shown in all simulation, independently on frequency, how significant the implementation of physically correct boundary conditions is. To have the flux of ions and electrons over the boundaries and at the barrier functioning in a correct way is of the outermost importance for the simulations to eventuate in fair results.

The interaction of ions and electrons with the electrode surface or the PVC-surface of the barrier is in this thesis described as a straightforward convective flux out of the model. In reality, there are additional processes influencing this interaction. For example, some electrons may be attached to the surface due to small fluctuations of potential along the surface area in what is known as 'sticky surface'. This is strongly dependent on the surface structure and material characteristics. In this thesis, as surfaces has been treated as perfectly smooth, no attention have been given to electron or ion interaction. However, the interaction of different materials is a research topic in itself and it is hard to estimate what impact it would have on improving the simulated results. As the results for the simulated discharge current also render a great fit, maybe such detailed implementations are not

necessary other than for cases where the charged species/barrier-interaction is of greater importance.

Since no values for air pressure and temperature from the experiments were provided, these parameters were considered in the simulations as being the same as their respective references. Even though correction for relative air density has been implemented into the model, the resulting impact of changing of these parameters has not been investigated.

Even as for the other parameters included in the model, more detailed studies of the impact of each of these parameters could be interesting. As the computational time and power needed for simulations more than ten cycles proved to be very high, there might be ways to reduce this by disregard some factors that does not have a huge impact on the results, and therefore save valuable computational power. If the number of computations could be scaled down and still provide an accurate enough result, simulations for longer time periods could be carried out, which could be of greater interest if a more detailed accumulation of charged species at the barrier is provided, i.e. the long term effect of charge accumulation on the electric field strength could be studied.

REFERENCES

- [1] G. Karman, *Simulation and Analysis of Corona Currents in Large Scale Coaxial Geometry due to Triangular Voltages*, Diploma Work No. 123/2013, Dept. of Materials and Manufacturing Technol., Div. of High Voltage Engineering, Chalmers University of Technology, 2013.
- [2] E. Kuffel, W.S. Zaengl, J. Kuffel, *High Voltage Engineering: Fundamentals*, Burlington, MA, Newsnes 2000.
- [3] Y. V. Serdyuk, *Numerical Simulations of Non-Thermal Electrical Discharges in Air*, Lightning Electromagnetics, IET Power and Energy, The Institution of Engineering and Technology; 1st Edition, 2012, pp. 87-138.
- [4] S. Pancheshnyi, *Role of Electronegative Gas Admixtures in Streamer Start, Propagation and Branching Phenomena*, Plasma Sources Sci. Technol. 14 645, 2005.
- [5] S. D. Pawar, P. Murugavel, D.M. Lal, *Effect of Relative Humidity and Sea Level Pressure on Electrical Conductivity of Air Over Indian Ocean*, Journal of Geophysical Research, Vol. 114, 2009.
- [6] J. M. Meek, J. D. Craggs, *Electrical Breakdown of Gases*, Wiley Series in Plasma Physics, John Wiley & Sons, Ltd, 1978.
- [7] I. A. Kossyi et al., *Kinetic Scheme of the Non-Equilibrium Discharge in Nitrogen-Oxygen Mixtures*, Plasma Sources Sci. Technol., Vol. 1, 1992, , pp. 207-220.
- [8] S. Chandrasekhar, *Stochastic Problems in Physics and Astronomy*, Reviews of Modern Physics, Vol. 15, Nr 1, Jan 1943, pp. 41.
- [9] G. G. Raju, *Gaseous Electronics - Theory and Practice*, CRC Press, 2006.
- [10] E. Kuffel, *Electron Attachment Coefficients in Oxygen, Dry Air, Humid Air and Water Vapour*, Proc. Phys. Soc. 74 297, 1959.
- [11] N. Y. Babaeva, J. K. Lee, *Dust-Grain Charging in Developing Air Plasma*, IEEE Transaction on Plasma Science, Vol. 32, No. 2, April 2004.
- [12] J. Sayers, *Ionic Recombination in Air*, Proc. R. Soc. Lond. A, 1938.
- [13] N. Y. Babaeva, J. K. Lee, H. C. Kim, *Non-Stationary Charging of a Dust Grain in Decaying Streamer-Channel Plasma*, Plasma Source Sci. Technol. 13, 2004, pp. 127-134.
- [14] J. P. Boeuf, L.C. Pitchford, *Two-dimensional Model of a Capacitively Coupled RF Discharge and Comparisons with Experiments in the Gaseous Electronics Conference Reference Reactor*, Phys. Rev. E, Vol .51, Nr. 2., 1995, pp. 1376-1390.
- [15] L. B. Loeb, *Electrical Coronas*, University of California Press, Berkeley, 1965.

- [16] F. W. Peek, *Dielectric Phenomena in High-Voltage Engineering*, McGraw-Hill, New York, 1929.
- [17] A. F. Kip, *Positive Point to Plane Discharge in Air at Atmospheric Pressure*, Phys. Rev. 54, 1938, pp. 139-46.
- [18] P. Grünberg, *The Validity of the Similarity Laws for the Onset of the First Independent Discharges in Air*, Elektrotech. Z. ETZ A, 94, 1973, pp. 20-25.
- [19] E. Nasser, M. Heiszler, *Mathematical Physical Model of the Streamer in Nonuniform Fields*, J. Appl. Phys. 45, 1974, pp. 3396-3401.
- [20] R. T. Waters, W. B. Stark, *Characteristics of the Stabilized Glow Discharge in Air*, J. Phys. D: Appl. Phys. 8, 1975, pp. 416-26.
- [21] F. D'Allesandro, G. Berger, *Laboratory Studies of Corona Emissions From Air Terminals*, J. Phys. D: Appl. Phys. 32, 1999, pp. 2785-90.
- [22] C. B. Moore et al, *Lightning Rod Improvement Studies*, J. Appl. Met. 39, 2000, pp. 539-609.
- [23] M. Goldman, A. Goldman, *Corona Discharges*, Gaseous Electronics, ed. M. N. Hirsh and H. J. Oskam, New York: Academic, 1978, pp. 219.
- [24] J. Schiessling et al, *Measurements and Simulations of Corona Currents due to Triangular Voltages in Large Scale Coaxial Geometry*, 2012 Annual Conference on Electrical Insulation and Dielectric Phenomena (CEIDP), 2012, pp. 357-360.
- [25] J. J. Lowke, *Theory of Electrical Breakdown in Air – The Role of Metastable Oxygen Molecules*, J. Phys. D: Appl. Phys. 25, 1991.
- [26] J. L. Morruzi, D. A. Price, *Ionization, Attachment and Detachment in Air-CO₂ Mixtures*, J. Phys. D: Appl. Phys. 7, 1974.
- [27] C. Raja Rao, G. R. Govinda Raju, *Growth of Ionization Currents in Dry Air at High Values of E/N*, J. Phys. D: Appl. Phys. 4 494, 1971.
- [28] L. G. Huxley, R. W. Crompton, *The Diffusion and Drift of Electrons in Gases*, Wiley, 1974.
- [29] U. Horrak, et al., *Mobility Spectrum of Air Ions at Tahkuse Observatory*, J. Geophys. Res. Atmospheres, Vol. 99, 1994.

APPENDIX

1

In Appendix 1, the tabulated values for the reduced ionization coefficient α/N can be found in Table 7; the values for the reduced attachment coefficient η/N are provided in Table 8; the magnitudes of the reduced electron drift velocity w_e are summarized in Table 9; and the tabulated values for the characteristic electron energy D/μ are given in Table 10.

Table 7. *Tabulated values for the reduced ionization coefficient α/N from Chapter 4.5. Values are scaled by 10^{-20} .*

E/N [Td]	α/N [m^2]
95	0.0001
100	0.0002
105	0.0009
110	0.0020
120	0.0062
125	0.0073
150	0.0185
175	0.0306
200	0.0521
250	0.1090
300	0.199
350	0.265
400	0.368
450	0.458
500	0.549
600	0.760
700	0.908
800	1.091
900	1.33
1000	1.43
1100	1.51
1200	1.71
1300	1.87
1400	1.98
1500	2.06
1600	2.17
1700	2.29
1800	2.40

Table 8. Tabulated values for the reduced attachment coefficient η/N discussed in Chapter 4.6.

E/N [Td]	$\eta/N \cdot 10^{-23}$
0	60
0.993555	49.5408
1.93867	24.6223
2.77222	16.1829
3.63035	11.4525
4.72627	8.10457
6.37375	5.92908
9.66502	3.83408
13.3431	2.66954
18.6387	1.90547
26.1899	1.39426
37.4573	1.12665
44.4053	1.07302
51.4247	1.11907
61.7007	1.48336
75.3488	2.08348
90.9383	2.78470
104.713	3.45440
117.766	3.88022
138.808	4.18307
166.507	4.22145
213.041	3.98891
249.595	3.52659
319.319	2.96830
401.387	2.47763
504.551	2.08522
608.727	1.84380

Table 9. Tabulated values for the reduced electron drift velocity w_e discussed in Chapter 4.7.

E/N [Td]	w_e [m/s]
0	0
0.3	3600
0.4	4000
0.6	4910
0.8	5780
1	6580
2	9520
3	11 360
4	12 760
6	15 500
8	18 260
10	21 000
20	38 000
30	50 000
100	122 000
200	200 000
300	267 000
400	323 000
500	380 000
600	439 000

Table 10. Tabulated values for the characteristic electron energy D/μ discussed in Chapter 4.7.

E/N [Td]	D/μ [eV]
0	0
2	0.29
3	0.4
5	0.62
8	0.85
10	0.95
16.5	1.15
20	1.25
30	1.26
40	1.3
50	1.35
70	1.6
100	2.15
200	4
300	5.25
400	6.5
500	7.5
600	8.6

APPENDIX

2

Appendix 2 shows the parameters providing the best fit of current-voltage characteristics as discussed in section 5.5 and corresponding plots are shown. The cases discussed in section 5.5 are for simulations for 1 Hz and 0.1 Hz voltage frequency in case of PVC-barrier included in the discharge gap. To get a fit that is equally good as in the cases without barrier is harder, but it is still possible to refine the fit with additional time.

In Figure 47, the best fit for the 1 Hz case is shown. As can be seen, the simulated values do not increase as fast as the experimental values on the rise of the positive corona, and the extinction of the corona is faster. Still, the peak current and the inception voltage are in a good match. For the negative corona cycle, the inception voltage matches well, but there is a slight discrepancy between the peak currents. For the 0.1 Hz case shown in Figure 48, the discrepancy between the simulated values and experimental values is even more visible. It should be noted that the current peak is lower in this case, and although the discrepancy is more pronounced in the figure, it is only in the range of 0.2 μA . In this case, it was discovered to be a tradeoff between having a good match on the peak current or a good match on the inception voltage. The case shown here is chosen to be somewhere in between, with a slight discrepancy for both.

Table 11. *Original and corrected values to achieve the best fits for the 1 Hz and 0.1 Hz cases with a PVC-barrier included.*

	Name:	Original value:	Corrected value:
<i>1 Hz case</i>			
Mobility of positive ions	μ_p	$1.5 \cdot 10^{-4}$	$0.7 \cdot 10^{-4}$
Mobility of negative ions	μ_n	$1.7 \cdot 10^{-4}$	$1.0 \cdot 10^{-4}$
Secondary ionization coefficient	γ	$2 \cdot 10^{-5}$	$2 \cdot 10^{-4}$
Background ionization rate	R_0	$1.5 \cdot 10^9$	$1.5 \cdot 10^7$
<i>0.1 Hz case</i>			
Mobility of positive ions	μ_p	$1.5 \cdot 10^{-4}$	$2.3 \cdot 10^{-4}$
Mobility of negative ions	μ_n	$1.7 \cdot 10^{-4}$	$2.5 \cdot 10^{-4}$
Background ionization rate	R_0	$1.5 \cdot 10^9$	$1.5 \cdot 10^7$

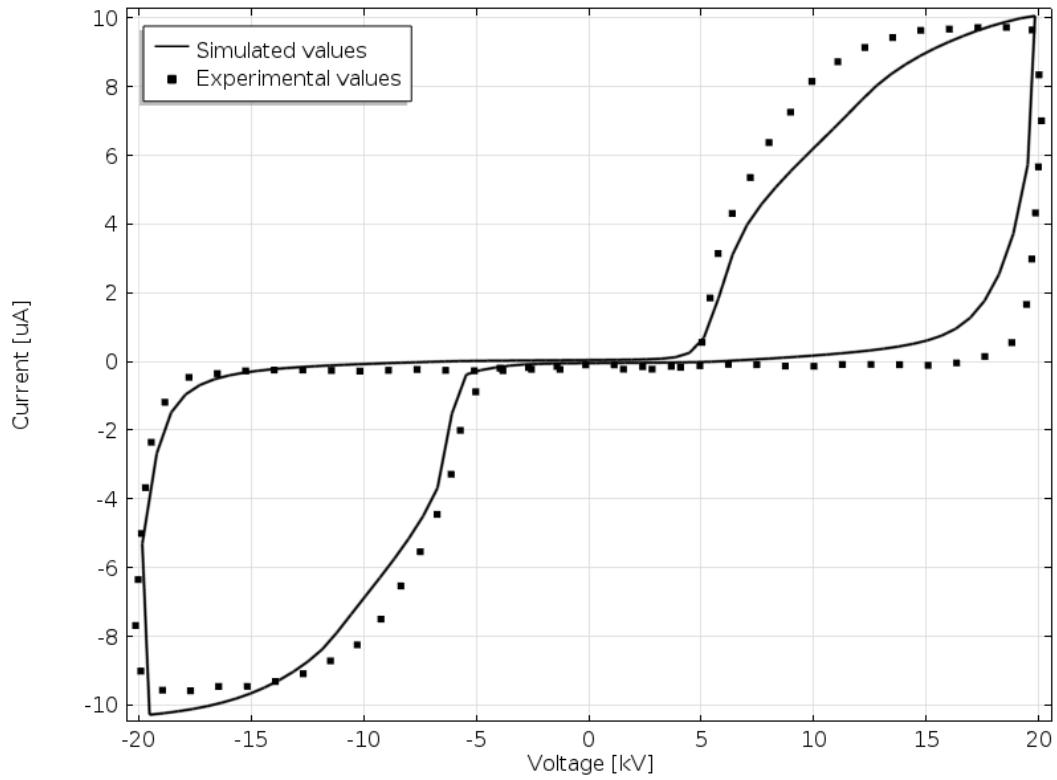


Figure 47. Best fit achieved for the current-voltage characteristics in the 1 Hz case for when a PVC-barrier is included in the discharge gap.

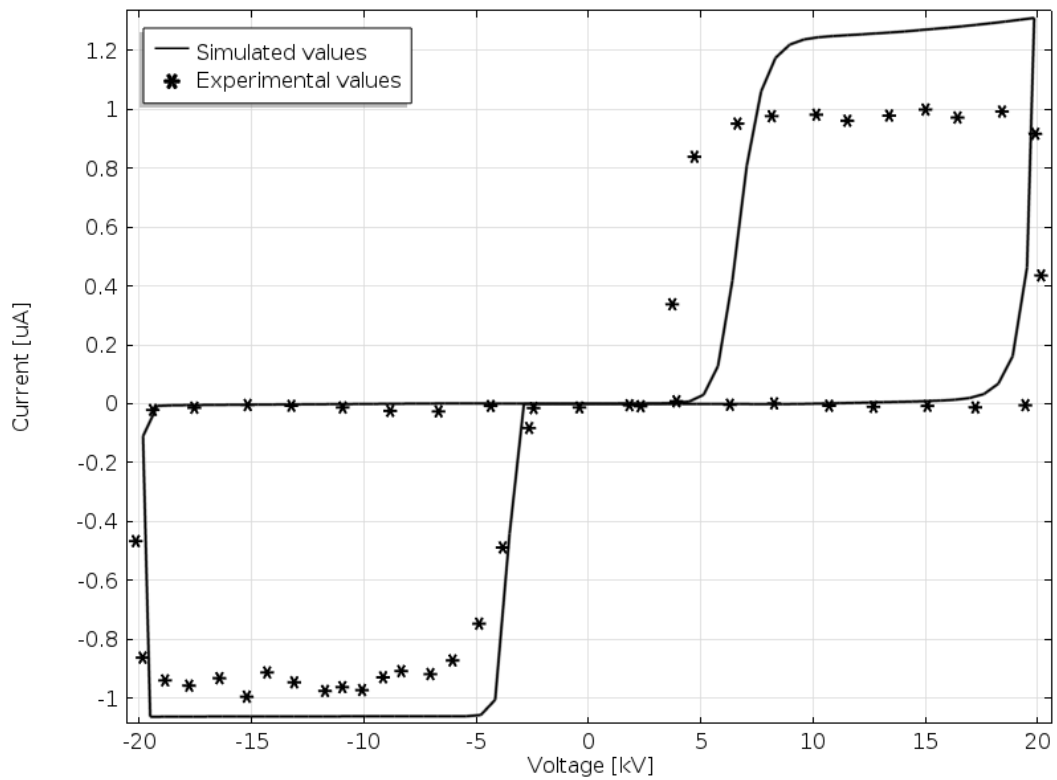


Figure 48. Best fit current-voltage characteristics achieved for the 0.1 Hz case with a PVC-barrier introduced into the discharge gap. Notice the discrepancy in peak current.